Exploring Energy Transfer and Evolution of Supernova Remnants through Year-Scale X-ray Variability

Masamune MATSUDA

Exploring Energy Transfer and Evolution of Supernova Remnants through Year-Scale X-ray Variability

Masamune MATSUDA

Kyoto University

A thesis submitted for the degree of

Doctor of Science

Feb. 6th, 2024

Acknowledgements

First and foremost, I extend my heartfelt gratitude to my supervisors, Prof. Takeshi Go Tsuru and Assoc. Prof. Hiroyuki Uchida, for their invaluable guidance and encouragement during my five years at Kyoto University. I am also grateful to Assoc. Prof. Takaaki Tanaka for his excellent advice, both during his work at Kyoto University and after his promotion to Konan University. Working with them over the past years has been an honor and a source of pride.

I would like to express my appreciation to my collaborators, Yuki Amano, Hiroya Yamaguchi, Shiu-Hang Lee, and Adrien Picquenot, for their insightful comments and contributions. Special thanks are due to Brian J. Williams for his kindness and valuable support during my stay at GSFC/NASA, as well as for providing invaluable advice related to my research. My time there was made meaningful, thanks to him.

I extend my thanks to all members of the Cosmic-Ray group at Kyoto University for engaging in pleasant communications and fruitful discussions.

最後に、私をこれまで育ててくれた両親及び家族に、この場をお借りして感謝を伝えます。本当にありがとうございました。

2023年12月　　松田　真宗

Abstract

Shock waves in the Universe are generally formed as "collisionless" shocks, whose physical scale is much shorter than the mean free path of Coulomb collisions. The collisionless shock can be observed in ubiquitous astrophysical environments, involving a number of unsettled problems, such as cosmic-ray acceleration, electron heating, and the evolution of magnetic field turbulence. Year-scale X-ray variabilities of supernova remnants (SNRs) can provide information on real-time changes in shock and post-shock physics, although there are few examples of it. This thesis focuses on time variability in SNRs to explore the shock acceleration, heating, and expansion of SNRs with the Chandra.

Tycho's SNR is a nearby and young SNR, which we can observe fine structure from the high-resolution imaging with Chandra. Therefore, we can expect the detection of time variabilities even on a small physical scale. A previous study indeed discovered X-ray flux changes of synchrotron radiation from part of the western "stripe" structure in Tycho's SNR, where protons might be accelerated to PeV energy. Expanding the region and energy band for searching time variabilities from Chandra images obtained in 2000, 2003, 2007, 2009, and 2015, we discovered two significant flux changes: fluctuation in nonthermal radiation along each stripe in the entire structure and gradual brightening in thermal radiation in the northeast rim. Spectral analysis of the former reveals the year-scale fluctuations of photon indices and brightness in each region, along with a tight anti-correlation between them. The fluctuation timescale suggests the magnetic field amplification up to ~ 500 μG. Additionally, the stripes have harder spectra than remnant rims, indicating a more effective acceleration than the rim. In the latter case of thermal radiation, we discovered an increase in electron temperature from ~ 0.3 keV to ~ 0.7 keV over 15 years from spectral analysis. The temperature increase can be attributed to ambient dense gas heated by shock and subsequent thermal energy acquisitions from heavier ions via Coulomb collisions. Comparison with the calculation of electron temperature evolution can confine the electron-to-proton temperature ratio immediately behind the shock ($\beta_0 \equiv T_e/T_p$), whose value is consistent with that measured with previous Hα observations. We propose a new method to measure β_0 independently of Hα measurements.

To investigate the ambient dense gas of Tycho's SNR implied above, we measured the velocity of remnant expansion with newly observed data from 2022 to 2023 with Chandra, as well as the data from 2003 to 2015 analyzed by a previous study. Our result exhibits further deceleration in the western shell from 2015 to 2021 beyond the velocity from 2003 to 2015 measured by the previous study, supporting the existence of the wall formed by the wind from the progenitor system. Our spectral analysis of synchrotron X-rays from the shock front revealed softening trends in some regions. We would understand the ambient environment and the effect of shock–wall interaction on the radiation from the shock, combining the theoretical model of shock dynamics and particle acceleration in future work.

We propose the application of measuring the thermal X-ray variabilities to other regions of Tycho's SNR or other SNRs, aiming to investigate the dependence of β_0 on parameters like shock velocity and magnetic field. Kepler's SNR, which is similar in age, distance, and explosion type to Tycho's SNR, shows an indication of thermal X-ray brightening along the distribution of circumstellar medium. This would enable us to investigate the dependence on factors such as ambient magnetic field. We also introduce the possible existence of thermal X-rays from heated ambient gas extending across a northeastern wide area of Tycho's SNR. The high-resolution spectroscopy with the recently launched observatory, XRISM, allows us to resolve it and reveal the time variabilities of ion temperatures behind the shock.

Contents

List of Figures

List of Tables

1

Shock Waves in Astrophysical Environment

Contents

1.1 Overview of Collisionless Shock

Shock waves in the Universe are observed in ubiquitous astrophysical environments, including the Earth's bow shock (e.g., Schwartz et al., 1988), supernova remnants (SNRs) (e.g., Laming et al., 1996; Ghavamian et al., 2001), gamma-ray bursts (e.g., Mészáros & Rees, 1997), and merging galaxy clusters (e.g., Markevitch et al., 2005; Russell et al., 2012). In contrast to terrestrial shock waves, astrophysical shock waves have much shorter thickness than the collisional mean free path, resulting in infrequent Coulomb collisions. These types of shock waves are generally referred to as "collisionless shock." Let us consider, for example, the bow shock front of Earth's magnetosphere in the solar wind. Its thickness is $\sim$ 100 km while the mean free path in this region extends to approximately the distance between the Sun and Earth ($\sim 1.5 \times 10^9$ km). The physics of the collisionless shock closely involves a number of intriguing topics, such as cosmic-ray acceleration and electron heating. This chapter presents the basic background of collisionless shocks in SNRs.

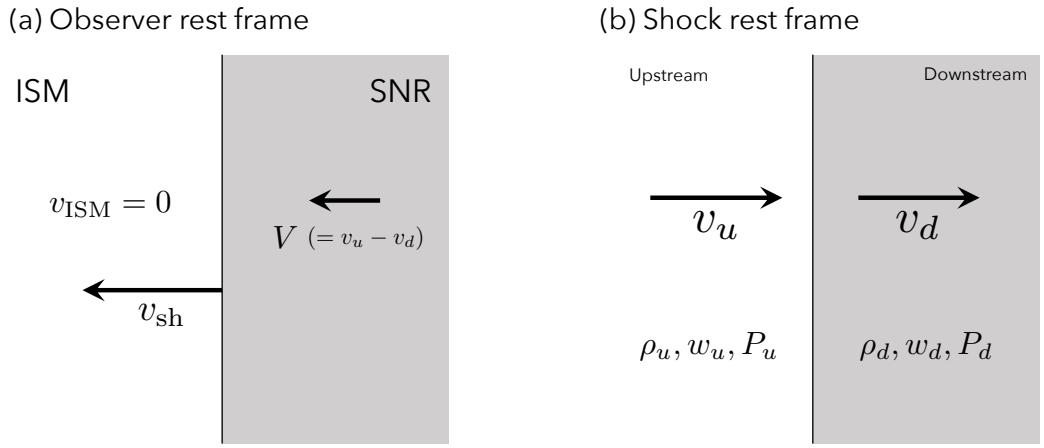

Figure 1.1: Schematic of the SNR shock waves and the particle behavior around the shock in observer rest frame (a) and shock rest frame (b).

1.2 Shock Heating in Astrophysical Plasma

1.2.1 Rankine-Hugoniot Jump Condition

The shock waves compress the downstream gas. It follows that the shock waves heat the particles downstream. Let us consider a scenario where a shock wave in SNR propagates through the interstellar medium (ISM) at a velocity $v_{\rm sh}$, while the particles behind the shock front possess a velocity of V (Figure 1.1). In the rest frame of the shock front, the particles are injected with v_u ($= v_{\rm sh}$) and exit with v_d ($= v_{\rm sh} - V$). The jump conditions can be expressed as follows, considering the conservation laws of mass, momentum, and energy:

$$\rho_u v_u = \rho_d v_d, \tag{1.1}$$

$$P_u + \rho_u v_u^2 = P_d + \rho_d v_d^2, \tag{1.2}$$

$$\frac{1}{2}v_u^2 + w_u = \frac{1}{2}v_d^2 + w_d, \tag{1.3}$$

where ρ, P, and w represent mass densities, pressures, and enthalpy densities for the upstream (subscript u) and downstream (subscript d) regions, respectively. These formulas are called "Rankine-Hugoniot jump conditions" (Rankine, 1870; Hugoniot, 1887, 1889).

When we assume the behavior of an ideal gas, the enthalpy can be written as follows:

$$w = C_{\rm P}T = \frac{\gamma P}{(\gamma - 1)\rho}. \tag{1.4}$$

Here, γ ($\equiv C_{\rm P}/C_{\rm V}$) represents the adiabatic index ($\equiv C_{\rm P}/C_{\rm V}$), where $C_{\rm P}$ and $C_{\rm V}$ denote the heat capacities at constant pressure and volume, respectively. The ratios of densities, pressures, and temperatures between upstream and downstream can be derived from

Equations (1.1), (1.2), (1.3), and (1.4):

$$\frac{\rho_u}{\rho_d} = \frac{v_d}{v_u} = \frac{(\gamma+1)P_u + (\gamma-1)P_d}{(\gamma-1)P_u + (\gamma+1)P_d}, \tag{1.5}$$

$$\frac{P_u}{P_d} = \frac{(\gamma+1)\rho_u - (\gamma-1)\rho_d}{(\gamma+1)\rho_d - (\gamma-1)\rho_u}, \tag{1.6}$$

$$\frac{T_u}{T_d} = \frac{P_d\rho_u}{P_u\rho_d} = \frac{P_d[(\gamma+1)P_u + (\gamma-1)P_d]}{P_u[(\gamma-1)P_u + (\gamma+1)P_d]}. \tag{1.7}$$

The velocities of the gas can be expressed as follows:

$$v_u^2 = \frac{[(\gamma-1)P_u + (\gamma+1)P_d]^2}{2\rho_d[(\gamma+1)P_u + (\gamma-1)P_d]}, \tag{1.8}$$

$$v_d^2 = \frac{(\gamma+1)P_u + (\gamma-1)P_d}{2\rho_d}. \tag{1.9}$$

In the case of a strong shock, in which the upstream pressure is negligibly small compared to its downstream pressure ($P_d/P_u \gg 1$), Equations (1.5), (1.7), (1.8), and (1.9) can be simplified to:

$$\frac{\rho_u}{\rho_d} = \frac{v_d}{v_u} = \frac{\gamma-1}{\gamma+1}, \tag{1.10}$$

$$\frac{T_u}{T_d} = \frac{P_d\rho_u}{P_u\rho_d} = \frac{(\gamma-1)P_d}{(\gamma+1)P_u}, \tag{1.11}$$

$$v_u^2 = \frac{(\gamma+1)^2 P_d}{2(\gamma-1)\rho_d} = \frac{(\gamma+1)^2}{2\gamma(\gamma-1)}c_s^2, \tag{1.12}$$

$$v_d^2 = \frac{(\gamma-1)P_d}{2\rho_d} = \frac{\gamma-1}{2\gamma}c_s^2, \tag{1.13}$$

where $c_s = \sqrt{\gamma P_d/\rho_d}$ is the downstream sound velocity. Especially for monoatomic gas ($\gamma = 5/3$), the ratios of densities and velocities are

$$\frac{\rho_u}{\rho_d} = \frac{1}{4}, \tag{1.14}$$

$$\frac{v_u}{v_d} = 4.$$

Moreover, the downstream average temperature can be expressed from Equations (1.12) using the shock velocity v_{sh} ($= v_u$):

$$k_B T_d = \mu m_H \frac{P_d}{\rho_d} = \frac{2(\gamma-1)}{(\gamma+1)^2}\mu m_H v_{sh}^2 \tag{1.15}$$

$$= \frac{3}{16}\mu m_H v_{sh}^2. \tag{1.16}$$

where k_B, μ, and m_H represent the Boltzmann constant, the averaged molecular mass, and the hydrogen mass, respectively. Using the Equation (1.16), we can estimate downstream temperature from the shock velocity. This can be interpreted as the conservation from the kinetic energy of the shock to the internal (thermal) energy of the plasma.

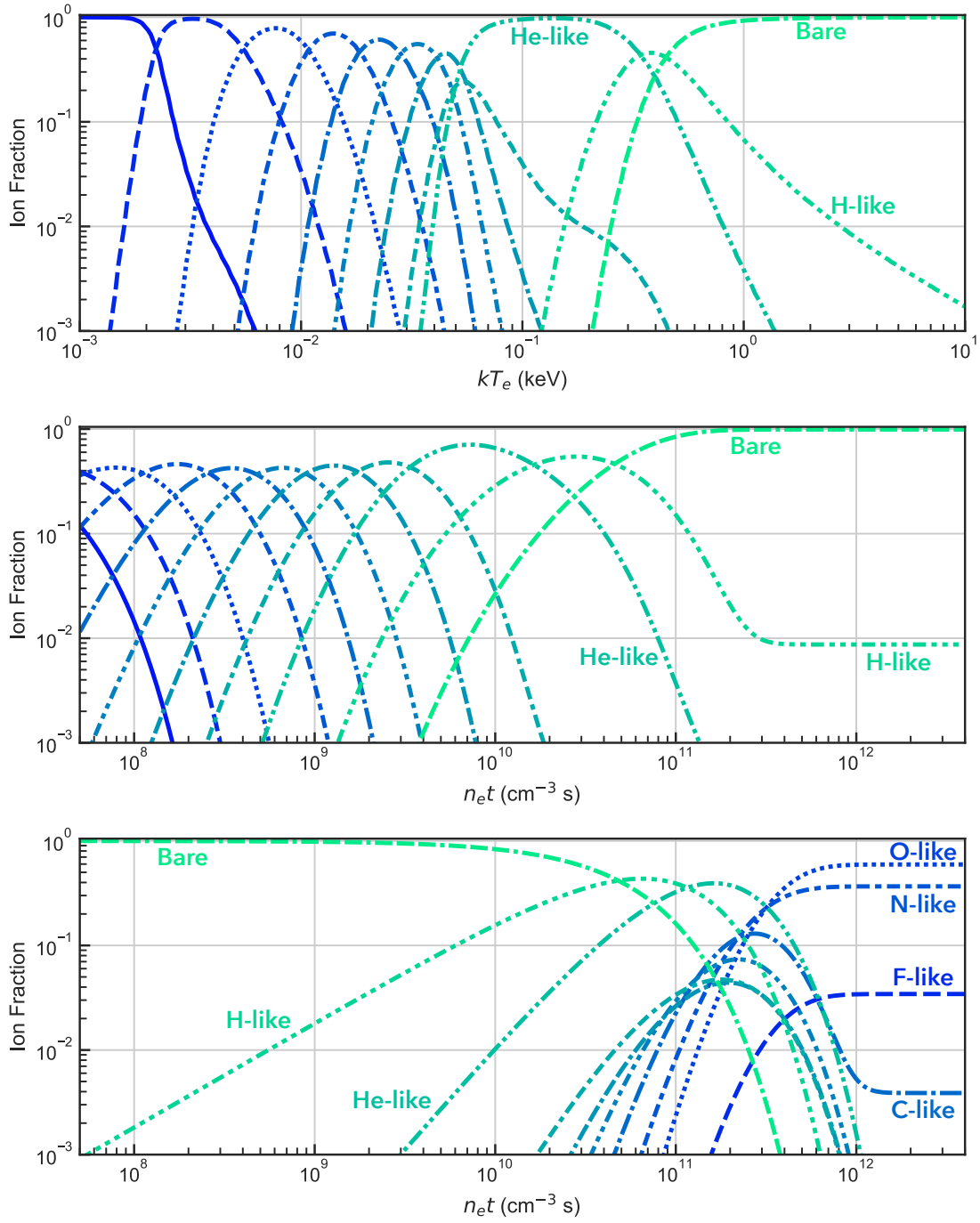

Figure 1.2: (Top panel): Ion fraction of Ne in CIE plasma as a function of the electron temperature (kT_e). (Middle panel): Ion fraction of Ne in ionization plasma of $kT_e = 3$ keV as a function of $n_e t$. (Bottom panel): Ion fraction of Ne in recombining plasma of $kT_e = 0.01$ keV as a function of $n_e t$ when the initial state is the fully ionized state. The calculation of each panel is conducted using PyAtomDB[1]

1.2.2 Ionization Equilibrium

After the electron temperature of the plasma changes rapidly for some reason like the shock heating, the ionization state is driven out of equilibrium. The time evolution of the ion density in the collisional ionization plasma can be written as:

$$\frac{1}{n_e}\frac{d\vec{N}_Z}{dt} = \mathbb{A}(Z, T_e)\vec{N}_Z, \tag{1.17}$$

where

$$\vec{N}_Z = (n_{Z,0}, n_{Z,1}, \cdots, n_{Z,Z}) \tag{1.18}$$

$$\mathbb{A} = \begin{pmatrix} -S_{Z,0} & \alpha_{Z,1} & 0 & 0 & \cdots & 0 \\ S_{Z,0} & -(S_{Z,1}+\alpha_{Z,1}) & \alpha_{Z,2} & 0 & \cdots & 0 \\ 0 & S_{Z,1} & -(S_{Z,2}+\alpha_{Z,2}) & \ddots & \cdots & \vdots \\ \vdots & \vdots & \ddots & \ddots & \ddots & \vdots \\ 0 & \cdots & \cdots & S_{Z,Z-2} & -(S_{Z,Z-1}+\alpha_{Z,Z-1}) & \alpha_{Z,Z} \\ 0 & \cdots & \cdots & 0 & S_{Z,Z-1} & -(S_{Z,Z}+\alpha_{Z,Z}) \end{pmatrix}. \tag{1.19}$$

Here, $n_{Z,z}$, $S_{Z,z}$ and $\alpha_{Z,z}$ are the density, the ionization rate coefficient, and the recombination rate coefficient of the ions with the atomic number Z and the charge number z. These coefficients solely depend on the electron temperature T_e. Thus, $\vec{N}_Z$ depends on $\int n_e dt = n_e t$ under the assumption of the constant electron temperature. The parameter of $n_e t$ is called "ionization timescale," which is used to describe the plasma equilibrium state in general analysis codes. The ionizing state can be divided into the following three states:

1. *Collisional Ionization Equilibrium (CIE)*:
   The equilibrium state between collisional recombining and ionizing in the plasma. Typically, the plasma reaches CIE when $n_e t = 10^{13}$ cm^{-3} s. Figure 1.2 (top) shows the ion population of Ne under the CIE state as a function of $k_B T_e$.

2. *Non-Equilibrium Ionization (NEI)*:
   The state in which either collisional recombining or ionizing is dominant. The plasma state of NEI can be divided into ionizing plasma (IP; Figure 1.2 middle) and recombining plasma (RP; Figure 1.2 bottom).

1.2.3 Thermal Equilibrium in Plasma

The post-shock plasma reaches thermal equilibrium initially within each ion and subsequently between different ions. As can be seen from Equation (1.16), the temperature (T_i) of ion with mass m_i can be written as:

$$k_B T_i = \frac{3}{16} m_i v_{\rm sh}^2. \tag{1.20}$$

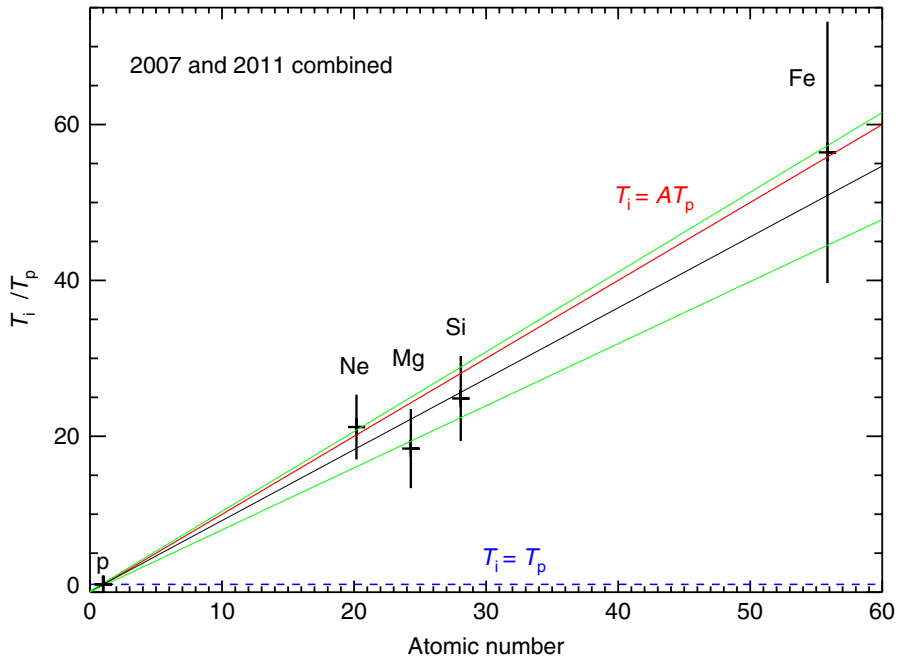

Figure 1.3: The relation between the ion/proton temperature ratio and the atomic number (Miceli et al., 2019). The red line shows the function predicted from Equation (1.20). The black line shows the best-fit function, and the green lines show the confidence levels of 90%.

Equation (1.20) shows that the ion temperature is proportional to the ion mass. Actually, Miceli et al. (2019), who measured the temperature of several ion species of shock-heated plasma in SN 1987A, revealed a linear increase of the ion temperature depending on the ion mass (Figure 1.3).

Let us consider the case of the energy equipartition between two different ion species (test particles and field particles). We assume that the test and field particles already reach thermal equilibrium states of T and T_f, respectively, and the particles follow the Maxwell-Boltzmann distribution depicted as follows (Spitzer, 1962):

$$P(v) = \left(\frac{m_e}{2\pi k_{\rm B} T}\right)^{3/2} \exp\left(-\frac{m_e v^2}{2k_{\rm B} T}\right), \tag{1.21}$$

where $k_{\rm B}$ is the Boltzmann constant. The time evolution of T can be written as:

$$\frac{dT}{dt} = \frac{T_f - T}{t_{\rm eq}}. \tag{1.22}$$

Here, $t_{\rm eq}$ is called relaxation time, which is given by

$$t_{\rm eq} = \frac{3mm_f k_{\rm B}^{3/2}}{8(2\pi)^{1/2} n_f Z^2 Z_f^2 e^4 \ln\Lambda} \left(\frac{T}{m} + \frac{T_f}{m_f}\right)^{3/2} \tag{1.23}$$

$$= 5.87 \frac{AA_f}{n_f Z^2 Z_f^2 \ln\Lambda} \left(\frac{T}{A} + \frac{T_f}{A_f}\right)^{3/2} \ {\rm s}, \tag{1.24}$$

[1] https://atomdb.readthedocs.io/en/master/ (Foster et al., 2017).

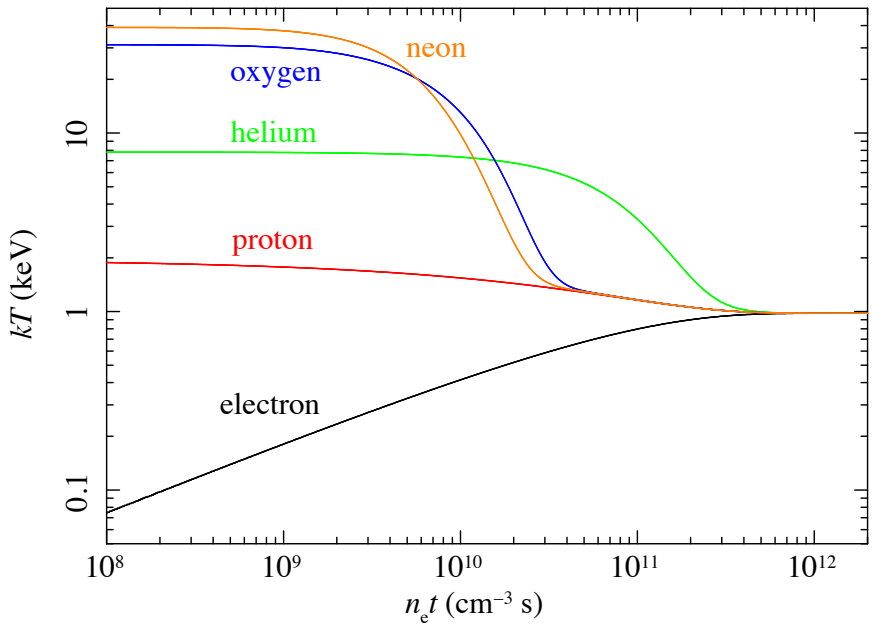

Figure 1.4: An example calculation of the temperature evolution at the shock waves, assuming a shock velocity of $v_{\rm sh} = 1000$ km s^{-1} (Katsuda, 2023). The heating of each ion at the shock front is assumed to follow Equation (1.20), and then the temperature changes in accordance with Equation (1.22).

where n, Z, and A are densities, atomic number, and mass number of ions, respectively. The Coulomb logarithm $\ln \Lambda$ ($\sim$ 25–30) is defined as

$$\ln \Lambda \equiv \ln \left(\frac{4\pi}{3} n_e \lambda_{\rm D}^3 \right), \tag{1.25}$$

where the Debye length $\lambda_{\rm D}$ is available in the NRL Plasma Formulary, pages 34–35[2].

Figure 1.4 shows an example calculation of the temperature evolution at the shock. The timescale of the thermal equilibration depends on the density and the square of the particle charge (Equation 1.23). Additionally, the temperature at the shock depends on the ion mass. Thus, thermal equilibrium is reached first between ion–ion and then between electron–ion. The equilibration is broadly divided into three phases:

1. *Full non-equilibration* ($n_e t \lesssim 5 \times 10^{10}$ cm^{-3} s):
   The temperatures of all species are different.

2. *Partial non-equilibration* ($5 \times 10^{10} \lesssim n_e t \lesssim 10^{12}$ cm^{-3} s):
   Equilibration within all ions is reached, but electron–ion equilibration has not yet.

3. *Full equilibration* ($n_e t \gtrsim 10^{12}$ cm^{-3} s):
   All particles are equilibrated.

[2] https://library.psfc.mit.edu/catalog/online_pubs/NRL_FORMULARY_13.pdf

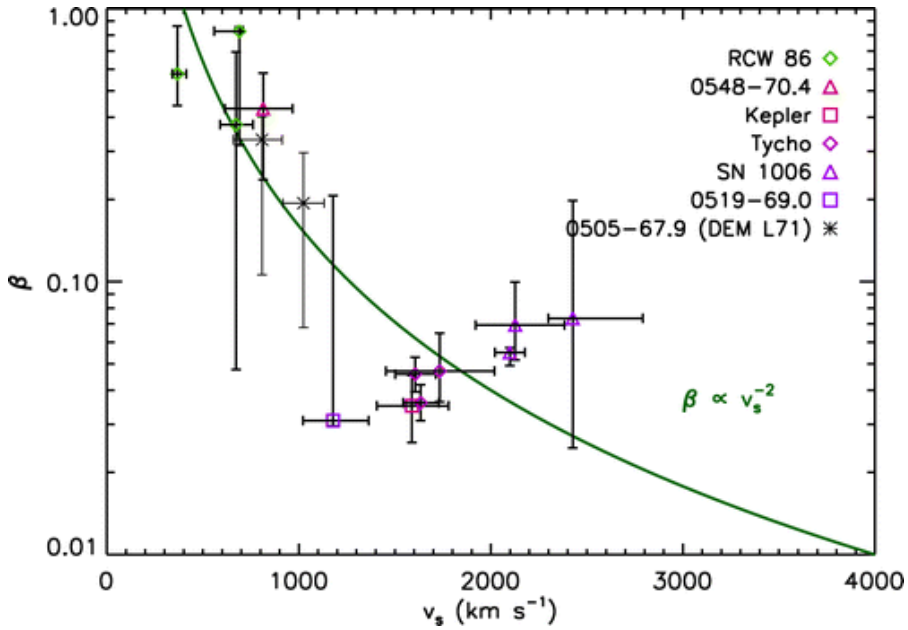

Figure 1.5: Temperature ratio β as a function of the shock velocity v_s for Balmer-dominated shock in several SNRs (van Adelsberg et al., 2008). Data points are fitted by calculations with the methodology by van Adelsberg et al. (2008). Each symbol shape of the data point shows the corresponding SNRs. The solid curve denotes the dependence $\beta(v_s) \propto v_s^{-2}$.

1.2.4 Collisionless Electron Heating

Under the typical environment around SNRs ($k_B T_e = 1$ keV, $n_e = 1$ cm^{-3}), the relaxation time between electron and proton can be calculated to be $\sim 100,000$ years from Equation (1.23). Since the typical age of an SNR is 1,000 years, the temperature ratio immediately behind the shock ($\beta \equiv T_e/T_p$) is expected to be:

$$\beta \equiv \frac{T_e}{T_p} = \frac{m_e}{m_p} \simeq \frac{1}{1836}. \tag{1.26}$$

On the other hand, several studies observed T_e/T_p to be ~ 1 at the shocks in young SNRs with age of hundreds of years (e.g., Laming et al., 1996; Ghavamian et al., 2001; Rakowski et al., 2003). This deviation between the expectation and the observation is generally attributed to processes other than Coulomb collisions, called "collisionless electron heating." The mechanism of the process is often thought to be related to the energy dissipation at the shock front and precursor due to strong plasma turbulence (e.g., Shimada & Hoshino, 2005; Bohdan, 2023). However, the physics of collisionless electron heating is still unsettled because there are several complex instabilities in forming the collisionless shock, which should be directly associated with the process (e.g., Cargill & Papadopoulos, 1988; Ghavamian et al., 2007; Rakowski et al., 2008; Laming et al., 2014).

The electron-to-ion temperature ratio immediately after shock ($\beta \equiv T_e/T_{\rm ion}$) is commonly used to describe the equilibration between electrons and ions at shock transition, consequently indicating the efficiency of collisionless electron heating. The ratio $T_e/T_{\rm ion}$ is determined with various methods, including "in situ" observations of solar wind bow

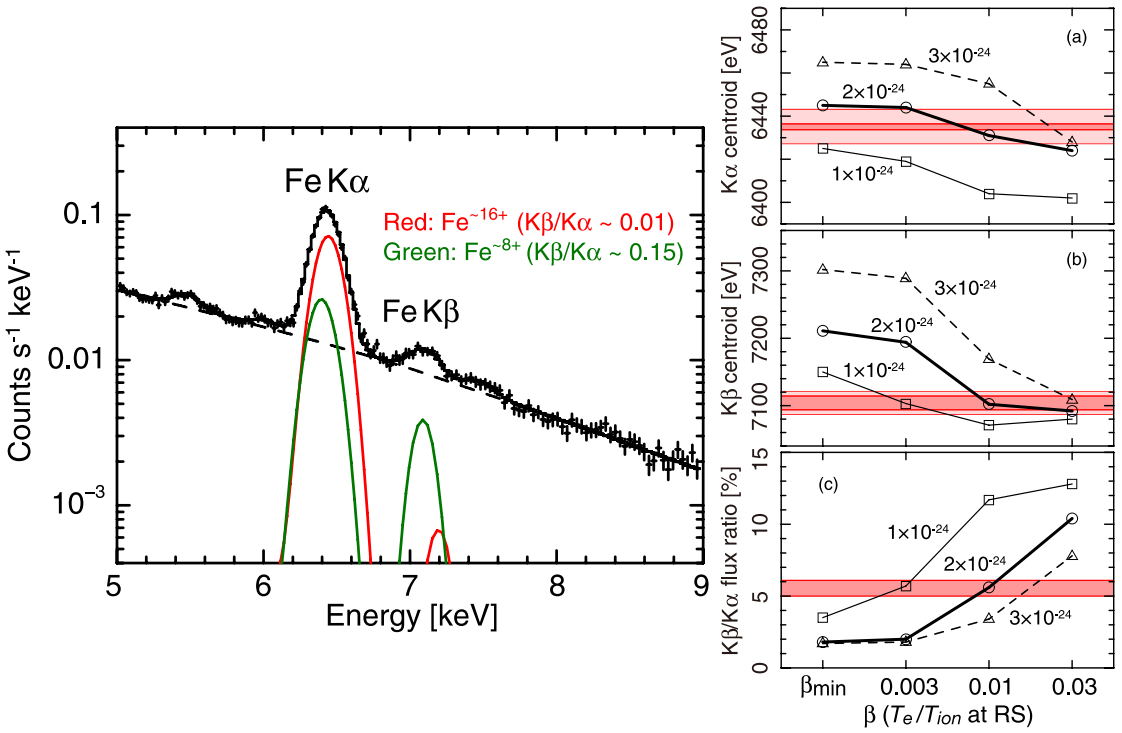

Figure 1.6: (Left): The detected Fe Kβ emission in the reverse shock in Tycho's SNR (Yamaguchi et al., 2014). (Right): The dependence of the centroid energy of Fe Kα and Kβ lines and their flux ratio on $T_e/T_{\rm ion}$. The plots in the right panel correspond to the different ambient densities. The red regions represent the observed value with statistical (dark) and systematic (light) uncertainties.

shocks (Schwartz et al., 1988; Masters et al., 2011). Optical observations can measure T_e/T_p using Hα line diagnostics in Balmer-dominated shocks (e.g., Ghavamian et al., 2001; Medina et al., 2014). The Hα lines at the shock wave consist of two components: a narrow component, which emits from hydrogen atoms collisionally excited at the shock transition layer, and a broad component, which emits from hydrogen atoms produced by charge transfer collisions with downstream protons. The ratio of the broad-to-narrow components can estimate T_e/T_p since it depends on the charge exchange, ionization, and excitation rates, which are sensitive to the electron and proton temperatures, and the width of the broad component directly reflects the proton temperature (Laming, 2000). Hα lines come from a confined region downstream of the shock within $\sim 10^{14}$ cm (van Adelsberg et al., 2008) because hydrogen atoms in the deeper region are ionized and unable to emit Hα lines. Thus, this method is often used in SNRs because it allows the selective measurement of T_e/T_p at a stage where Coulomb collisions have not yet significantly influenced the plasma. Figure 1.5 shows the T_e/T_p ($\equiv \beta$) in several SNRs estimated from the broad-to-narrow component ratio of Hα lines.

Another method to measure $T_e/T_{\rm ion}$ is proposed by Yamaguchi et al. (2014). They estimated $T_e/T_{\rm Fe}$ from Fe K diagnostics in Tycho's SNR using the X-ray data obtained with the *Suzaku* satellite. Their spectral analysis detected Kα and Kβ lines from highly-ionized and low-ionized iron, as seen in Figure 1.6 (left). From the comparison with the simulation of the Fe ionization state, the observed centroid energy of the Kβ line requires

the $T_e/T_{\rm Fe} \simeq 0.01$ at the reverse shock (Figure 1.6 right). They presented a method that allows us to diagnose the plasma state and measure β with low-ionized iron, which is present in a limited region of immediate postshock ejecta.

1.3 Particle Acceleration in SNR

1.3.1 Cosmic Ray

ISM particles are accelerated at collisionless shocks and gain relativistic energy after injections into the shocks. These particles are referred to as cosmic rays (CRs), which reach Earth from cosmic space. Since the discovery of CR by Hess (1912) using balloons, they have been observed through various experiments, including balloon missions (e.g., Fleisher et al., 1975), satellites (e.g., The Fermi-LAT Collaboration et al., 2017), and ground-based detectors (e.g., Telescope Array Collaboration et al., 2023). Figure 1.7 illustrates the CR spectrum observed by different experiments. The spectrum exhibits distinct breaks mainly at two energy points: $\sim 3 \times 10^{15}$ eV (referred to as the "knee") and $\sim 3 \times 10^{18}$ eV (referred to as the "ankle"). CRs with energy below 3×10^{15} eV are believed to be produced in our Galaxy (the Galactic CR), while those with higher energy are thought to come from extra-galactic sources. Nevertheless, the origin of CR and its underlying physics remain open questions.

SNRs have been thought to be the main candidate of the Galactic CR accelerator for decades (Baade & Zwicky, 1934). One reason is that it has a large enough energy budget to accelerate CRs. The required energy to keep the CRs is estimated to be $L_{\rm CR} \simeq 10^{41}$ erg s^{-1}. Because the energy of supernovae (SNe) is $E_{\rm SN} \simeq 10^{51}$ erg, the explosion energy provided to the Galaxy as kinetic energy is $L_{\rm SN} \simeq f_{\rm SN} E_{\rm SN} \simeq 10^{42}$ erg s^{-1} under an assumption of the SNe rate to be $f_{\rm SN} \simeq 0.03$ yr^{-1}. If 10% of the total kinetic energy is used for the acceleration of CRs, the CR energy density can be explained feasibly. Another reason is the acceleration mechanism of the first-order Fermi acceleration or Diffusive Shock Acceleration (DSA) (e.g., Axford et al., 1977; Blandford & Eichler, 1987; Drury, 1983; Bell, 1978a,b). The acceleration mechanism predicts the energy spectrum of CRs to be distributed in power law, which is consistent with the observations.

1.3.2 Diffusive Shock Acceleration

Let us consider the behavior of individual particles around the shock transition. Figure 1.8 presents the schematic view of the DSA. Here, we make three assumptions: (i) steady state, (ii) plane parallel non-relativistic shock, and (iii) test particle approximation. Under the test particle approximation, we ignore the effect on the macroscopic plasma by non-thermal particles.

Around the collisionless shock, the plasma has magnetic field turbulence, leading to charged particle scattering via magnetohydrodynamical (MHD) waves such as Alfén waves. The scattering alters the direction of the particle motion, resulting in particle

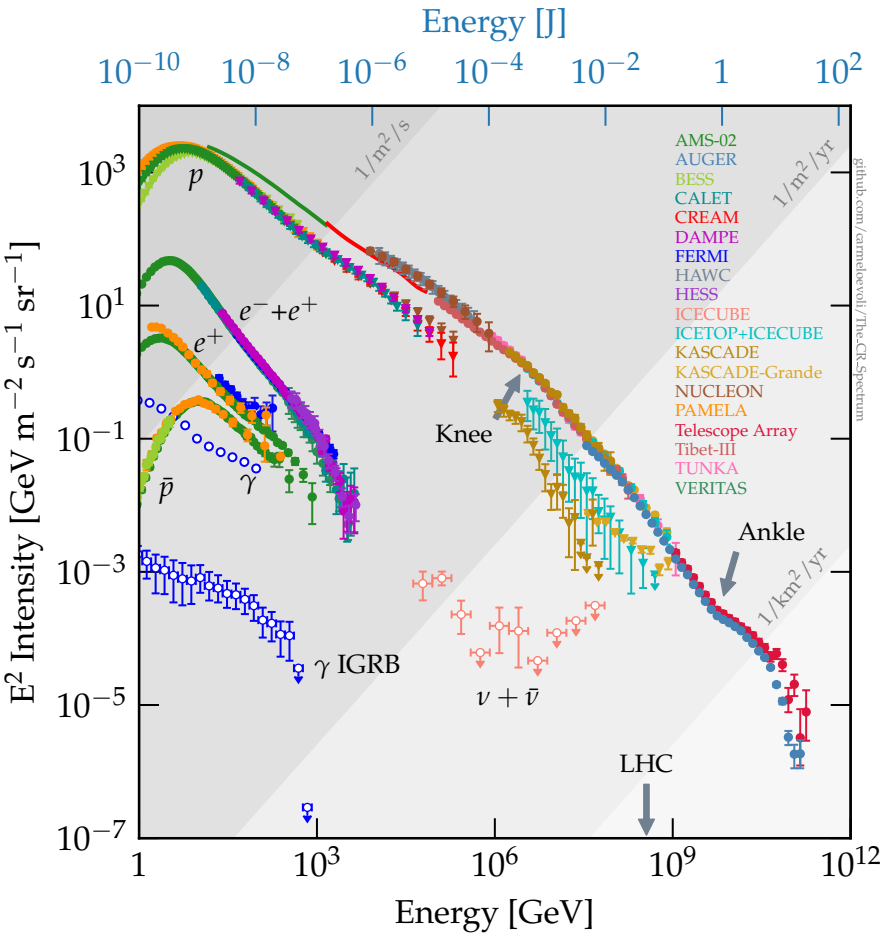

Figure 1.7: Cosmic ray spectrum (Evoli, 2020).

acceleration as the particle transverses the shock multiple times. When an upstream particle with the energy E injects downstream, the downstream energy in the rest frame of the upstream observer (E') can be expressed as:

$$E' = \gamma(E + V p_x), \tag{1.27}$$

where $V = v_d - v_u$, $p_x = (E/c)\cos\theta$, and $\gamma \equiv 1/\sqrt{1-(V/c)^2} \simeq 1$ are the downstream velocity in the upstream frame, the momentum perpendicular to the shock, and the Lorentz factor, respectively. The angle θ is between the momentum vector and the normal shock vector. From Equation (1.27), the particle, after crossing the shock, gains energy of:

$$\Delta E = E' - E = \frac{V}{c} E \cos\theta. \tag{1.28}$$

The averaged gain energy is derived as follows:

$$\left\langle \frac{\Delta E}{E} \right\rangle = \int_0^{\pi/2} \frac{\Delta E}{E} 2 \sin\theta \cos\theta \, d\theta = \frac{2V}{3c}. \tag{1.29}$$

Also, the particle downstream undergoes multiple scatterings and eventually crosses the shock. As the upstream gas appears to approach with a velocity V in the downstream

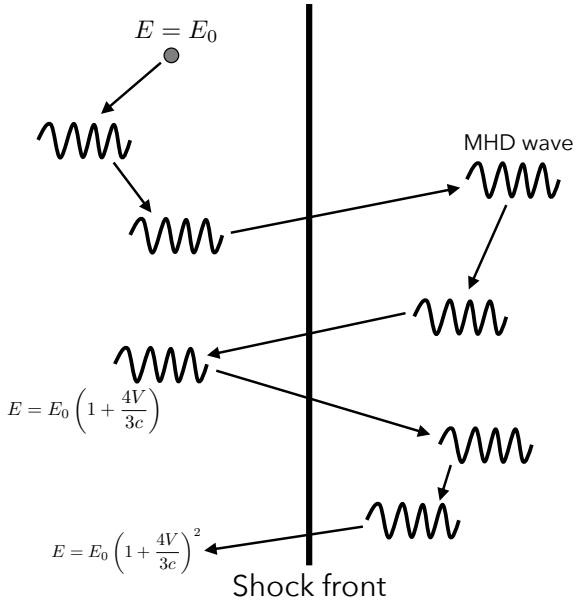

Figure 1.8: Schematic of diffusive shock acceleration.

frame, the particle gains the energy of $2V/3c$. Consequently, the average energy gain over a single round-trip through the shock is calculated to be $(\Delta E/E) = 4V/3c \ll 1$. Therefore, when the particles undergo n round-trips, their energy is given by:

$$E_n = E_0\left(1+\frac{4V}{3c}\right)^n \simeq E_0 \exp\left(\frac{4V}{3c}n\right), \tag{1.30}$$

which indicates that the particle energy increases exponentially. Here, E_0 is the initial particle energy.

The particle escapes from the shock with the probability of $4v_d/c$ per round-trip. As a result, the number of accelerated particles decreases as the number of round trips increases. The probability of the escape at the n-th time step (P_n) is expressed as follows:

$$P_n = \left(1-\frac{4v_d}{c}\right)^n \times \frac{4v_d}{c}. \tag{1.31}$$

From Equation (1.30) and (1.31), the energy spectrum of the accelerated particles follows a power-law distribution:

$$\frac{dN}{dE} \propto E^{-(3v_d/V)-1} = E^{-(r+2)/(r-1)} \equiv E^{-s}, \tag{1.32}$$

where $r \equiv \rho_d/\rho_u = (\gamma+1)/(\gamma-1)$ is the shock compression. Using $r = 4$ in Equation (1.14), the spectral index is $s = 2$, in agreement with the observed CR spectrum.

In order to inject DSA, the particles have to reach high energy enough to cross the shocks. However, there are large gaps between thermal and injection energy, especially for electrons. This crucial problem is referred to as "injection problem", which is still open despite various theories (e.g., Bohdan, 2023).

1.3.3 Acceleration Timescale and Maximum Energy

The acceleration timescale ($t_{\rm acc}$) can be defined as the time that it takes for the accelerated particle to double in energy:

$$t_{\rm acc} = t_{\rm cyc}\left\langle \frac{E}{\Delta E} \right\rangle_{\rm cyc}, \tag{1.33}$$

where $t_{\rm cyc}$ is the time of a round trip, and $\langle E/\Delta E\rangle_{\rm cyc} = 3c/4V$ is the reciprocal of the energy gain of a round trip. Using diffusion coefficient $\mathfrak{D}$, $t_{\rm cyc}$ can be expressed by:

$$t_{\rm cyc} = \frac{4\mathfrak{D}_u}{v_u c} + \frac{4\mathfrak{D}_d}{v_d c}. \tag{1.34}$$

Therefore, $t_{\rm acc}$ can be written as:

$$t_{\rm acc} = \frac{3}{V}\left(\frac{\mathfrak{D}_u}{v_u} + \frac{\mathfrak{D}_d}{v_d}\right), \tag{1.35}$$

which means that it is necessary to get the diffusion coefficient $\mathfrak{D}$ in order to calculate $t_{\rm acc}$. The coefficient $\mathfrak{D}$ is expressed by:

$$\mathfrak{D} = \frac{\lambda_{\rm mfp}}{3}c = \frac{\eta r_{\rm g}}{3}c, \tag{1.36}$$

where $\lambda_{\rm mfp}$ is the mean free path of the scattering, which can be written as $\lambda_{\rm mfp} = \eta r_{\rm g}$ in the DSA situation using the gyro radius $r_{\rm g}$. $\eta = (B/\delta B)^2$ is the parameter called "gyro factor", which depicts the magnitude of magnetic field turbulence. Generally, $\eta \geq 1$, so the mean free path is not smaller than the gyro radius. The state of $\eta = 1$ is the so-called "Bohm limit," which corresponds to the state with the highest magnetic field turbulence. Assuming $\mathfrak{D}_u = \mathfrak{D}_d$ for the sake of simplicity and using $v_u = 4v_d = v_{\rm sh}$, the timescale $t_{\rm acc}$ can be rewritten as followings using Equation (1.35) and (1.36):

$$t_{\rm acc} = \frac{20}{3}\frac{c r_{\rm g}}{v_{\rm sh}^2}\eta. \tag{1.37}$$

Under the environment of the magnetic field B, the gyro radius of the particle with the charge of Ze and the energy of E can be expressed as:

$$r_g = \frac{E_e}{ZeB}. \tag{1.38}$$

Thus, when the maximum energy of the particles accelerated by DSA is written as the following using $t_{\rm acc}$:

$$E_{\rm max} = \frac{3}{20}\frac{v_{\rm sh}^2 ZeBt_{\rm acc}}{\eta c}. \tag{1.39}$$

The acceleration time $t_{\rm acc}$ is limited mainly by three scenarios: the age of the SNR, synchrotron cooling loss, and escaping (Reynolds, 1998). We provide detailed explanations for each scenario in the following.

Age-limited When particles continue to be accelerated with little escape or cooling since the formation of shock waves, the acceleration time is limited by the remnant age. This scenario is called *age-limited* case. The maximum energy $E_{\rm max}^{\rm age}$ can be written as the following using the remnant age $t_{\rm age}$:

$$E_{\rm max}^{\rm age} = \frac{3Ze}{20c}\eta^{-1}v_{\rm sh}^2 t_{\rm age} B \simeq 40\eta^{-1}\left(\frac{v_{\rm sh}}{3000\ {\rm km\ s^{-1}}}\right)^2\left(\frac{t_{\rm age}}{10^3\ {\rm yr}}\right)\left(\frac{B}{10\ \mu{\rm G}}\right)\ {\rm TeV}. \tag{1.40}$$

The maximum energy is generally limited by this scenario because this timescale is typically smaller than the other two timescales. Thus, to produce particles accelerated to the "knee" energy, it is necessary to increase the magnetic field to the order of mG. However, the mechanism of the magnetic field amplification is not well established (e.g., Inoue et al., 2012; Caprioli & Spitkovsky, 2014).

Loss-limited The accelerated particles lose their energy by radiating synchrotron radiation. When the cooling by synchrotron loss is dominant, the maximum energy $E_{\rm max}^{\rm loss}$ is limited by the synchrotron cooling time. Using the definition of cooling time $t_{\rm loss} \simeq 9(mc^2)^4/(4Z^4e^4B^2E_e)$ proposed by Zirakashvili & Aharonian (2007) (see also Equation 2.26), the maximum energy can be expressed as:

$$E_{\rm max}^{\rm loss} \simeq 70\eta^{-1/2}\left(\frac{v_{\rm sh}}{3000\ {\rm km\ s^{-1}}}\right)\left(\frac{B}{10\ \mu{\rm G}}\right)^{-1/2}\ {\rm TeV}. \tag{1.41}$$

This case is applicable when the magnetic field is amplified and the time scale is smaller than the remnant age, as can be seen from $t_{\rm loss} \propto B{-}2$.

Escape-limited At the late time of the remnant lifetime, particles escape upstream from DSA without being scattered by MHD waves. The maximum energy in the escape-limited case is roughly given as:

$$E_{\rm max}^{\rm esc} \simeq 100\left(\frac{\lambda_{\rm max}}{3\times10^{-2}\ {\rm pc}}\right)\left(\frac{B}{10\ \mu{\rm G}}\right)\ {\rm TeV}, \tag{1.42}$$

where $\lambda_{\rm max}$ is the maximum wavelength of MHD waves to scatter particles.

2

Supernova and Supernova Remnant

Contents

2.1 Supernova

2.1.1 Supernova Classification

Based on our comprehension of the explosion mechanism, there are two major groups of supernovae (SNe): core-collapse SNe and thermonuclear SNe. The following sections describe the mechanisms and characteristics of each explosion type. Before describing the core-collapse and thermonuclear explosions, we will briefly overview another classification scheme based on two observational criteria: optical spectroscopy and light-curve shape (Figure 2.1). The origin of the observational classification can date back to Minkowski (1941), who observed some SNe without hydrogen absorption in their spectra (Type I), while others showed hydrogen absorption. While Type II SN is consistently a core-collapse event, Type I SN encompasses both thermonuclear and core-collapse explosions. Further subcategories of Type I SN can be defined based on the presence of silicon and helium absorption lines. Type Ia SNe, identified by the presence of silicon absorption lines, are attributed to thermonuclear explosions (Elias et al., 1985). Within the Type I group, those without silicon absorption lines are thought to

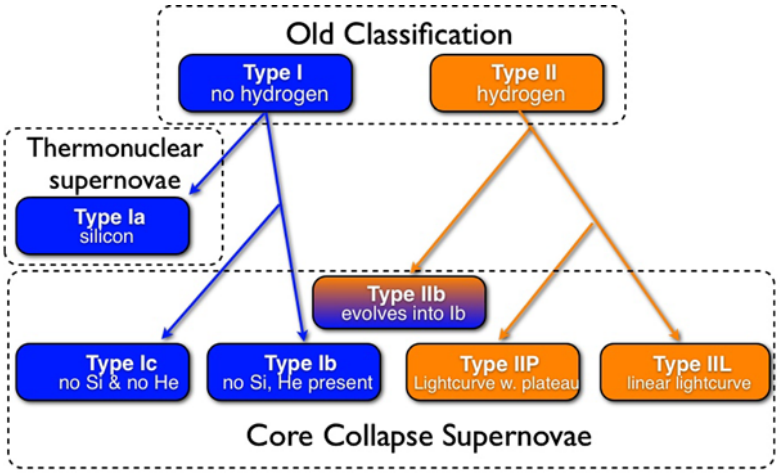

Figure 2.1: Classifications of SNe based on optical spectra and light-curve shape (Vink, 2012).

be associated with core-collapse explosions. They are classified as Type Ib SNe (without Si but with He absorption lines) and Type Ic SNe (without both Si and He absorption lines). Meanwhile, the Type II category can be divided based on light-curve shape into a Type IIP with a plateau phase and a Type IIL with a linear decline from the peak.

2.1.2 Core-Collapse SN

Core-collapse SNe occur as the result of core implosions at the end of the lives of massive stars: typically $\gtrsim 10 M_\odot$ in the main sequence phase (see a review by Woosley & Janka, 2005). Below, we provide a brief explanation of the mechanism of core-collapse SN. As a massive star evolves, the composition of its elements changes via stellar nucleosynthesis. At first, a helium-rich core is formed through hydrogen burning, followed by a carbon-rich core through helium burning. Subsequently, as nucleosynthesis progresses, cores of heavier elements are formed sequentially. Then, an iron core is formed at the center of the star as the depicted configuration of each elemental layer in Figure 2.2. When the center temperature increases to 5×10^9 K by the heating driven by contraction, the core of ^{56}Fe, the most stable nucleus, is formed, and heavier elements are no longer synthesized. It follows that the core is heated further by the contraction, resulting in the absorption of gamma rays from the very hot core:

$$^{56}\mathrm{Fe} + \gamma \rightarrow 13\,^4\mathrm{He} + 4n - 124.4\ \mathrm{MeV}. \tag{2.1}$$

Then, the helium created by this photo-disintegration process decays into neutrons and protons:

$$^4\mathrm{He} \rightarrow 2p + 2n - 28.3\ \mathrm{MeV}. \tag{2.2}$$

Subsequently, after protons capture electrons and gradually transform into neutrons, the core eventually loses its ability to be supported by processes like nucleosynthesis and electron degeneracy. As a result, the core collapses toward the center, forming a proto-neutron star or a black hole. Most of the gravitational energy ($\sim 10^{53}$ erg) is transformed

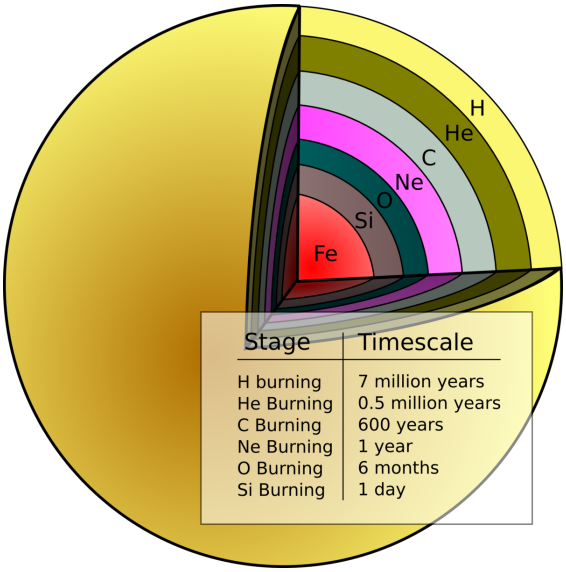

Figure 2.2: The configuration of a massive star nearing SN. The timescales are computed for a star with a mass of $25M_{\odot}$ (Deaconu, 2008).

into neutrinos, as confirmed by the observations of SN 1987A with the Kamiokande (Hirata et al., 1987), IMB detector (Haines et al., 1988), and the INR Baksan Underground Scintillation Telescope Alekseev et al. (1987). The rest of the energy ($\sim 10^{51}$ erg) is used as the explosion energy of SN. While the detailed conversion mechanism from gravitational energy to explosion energy is still under debate, neutrino heating, initially proposed by Wilson (1985), is a widely supported mechanism to drive the shock revival.

2.1.3 Thermonuclear SN

Type Ia SNe are widely believed to originate from the explosive thermonuclear burning in white dwarfs with no hydrogen envelope. It is supported by the fact that the SNe are also found in all galaxy types, including old elliptical galaxies, which have abundant low-mass stars (Wang et al., 1997). When the mass of a carbon-oxygen (CO) white dwarf approaches or exceeds the Chandrasekhar limit ($\sim 1.4M_{\odot}$) for some reason, the electron degeneracy pressure can no longer support its own mass. After the core density reaches $\sim 2 \times 10^9$ g cm^{-3}, the ignition and detonation of ^{12}C + ^{12}C fusion is triggered, following the ejection of the entire star, including its core (Arnett, 1969). The ejecta of Type Ia SN has a metal-rich characteristic; the abundances of heavy elements like intermediate-mass elements (IMEs: silicon, sulfur, argon, and calcium) and iron are higher compared to those of the solar abundance.

Although many astrophysicists accept that the thermonuclear SNe occur from binary systems, there are a variety of theories for the progenitor system that enables the white dwarf to obtain mass, leading to ongoing debates (Liu et al., 2023, for a review). Figure 2.3 shows the various theories of the progenitor system. We note that they are not all of the theories. The theories can be divided mainly into two groups: single-degenerate

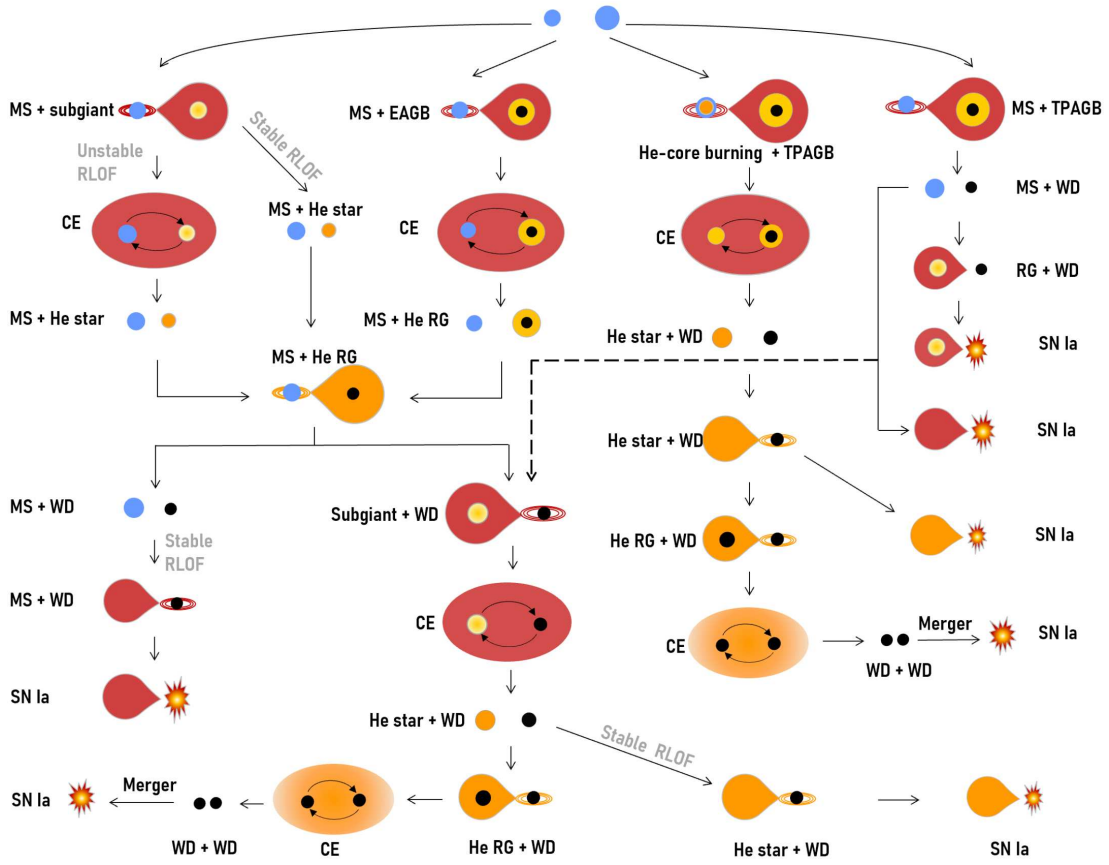

Figure 2.3: Schematic illustrating the progenitor of Ia SNe (Liu et al., 2023).

(SD) and double-degenerate (DD) scenarios. The former assumes the binary of a white dwarf and a non-degenerate companion star, such as a main sequence or red giant. The white dwarf gains mass from the companion star via accretion (Whelan & Iben, 1973). In the latter scenario, two white dwarfs merge and explode (Webbink, 1984; Iben & Tutukov, 1984). Because each scenario has its advantages and disadvantages, the progenitor system of Ia SNe is still open. One observational guide to distinguishing the two scenarios is probing the circumstellar medium (CSM) created by the wind from a progenitor white dwarf during mass accretion.

Type Ia SNe are also known as standard candles because their peak brightnesses have much less variation than the other SNe types. Owing to this, Type Ia SNe is often used as distance indicators in cosmology, leading to the findings of the accelerating expansion of the Universe (Perlmutter et al., 1998; Garnavich et al., 1998; Riess et al., 1998) and measurement of the Hubble constant H_0 (Riess et al., 2019).

2.2 Supernova Remnant

2.2.1 Evolution of SNR

Free Expansion Phase After SN, most of the explosion energy ($E_{\rm SN}$) transfers to the kinetic energy and 2–3% of $E_{\rm SN}$ to thermal energy. The exploded ejecta expands with the velocity of $\sim 10,000$ km s^{-1}, much faster than the sound velocity in ISM (~ 10 km s^{-1}). It follows that forward shock (blast wave) at the front of the ejecta. The blast wave sweeps up the surrounding ISM. Since the mass of swept-up ISM ($M_{\rm ism}$) is negligibly smaller than the mass of ejecta ($M_{\rm ej}$) in the early phase after the SN, the ejecta expands without decelerating. Therefore, this phase is called the "free expansion phase." The expansion velocity ($v_{\rm sh}$) and the radius of the supernova remnant (SNR) can be denoted as follows:

$$v_{\rm s} = \sqrt{\frac{2E_{\rm SN}}{M_{\rm ej}}} = 1.0\times10^4 \left(\frac{E_{\rm SN}}{10^{51}\ {\rm erg}}\right)^{1/2} \left(\frac{M_{\rm ej}}{M_\odot}\right)^{-1/2} {\rm km\ s^{-1}}, \tag{2.3}$$

$$R_{\rm sh} = v_{\rm sh} t, \tag{2.4}$$

where t is the time from the SN. $M_{\rm ism}$ can be calculated as follow:

$$M_{\rm ism} = \frac{4}{3}\pi R_{\rm sh}^3 \mu m_{\rm H} n_0, \tag{2.5}$$

where n_0 is the hydrogen density in ISM. The free expansion phase continues until $M_{\rm ism}$ is comparable to $M_{\rm ej}$. From Equation (2.3), (2.4), (2.5), the timescale of this phase is a few hundred years:

$$t \sim 1.9\times10^2 \left(\frac{E_{\rm SN}}{10^{51}\ {\rm erg}}\right)^{-1/2} \left(\frac{M_{\rm ej}}{M_\odot}\right)^{5/6} \left(\frac{\mu}{1.4}\right)^{-1/3} \left(\frac{n_0}{1\ {\rm cm^{-3}}}\right)^{-1/3} {\rm yr}. \tag{2.6}$$

Adiabatic Expansion Phase (Sedov-Taylor Phase) When $M_{\rm ism}$ becomes much larger than $M_{\rm ej}$, the shock velocity decelerates due to swept-up ISM. In this phase, where the radiative cooling is still negligible, the SNR expands adiabatically. This phase is called the "adiabatic expansion phase (Sedov-Taylor phase)," where a self-similar solution (Sedov-von Neumann-Taylor solution) can give the shock radius, velocity, and temperature under an approximation of point source explosion (Sedov, 1946; Taylor, 1950; von Neumann, 1976):

$$R_{\rm sh} = 4\times10^{14} \left(\frac{t}{10^4\ {\rm yr}}\right)^{2/5} \left(\frac{E_{\rm SN}}{10^{51}\ {\rm erg}}\right)^{1/5} \left(\frac{n_0}{1\ {\rm cm^{-3}}}\right)^{-1/5} {\rm km}, \tag{2.7}$$

$$v_{\rm sh} = \frac{dR_{\rm sh}}{dt} = 5\times10^2 \left(\frac{t}{10^4\ {\rm yr}}\right)^{-3/5} \left(\frac{E_{\rm SN}}{10^{51}\ {\rm erg}}\right)^{1/5} \left(\frac{n_0}{1\ {\rm cm^{-3}}}\right)^{-1/5} {\rm km\ s^{-1}}, \tag{2.8}$$

$$T_{\rm sh} = 3\times10^6 \left(\frac{t}{10^4\ {\rm yr}}\right)^{-6/5} \left(\frac{E_{\rm SN}}{10^{51}\ {\rm erg}}\right)^{2/5} \left(\frac{n_0}{1\ {\rm cm^{-3}}}\right)^{-2/5} {\rm K}. \tag{2.9}$$

After the adiabatic expansion phase over $\sim 10,000$ years, 70% of the explosion energy transfers to thermal energy (Chevalier, 1974).

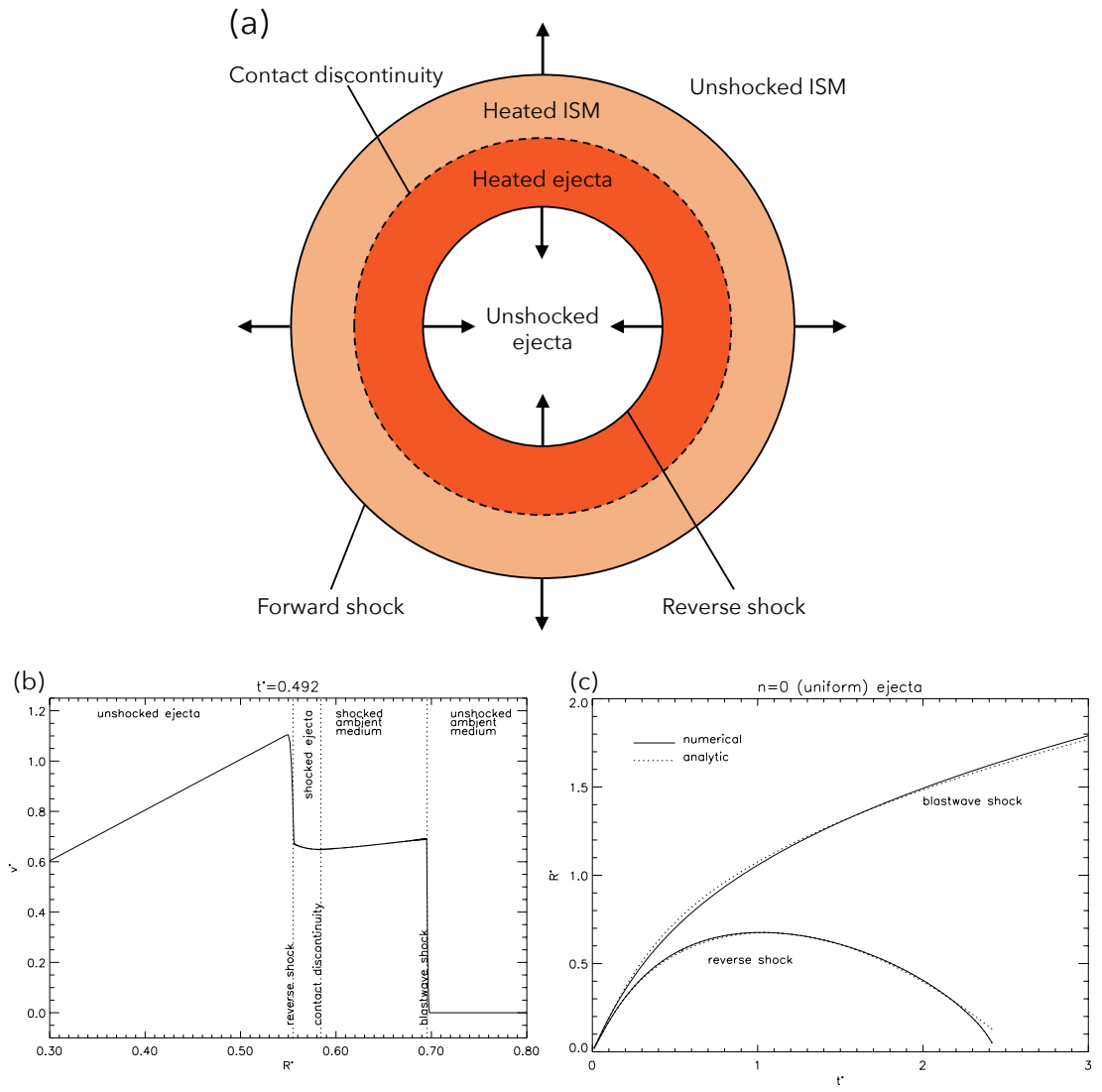

Figure 2.4: (a) Schematic of the cross-section of an SNR at the transition state from the free to adiabatic expansion phase. (b) The radius of the forward and reverse shock as a function of time (Truelove & McKee, 1999).

At the transition phase from the free to adiabatic expansion phase, the swept-up ISM pushes back on the ejecta, which is decelerated. It creates the shock, which moves towards the inner direction (reverse shock) (McKee, 1974). Figure 2.4 (a) shows the schematic of the SNR at the phase, and Figure 2.4 (b) shows the position and the velocity of the forward and reverse shock. As shown in Figure 2.4 (c), the shocks move over time. The X-rays can be detected from the forward-shocked ISM and reverse-shocked ejecta, which are heated to high enough temperatures. The boundary between the heated ISM and ejecta is called "contact discontinuity." Many young SNRs, such as Tycho's SNR and SN 1006, are thought to be categorized as a remnant in this phase.

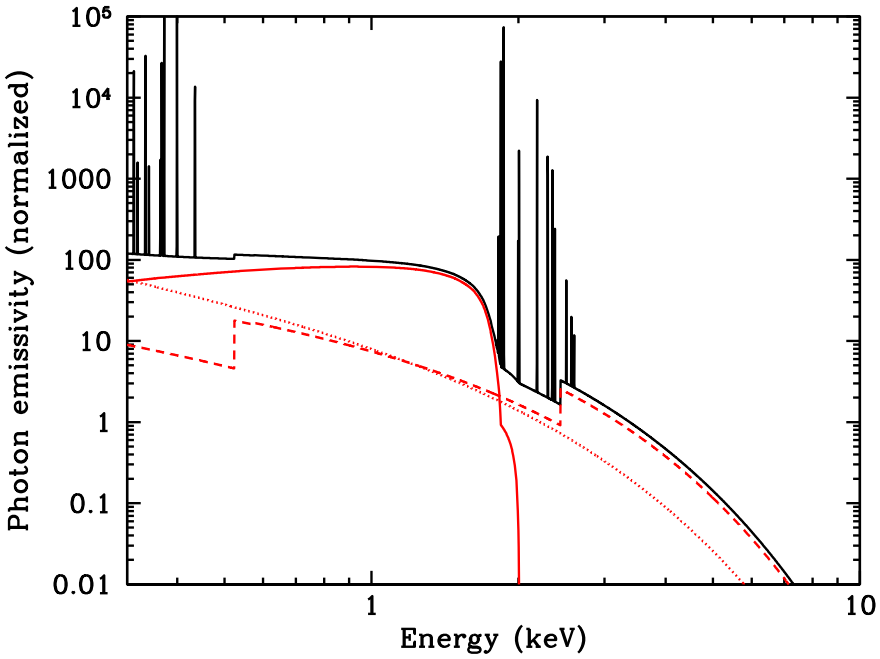

Figure 2.5: The emissivity of a plasma composed solely of silicon and not in ionization equilibrium (with parameters $kT_e = 1$ keV and $n_e t = 5 \times 10^{10}$ cm^{-3} s). The plot illustrates the contributions from two-photon emission (depicted by the red solid line), free-bound continuum (indicated by the red dashed line), and bremsstrahlung (free-free emission, represented by the red dotted line). Additionally, the total emissivity, encompassing Si-L- and Si-K-shell line emissions, is displayed (Vink, 2012).

Radiative Cooling Phase When $T_{\rm sh}$ becomes too low to ignore the radiative cooling, the expansion of the remnant is no longer adiabatic. This phase is called "radiative cooling phase." In the early phase of it, the outer region with high density is cooled by radiation. On the other hand, the inner region keeps adiabatical expansion because it has low density and high temperature. This phase is also known as "pressure-driven snowplow phase" because the remnant expands by the pressure of the inner ejecta (McKee & Ostriker, 1977). For the non-relativistic single atomic gas ($\gamma = 5/3$), the shock expansion of this phase has the dependency of

$$R_{\rm sh} \propto t^{2/7}. \tag{2.10}$$

When the ejecta is cooled further, the shock expands only by the momentum conservation. This phase is also known as "momentum-conserving snowplow phase" (Cioffi et al., 1988). The shock expands with the dependency of

$$R_{\rm sh} \propto t^{1/4}. \tag{2.11}$$

2.2.2 Thermal Radiation from Shock-Heated Particles

2.2.2.1 Contiuum Emission

Thermal X-ray spectra comprise continuum emission originating from bremsstrahlung (free-free emission), recombination continuum (free-bound emission), and two-photon emission, the latter arising from the radiative electron transition from a metastable quantum level. Figure 2.5 shows the three components from the plasma composed solely of silicon. The following gives an explanation of the radiative process of bremsstrahlung, which this thesis mainly relates to, in SNRs.

Bremsstrahlung (Free-free Emission) Bremsstrahlung radiation is produced as the result of decelerations or deflections of charged particles colliding with other particles (Rybicki & Lightman, 1985a). Since an ion with an atomic number Z is $1836Z$ times heavier than electrons, the ions are resistant to deceleration. Thus, most of the observed bremsstrahlung radiation originates from electrons. The emissivity of the bremsstrahlung from the plasma with the electron density n_e, ion density n_i, and fixed electron velocity v_e can be written as:

$$\varepsilon_{\rm ff}(v_e) = \frac{2^4\pi e^6}{3\sqrt{3}c^3 m_e^2 v_e} g_{\rm ff}(v,\nu) n_e \sum_i n_i Z_i^2, \tag{2.12}$$

where e, c, and m_e are the elementary charge, the light speed, and the electron mass, respectively. $g_{\rm ff}(v,\nu)$ is a gaunt factor, which is defined as:

$$g_{\rm ff}(v,\nu) \equiv \frac{\sqrt{3}}{\pi} \ln\left(\frac{m_e v^3}{e^2\nu}\right). \tag{2.13}$$

Observing SNR plasma in practice, the velocity v_e does not adhere to a single value as previously assumed but follows a Maxwell–Boltzmann distribution as expressed in Equation (1.21). Therefore, the emissivity from the plasma with the electron temperature T_e can be obtained by integrating the radiation from electrons with different velocities:

$$\varepsilon_{\rm ff} = \frac{2^5\pi e^6}{3m_e c^3}\left(\frac{2\pi}{3k_{\rm B}m_e}\right)^{1/2} T_e^{-1/2}\overline{g_{\rm ff}} \exp\left(-\frac{h\nu}{k_{\rm B}T_e}\right) n_e \sum_i n_i Z_i^2 \tag{2.14}$$

$$= 2.0\times10^{-41}\left(\frac{k_{\rm B}T_e}{\rm keV}\right)^{-1/2}\left(\frac{n_e}{\rm cm^{-3}}\right)\sum_i Z_i\left(\frac{n_i}{\rm cm^{-3}}\right) \tag{2.15}$$

$$\times\,\overline{g_{\rm ff}} \exp\left(-\frac{h\nu}{k_{\rm B}T_e}\right) \ {\rm erg\ s^{-1}\ Hz^{-1}\ cm^{-3}}.$$

Here, $\overline{g_{\rm ff}}$ is a velocity averaged gaunt factor, whose approximate value can be given from a review by Brussaard & van de Hulst (1962). The typical value in the X-ray emitting plasma can be expressed as:

$$\overline{g_{\rm ff}} = \left(\frac{3k_{\rm B}T_e}{\pi h\nu}\right)^{-1/2}. \tag{2.16}$$

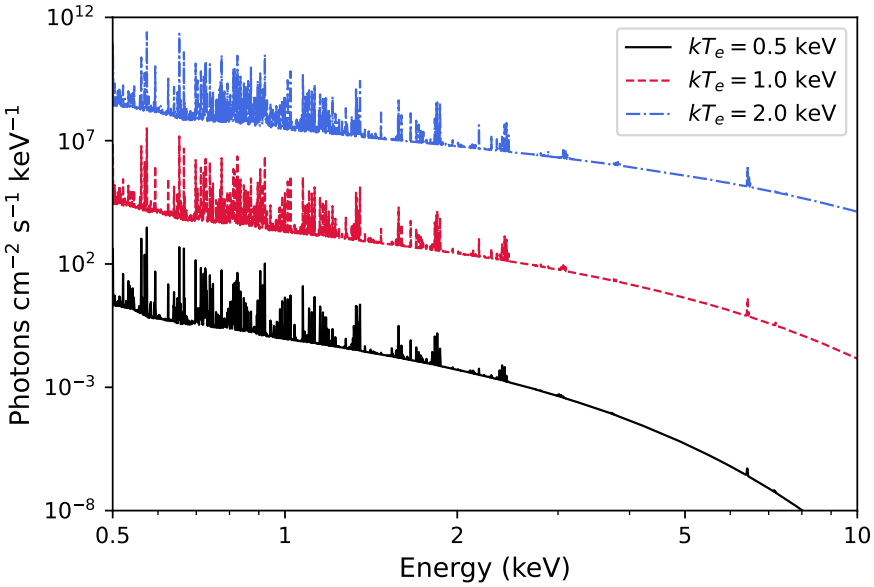

Figure 2.6: Examples of ionizing plasma model with parameters $n_e t = 1 \times 10^{10}$ cm^{-3} s and different kT_e. The model is made by the *vnei* model in the XSPEC tool. The abundance of each element is assumed to be solar composition. Solid, dashed, and dash-dotted curves represent the model when $kT_e = 0.5$, 1.0, and 2.0 keV multiplied by 1, 5×10^4, and 1×10^9, respectively.

Since the luminosity L of the plasma in a certain energy given by $\int dV \varepsilon_{\rm ff}$, it is proportional to $\int n_e n_H dV$ when elemental abundances are known. This factor is called emission measures (EMs), often used in spectral fitting codes.

Examples of radiations from X-ray emitting plasma with the solar composition are given in Figure 2.6. In the case of these abundances, The bremsstrahlung by electrons interacting with protons and helium ions is dominant. So, we observe the superposition of the radiation originating from these two particles. The emissivity depicted in Equation (2.15) can be approximated as the following:

$$\varepsilon \propto \begin{cases} (h\nu)^{-0.4} & (h\nu \leq kT_e) \\ \exp(-h\nu/kT_e) & (h\nu > kT_e). \end{cases} \tag{2.17}$$

Thus, the slope and the cutoff energy depend on the electron temperature of the plasma, as can also be seen from Figure 2.6. Conversely, using this, it is possible to estimate the electron temperature by analyzing the shape of the spectrum.

2.2.2.2 Line Emission

Emission lines are radiated from atoms whose electron bounded at a certain energy level transits to a lower energy level prompted by, e.g., collisional excitation, inner-shell ionization, and cascade decay following radiative recombination. The photon energy corresponds to the difference between the before and after states. Bohr's model can

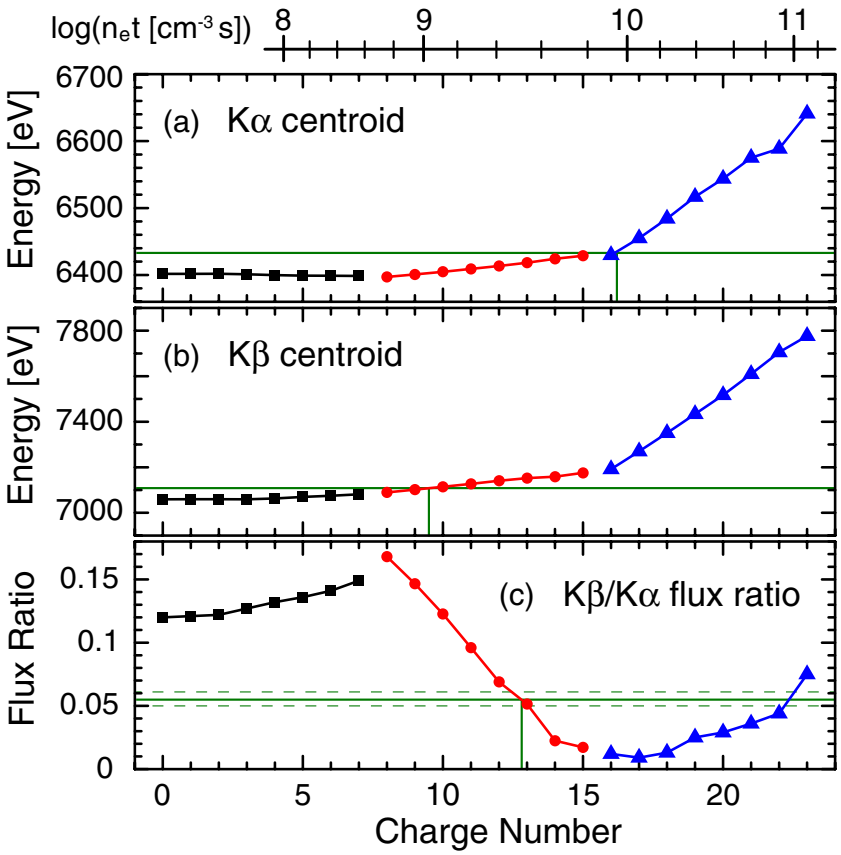

Figure 2.7: Centroid energies of the Fe Kα lines (top), and Feβ lines (middle) and the flux ratio of Kβ/Kα (bottom) as a function of charge number of the Fe ion (Yamaguchi et al., 2014).

approximate emission energies from ions with an electron (H-like ions). When an electron transits from quantum number n to n', the energy is:

$$E \simeq hcR_\infty Z^2 \left(\frac{1}{n^2} - \frac{1}{n'^2} \right), \tag{2.18}$$

where R_∞ is Rydberg constant ($= 1.00 \times 10^7$ m^{-1}). Complex calculations are needed to obtain the line energies from the ions in other ionization states. We can access the line energies from the atomic database such as AtomDB (Foster et al., 2017) and SPEX (Kaastra et al., 1996). Figure 2.7 shows the centroid energies of Fe Kα and Fe Kβ lines in different ionization states and the flux ratio between the two lines. As can be seen from the figure, the centroid energies generally increase as the ionization state increases.

The electron temperature of plasma can be measured using the line intensity ratio emitted from the same ion. The observed flux ratio of two lines with energies E_1 and E_2 can be depicted as:

$$\frac{F_1}{F_2} = \frac{\Omega_1}{\Omega_2} \exp\left(\frac{E_2 - E_1}{kT_e} \right) \exp\left[(\sigma_{E_2} - \sigma_{E_1}) N_\mathrm{H} \right], \tag{2.19}$$

where Ω and σ_E are the effective oscillator strength and photo-electronic absorption cross section at energy E, respectively. This equation represents the modified emissivity

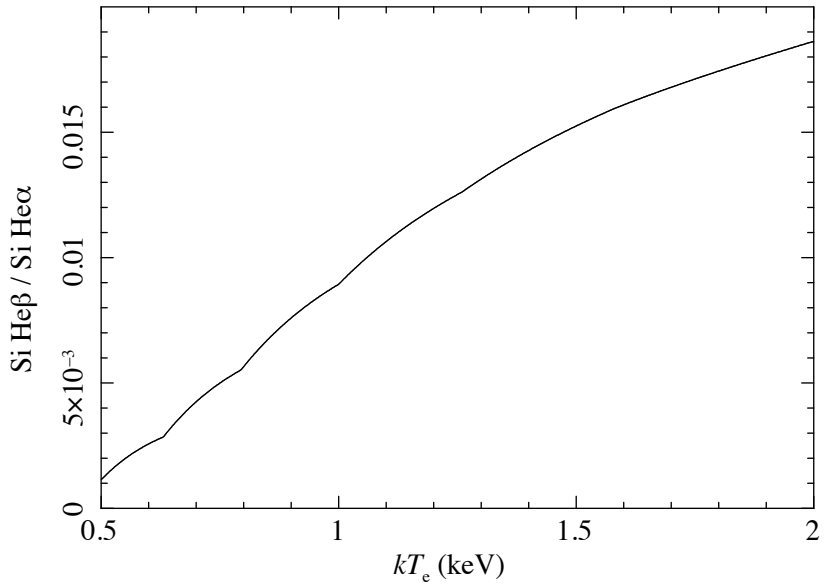

Figure 2.8: Intensity ratio of Si Heβ/Si Heα lines as a function of the electron temperature kT_e when the ionization timescale of $n_e t = 10^{11}$ cm^{-3} s (Katsuda, 2023).

ratio by a factor of the relative interstellar absorption at the two lines. For instance, the line intensity ratio of Si Heβ/Si Heα varies strongly depending on electron temperature kT_e as shown in Figure 2.8.

2.2.3 Non-thermal Radiation from Shock-Accelerated Electrons

In the X-ray band, the synchrotron radiation is mainly observed from electrons that are accelerated to the relativistic velocities by DSA, indeed observed in many SNRs (e.g. Koyama et al., 1995; The et al., 1996; Koyama et al., 1997). It is emitted due to the influence of the Lorentz force (see also Ginzburg & Syrovatskii (1965) and Rybicki & Lightman (1985b) for reviews). The power per frequency ω from an electron with a given velocity $\beta = v/c \simeq 1$ is:

$$P(\omega) = \frac{\sqrt{3}e^3 B\beta^2 \sin\alpha}{2\pi m_e c^2} F\left(\frac{\omega}{\omega_c}\right), \tag{2.20}$$

where α and B are the pitch angle (the angle between the velocity and field) and the magnetic field, respectively. The critical frequency ω_c is defined as:

$$\omega_c \equiv \frac{3e\gamma^2 B \sin\alpha}{2m_e c}. \tag{2.21}$$

The formula $F(\omega/\omega_c)$ is defined as the following using the Bessel function of order 5/3 ($K_{5/3}(\xi)$):

$$F(\omega/\omega_c) \equiv \frac{\omega}{\omega_c} \int_{\omega/\omega_c}^{\infty} K_{5/3}(\xi) d\xi. \tag{2.22}$$

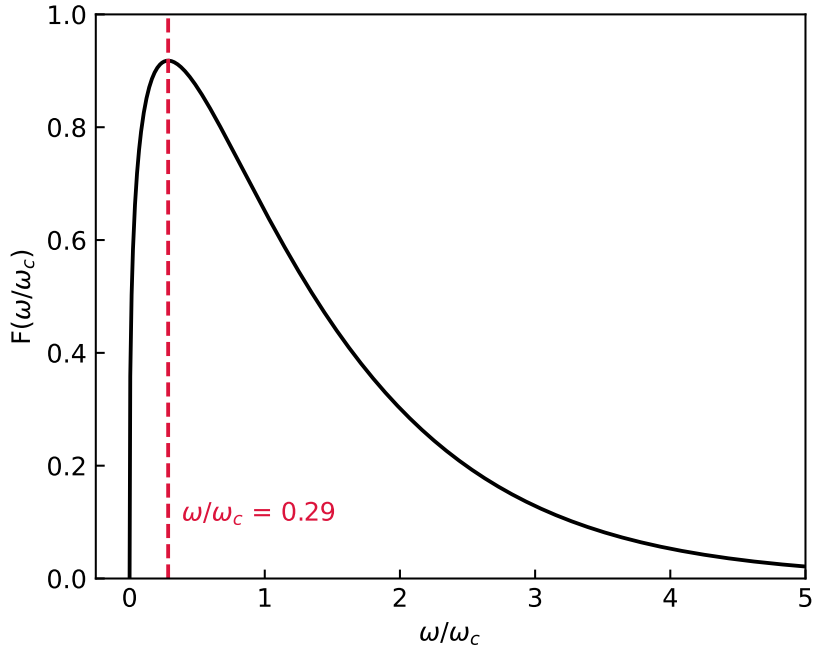

Figure 2.9: The spectral shape of synchrotron radiation from a single electron. The dotted line shows the position of the peak energy.

The synchrotron spectrum from an electron has a shape as depicted in Figure 2.9. The spectrum has a peak at the frequency of $\omega \simeq 0.29\omega_{\rm c}$. The averaged photon energy from the electron with energy E_e can be approximated as:

$$\varepsilon \simeq 2\left(\frac{B}{10\ \mu\mathrm{G}}\right)\left(\frac{E_e}{100\ \mathrm{TeV}}\right)^2\ \mathrm{keV}. \tag{2.23}$$

The total emitting power can be given from the Lamor formula:

$$P_{\rm synch} = \frac{4}{3}\sigma_{\rm T} c\beta^2\gamma^2 U_B, \tag{2.24}$$

where $\sigma_{\rm T} = 8\pi r_0^2/3$ is the cross-section of Thomson scattering with the classical electron radius $r_0 \equiv e^2/(m_e^2 c)$, $U_B = B^2/(8\pi)$ is the energy density of the magnetic field B. Equation (2.24) also can be given by the integral of Equation (2.20) over ω. When both electron and proton have the same energy E, the power ratio is

$$\frac{P_p}{P_e} = \left(\frac{m_e}{m_p}\right)^4 \simeq 9\times10^{-14}, \tag{2.25}$$

using $\sigma_{\rm T} \propto m^{-2}$, $\gamma = E/(mc^2)$. Therefore, the synchrotron emissivity of protons is much less than that of electrons. Otherwise, the electrons have high emissivity, making them more susceptible to energy loss through radiation. This energy loss is called "synchrotron cooling," whose timescale is given by $t_{\rm loss} = E/|dE/dt|$. Because $|dE/dt|$ is equivalent to Equation 2.24, the timescale $t_{\rm loss}$ can be expressed as:

$$t_{\rm synch} = \frac{3m_e c^2}{4\sigma_{\rm T} c U_B \gamma} \simeq 12.5\left(\frac{E_e}{100\ \mathrm{TeV}}\right)^{-1}\left(\frac{B}{100\ \mu\mathrm{G}}\right)^{-2}\ \mathrm{yr}. \tag{2.26}$$

When the energy distribution of particles is expressed power law as depicted in Equtation 1.32, the photon energy spectrum can derive from the integral of the radiation from electrons:

$$\varepsilon \frac{dn}{d\varepsilon} = \int P(\omega) N(E) dE \tag{2.27}$$

$$= \varepsilon^{-(s-1)/2} \equiv \varepsilon^{-\alpha}. \tag{2.28}$$

Thus, photons also have a power-law spectrum. Its photon index Γ, which is defined as $dn/d\varepsilon \propto \varepsilon^{-\Gamma}$ has a relation of:

$$\Gamma = \alpha + 1 = \frac{s+1}{2}. \tag{2.29}$$

We can estimate the cutoff energy by combining Equation (2.23) and Equation (1.40), (1.41), (1.42):

$$\varepsilon_{\rm cutoff}^{\rm age} \propto \eta^{-2} v_{\rm sh}^4 B^3 t_{\rm age}^2, \tag{2.30}$$

$$\varepsilon_{\rm cutoff}^{\rm loss} \propto \eta^{-1} v_{\rm sh}^2, \tag{2.31}$$

$$\varepsilon_{\rm cutoff}^{\rm esc} \propto \lambda_{\rm max}^2 B^3, , \tag{2.32}$$

3

Time Variabilities of Supernova Remnant

Contents

3.1 Overview

Observations of time variabilities are typically used in studies of transient sources, such as novae (e.g., König et al., 2022), SNe (e.g., Foley et al., 2014; Jacobson-Galán et al., 2023), gamma-ray bursts (e.g., Abbott et al., 2017), and fast radio bursts (e.g., Enoto et al., 2021). These studies can offer insights into the real-time changes in their radiation processes or other states. On the other hand, it is difficult to observe rapid time variabilities in radiation from SNRs, which have passed several hundred years since their explosions. Considering their shocks with a high Mach number, it seems natural for the plasma to undergo rapid time variabilities. One possible reason why the variabilities cannot be observed is that we might have missed them even though they actually occur. Observatories with high-resolution imaging, such as Chandra and Hubble Space Telescope (HST), can help us detect time variabilities in SNRs on small scales.

3.2 Changes in X-ray Spectrum and Flux

The first detection of X-ray time variability in SNR is nonthermal flux changes in the shell of RX J1713.7−3946 discovered by Uchiyama et al. (2007). Figure 3.1 shows the nonthermal X-ray brightening and decay that they discovered from high-resolution images taken by Chandra. They found the time variabilities on a one-year timescale with the

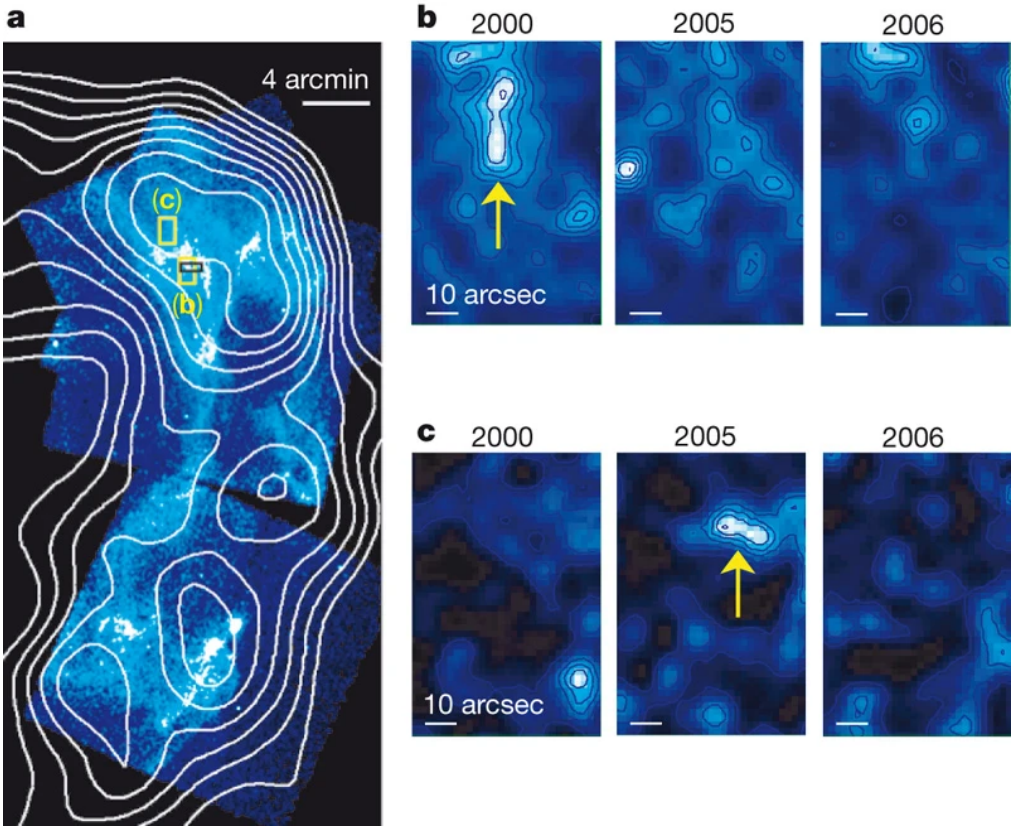

Figure 3.1: Flux change of synchrotron X-ray in RX J1713.7−3946 reported by (Uchiyama et al., 2007). The contours in panel (a) show the TeV gamma-ray emission obtained from HESS measurement. Panel (b) and (c) is the zoom-in view of the yellow regions in panel (a).

sub-pc scale. The flux decay was interpreted as a result of a decrease of the electron cutoff energy due to the rapid synchrotron cooling, while the flux increase can be caused by the boosted DSA efficiency and/or amplified magnetic field. Thus, the decay and brightening timescale can be equivalent to the synchrotron loss and DSA acceleration time. From the Equations (1.39) and (2.23), the acceleration time can be described as:

$$t_{\rm acc} \simeq 1\eta \left(\frac{\varepsilon}{\rm keV}\right)^{0.5} \left(\frac{B}{\rm mG}\right)^{-1.5} \left(\frac{v_{\rm sh}}{3000\ {\rm km\ s^{-1}}}\right)^{-2} {\rm yr}. \tag{3.1}$$

Whereas the cooling loss time can be written as follows using Equation (2.23) and (2.26):

$$t_{\rm synch} \simeq 1.5 \left(\frac{B}{\rm mG}\right)^{-1.5} \left(\frac{\varepsilon}{\rm keV}\right)^{-0.5} {\rm yr}. \tag{3.2}$$

Therefore, they suggested that the magnetic field in the region where the variability was observed is required to be amplified to $B > 1$ mG, considering the measured shock velocity $v_{\rm sh} < 4500$ km s^{-1}. Conversely, the time variabilities of nonthermal radiation can be a probe for the magnetic field amplification that induces fast acceleration and synchrotron cooling. Such rapid time variabilities in synchrotron X-rays are subsequently discovered in several other young SNRs, such as Cassiopeia A (Uchiyama &

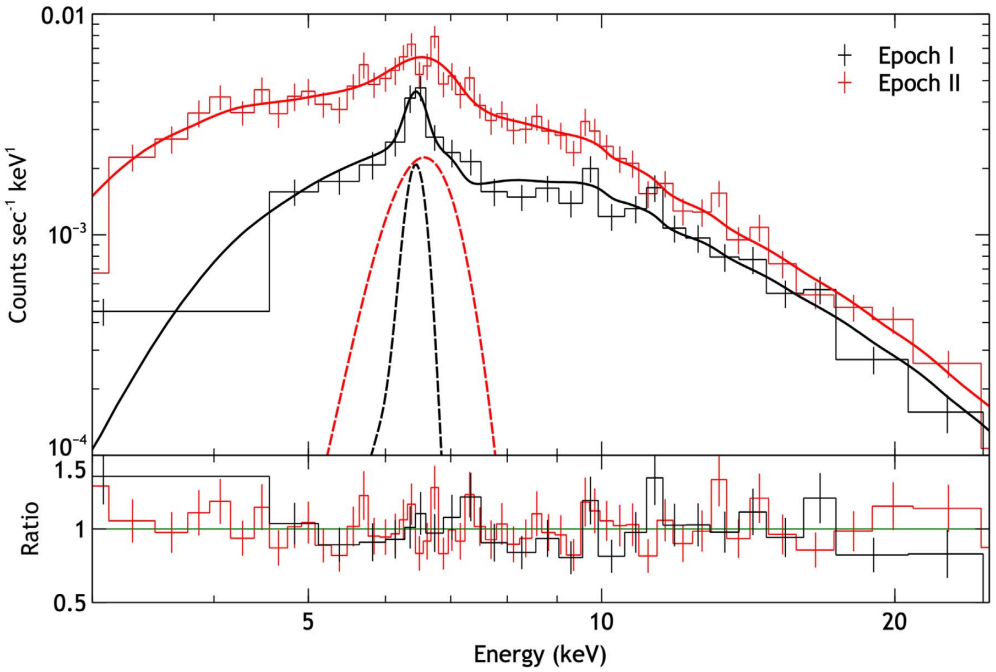

Figure 3.2: The spectra of SN 2023ixf in M101 at 4 and 11 days from its explosion (Grefenstette et al., 2023). The solid and dashed curves show the best-fit model and a Gaussian component for the Fe Kα line, respectively.

Aharonian, 2008; Patnaude & Fesen, 2009), G330.2+1.0 (Borkowski et al., 2018), and Tycho's SNR (Okuno, Matsuda, et al., 2020).

In the case of thermal X-rays, time variabilities in SNRs are limited to a few examples, whereas they are often discovered in earlier phases after SNe. Grefenstette et al. (2023) detected hard X-rays from SN 2023ixf in a nearby galaxy M101 at 4 (Epoch I) and 11 (Epoch II) days from its explosion. As seen in Figure 3.2, counts in Epoch II get brighter than in Epoch I, which they interpreted as a result of the rapidly decreasing absorption based on their spectral analysis. In the latter phase, the earliest stage of the SNR evolution, SN 1987A has been observed with X-ray observatories and detected in X-rays from shock-heated ISM (e.g., Burrows et al., 2000; Michael et al., 2002; Park et al., 2004; Miceli et al., 2019). Park et al. (2005) reported a rapid increase in flux in the 0.5–2 keV band approximately 6000 days after the explosion, based on data from ROSAT and Chandra. They also observed a transition in the soft X-ray distribution from being localized to becoming more widespread. These findings were interpreted as evidence of the blast wave reaching the main body of the dense CSM. Some recent studies also reported the ongoing spectral changes (e.g., Sun et al., 2021; Ravi et al., 2021).

Year-scale X-ray time variabilities are rarely detected in SNRs, even in young ones. As the only example known to us, we can mention Cassiopeia A, a young Galactic SNR (Rutherford et al., 2013; Patnaude & Fesen, 2007, 2014). Brightening features identified by Patnaude & Fesen (2014), with a size of 10^{15-16} cm, show correlations with optical Si XIII images (panel a and b in Figure 3.4). Through a temporal and spatial comparison between the X-ray and optical emissions, they discovered (1) time delays of appearance

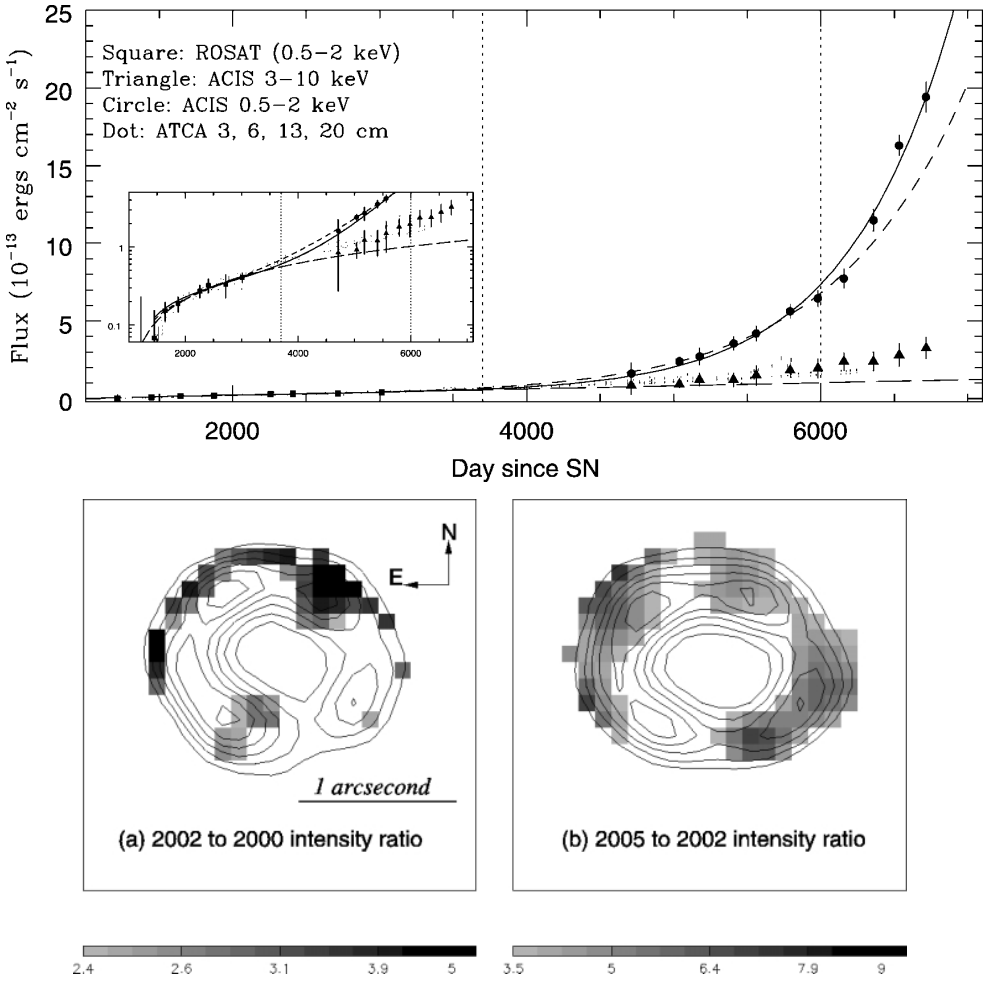

Figure 3.3: X-ray light curves of SN 1987A and intensity ratio in the 0.5–2.0 keV (Park et al., 2004).

between optical and X-ray features and (2) displacements on the arcsec scale between the optical and X-ray features. They explained these behaviors as originating from ejecta with highly inhomogeneous density, as depicted in Figure 3.4 (c). From their results, we can expect to detect time variabilities on a small scale in SNRs with a large apparent diameter.

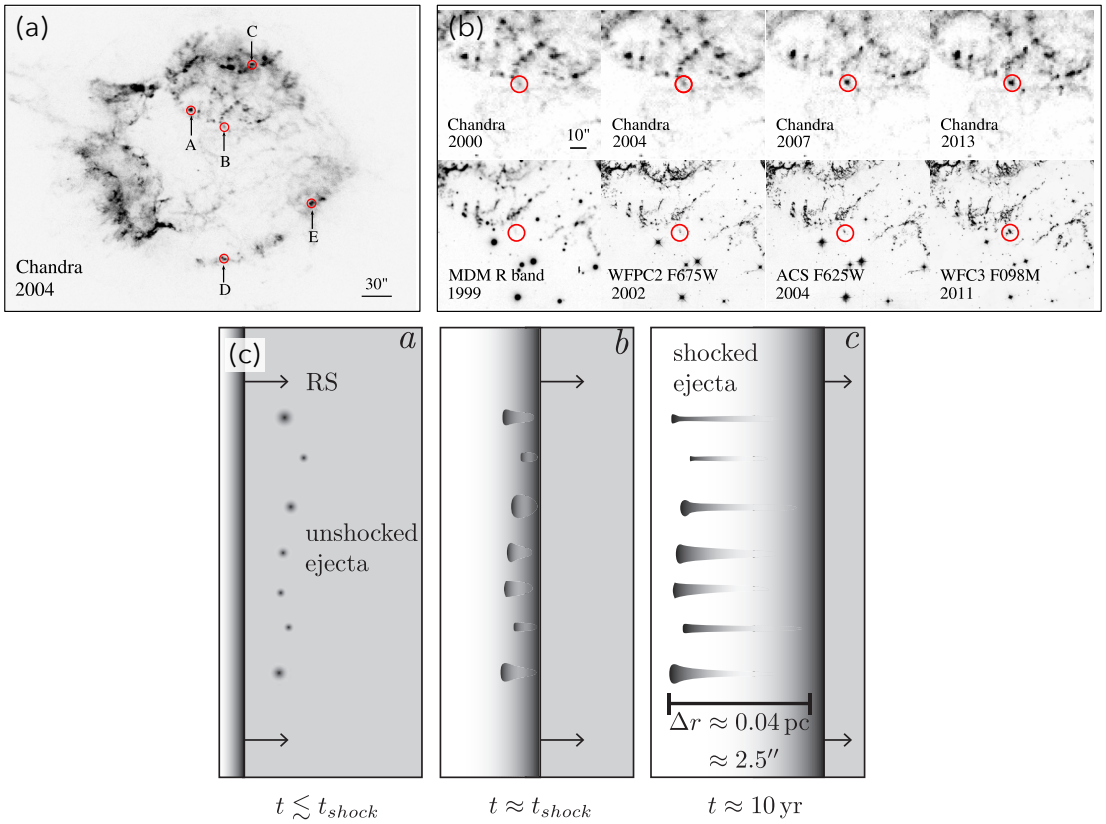

Figure 3.4: (a): The Chandra images of Cassiopeia A. (b): Zoom-in view of the time variable feature marked as "B" in panel (a). (c): Schematic of the density profile of the time variable features (Patnaude & Fesen, 2014).

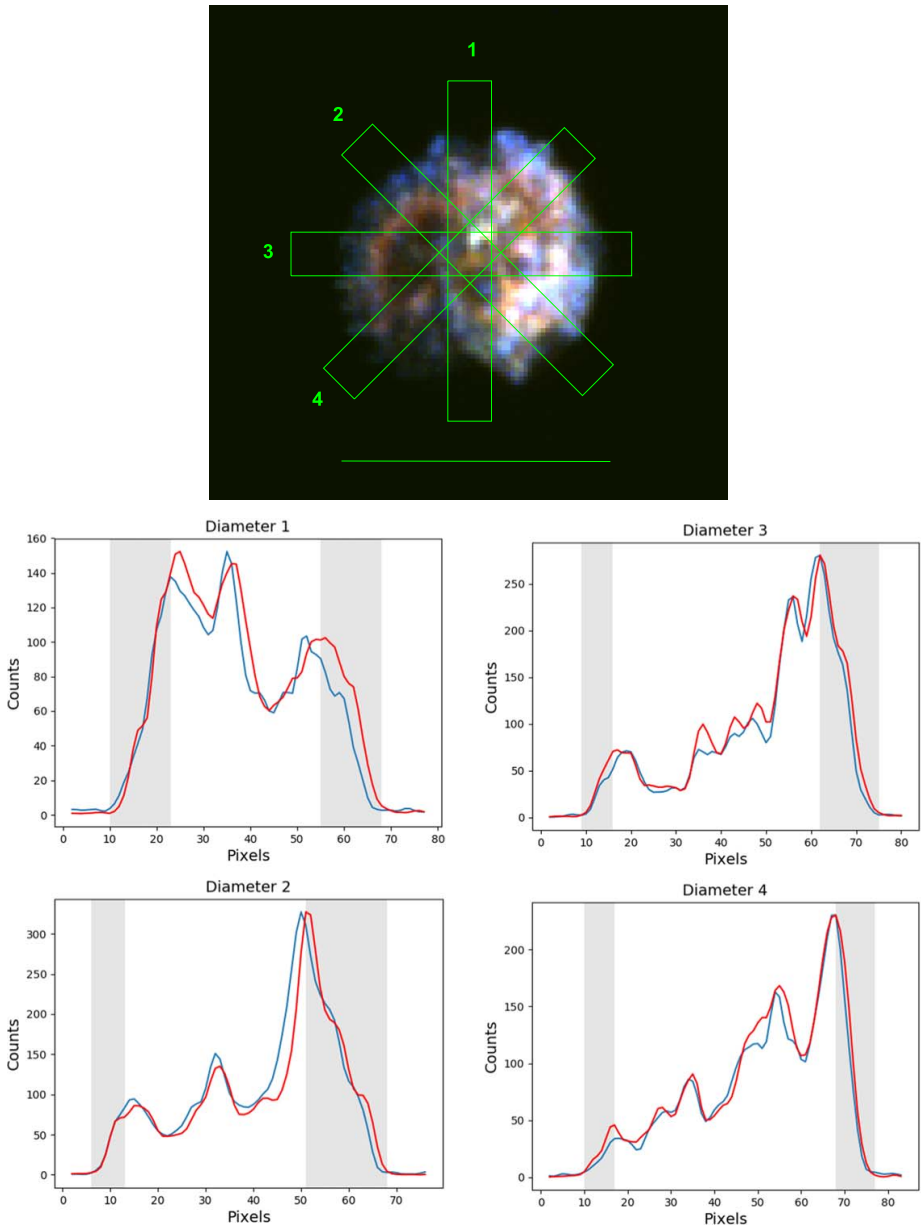

Figure 3.5: The expansion of SNR N103B from 1999 to 2017 (Williams et al., 2018). (Left): Chandra X-ray image of N103B with the energy band of 0.5–1.2 keV (red), 1.2–2.0 keV (green), and 2.0–7.0 keV (blue). Green boxes are the regions for extracting profiles. (Right): The extracted profiles in 1999 (blue) and 2017 (red).

3.3 Expansion of Blast waves and Ejecta

Since a typical young SNR expands with a velocity of about 10^{3-4} km s^{-1}, we can observe the expansion of a nearby ($\sim$ 1–10 kpc) SNR over ten years in arcsec scale. Recent observatories with excellent angular resolution (e.g., Hubble Space Telescope, Very Largy Array, and Chandra X-ray Observatory) have allowed us to measure the proper motions in parts of SNRs. The proper motions of metal-rich ejecta over many years

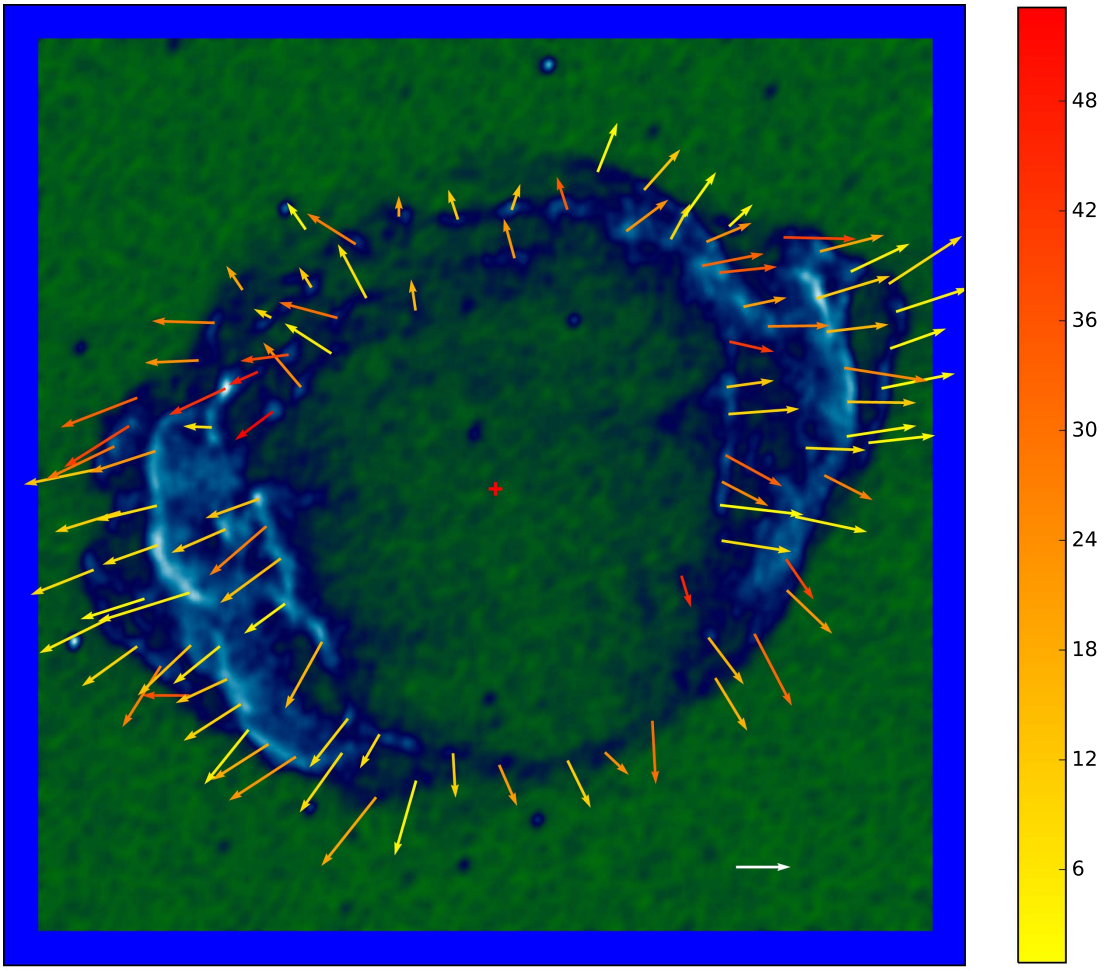

Figure 3.6: Chandra image of G1.9+0.3 in the 1.2–8.0 keV band and proper motion vectors of each feature (Borkowski et al., 2017). The color bar represents the deviations from radial in degrees. The length of the white allow corresponds to $0.''25\ \mathrm{yr}^{-1}$.

enable us to estimate the center of the explosions and explosion age. These values play an important role in studying the compact objects (Katsuda et al., 2018; Tsuchioka et al., 2021) or companion stars (Kerzendorf et al., 2019; Li et al., 2021). For example, using optical observations, Banovetz et al. (2021) estimated a center of explosion of 1E 0102.2−7219 from a measurement of 120 O-rich ejecta knots.

Although tracing the proper motions of fine structures is challenging in the extra-galactic SNRs, Williams et al. (2018) estimated expansion velocity through changes in the diameters of SNR 0509−68.7 (N103B) in the Large Magellanic Cloud (Figure 3.5). The measured expansion velocity is $4170^{+1280}_{-1310}\ \mathrm{km\ s^{-1}}$, suggesting an undecelerated age of 850 years and a somewhat younger real age. Expansion measurements are also reported in other extra-galactic SNRs, such as 1E 0102.2−7219 (Xi et al., 2019), 0509−67.5 (Hovey et al., 2015; Helder et al., 2010; Roper et al., 2018; Guest et al., 2022), 0519−69.0 (Guest et al., 2023).

We can obtain further insights from the expansion of Galactic SNRs because we can accurately measure shock velocities and discuss their spatial variation. The study of

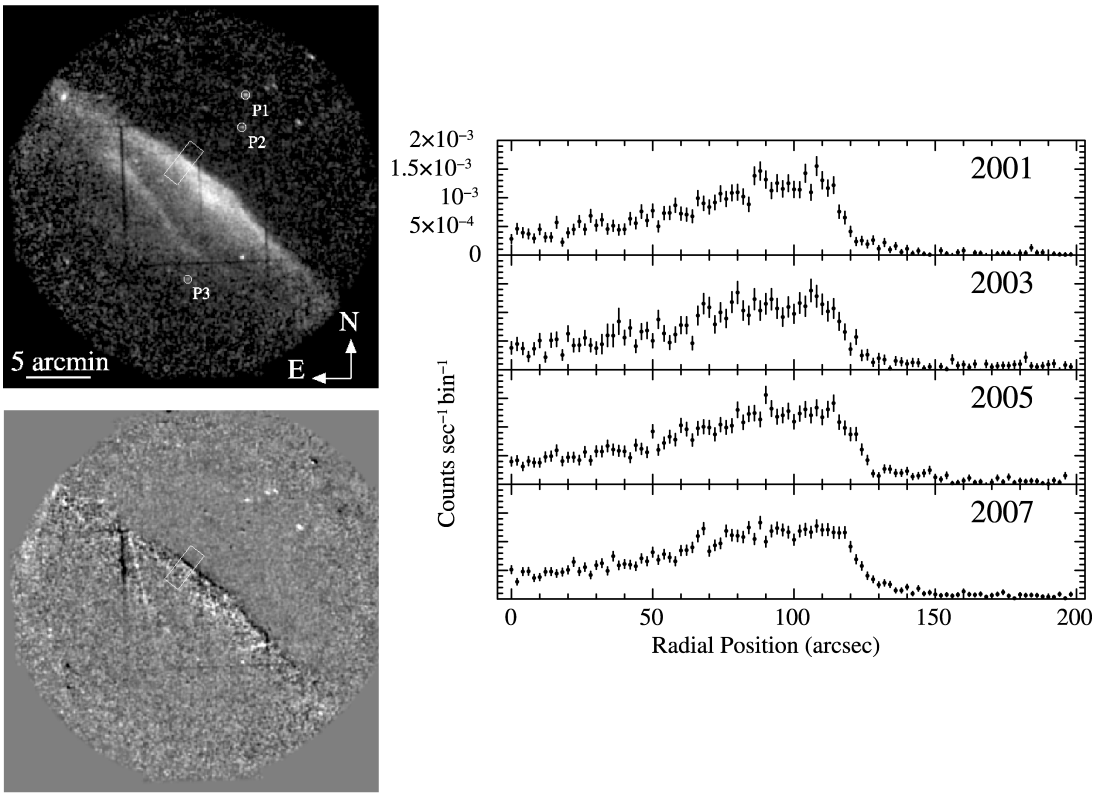

Figure 3.7: The shock proper motion in RX J0852.0−4622 (Vela Jr.) (Katsuda et al., 2008a). Left-top: XMM-Newton image in the 1.5–8.0 keV band obtained in 2001. The box represents the region for extracting the flux profile. Top-bottom: An image in 2001 subtracted from one in 2007. Right: The profile in each year extracted from the box in the left-top panel.

G1.9+0.3 by Borkowski et al. (2017) can be cited as an example that revealed large spatial variation in the remnant expansion (Figure 3.6). They suggested that the slow shocks are caused by the collision of SN ejecta with a dense CSM, indicating the asymmetric distribution of CSM. Such indications of ambient material are also discovered from the expansion measurements of other SNRs, including Kepler's SNR (Katsuda et al., 2008b), Cassiopeia A (e.g., Sato et al., 2018), SN 1006 (Katsuda et al., 2013), and RX J1713.7−3946 (e.g., Acero et al., 2017; Tanaka et al., 2020).

Accurate measurement of the shock proper motion also enables us to determine the remnant age and distance. Katsuda et al. (2008a) reported an expansion measurement in RX J0852.0−4622 (Vela Jr.) with XMM-Newton image in the 1.5–8.0 keV band (Figure 3.7). Their result indicated its expansion rate of 0.023% ± 0.006% per year, which is five times lower than those of young SNRs less than 1000 years. Such a slow velocity suggested that Vele Jr. was younger (1700–4800 years) than had been commonly expected. Additionally, they estimated the distance to the remnant to be $\sim$ 750 pc under an assumption of high shock velocity $\sim$ 3000 km s^{-1}.

Tanaka et al. (2021) reported the proper motion of the synchrotron X-rays at the forward shock of Tycho's SNR using Chandra data over 12 years. Figure 3.8 shows the

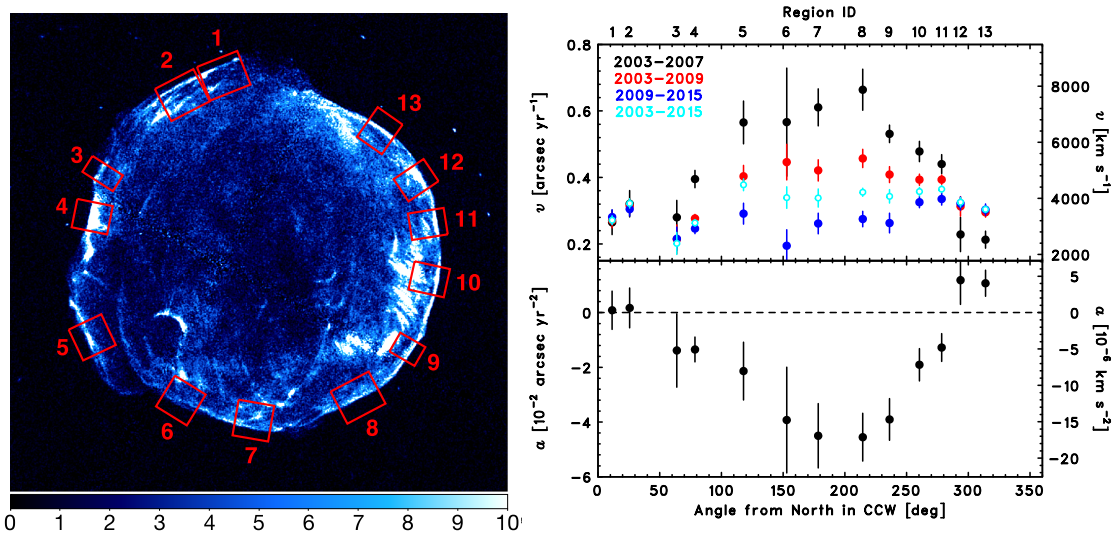

Figure 3.8: The decelerations of the blast waves in Tycho's SNR reported by (Tanaka et al., 2021). The red regions in the left panel show the regions for the shock velocity analysis. The right-top panel shows the shock velocity in each interval of the years. The right-bottom panel shows the acceleration rate in each region.

time variabilities of the blast waves. As can be seen in the figure, a rapid deceleration is revealed in the southwest blast waves (especially Regions 6–11). They interpreted it as the result of a recent hit on a dense wall around the remnant. The SD scenario can explain the dense wall, considering that the wind from a progenitor white dwarf during mass accretion can create the cavity wall, while there is no plausible interpretation in the DD scenario. Their results provided constraints on the progenitor activity before the expansion.

4

Instruments

Contents

4.1 Overview of Chandra X-ray Observatory

The Chandra X-ray Observatory is a telescope, which is still active, launched aboard the Space Shuttle Columbia by NASA on July 23rd, 1999 (Weisskopf et al., 2000). Its orbit is an elliptical shape with a perigee altitude of 16,000 km and an apogee altitude of 134,000 km. This orbit makes the period 64.3 hours, enabling the telescope to observe 55 hours continuously without interruption from the Earth's radiation belts (Chandra X-ray Center, 2023b).

Figure 4.1 shows the overview of the Chandra X-ray Observatory. Its dimensions, excluding the solar arrays, are 13.8 m × 19.5 m, and it weighs 4800 kg. The High Resolution Mirror Assembly (HRMA) is responsible for generating images on the focal plane with the half-power diameter (HPD) of the point spread function (PSF) of $< 0.''5$. The imaging capabilities are supported by two types of cameras: the Advanced CCD Imaging Spectrometer (ACIS) and the High Resolution Camera (HRC). Between the HRMA and

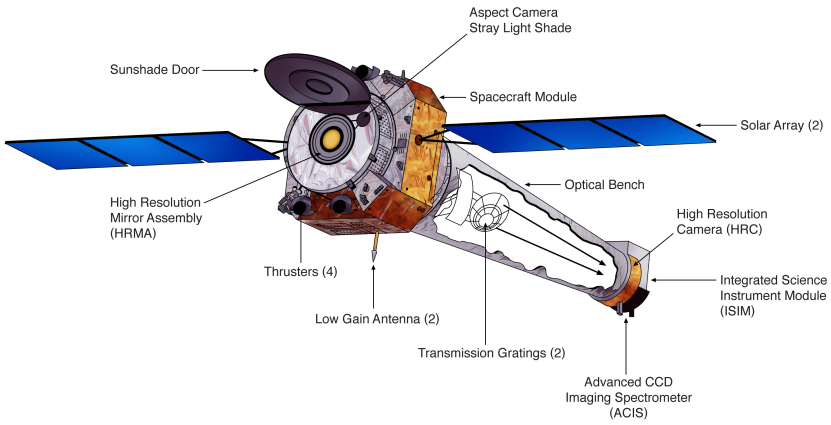

Figure 4.1: The Overview of Chandra X-ray Observatory (Credit: NGST & NASA/CXC).

the focal-plane cameras, there are two grating systems: the low-energy transmission grating (LETG) and the high-energy transmission grating (HETG). In this thesis, we explain the HRMA (Section 4.2) and the ACIS (Section 4.3), as these instruments are used in our research.

4.2 High Resolution Mirror Assembly (HRMA)

4.2.1 Layout

The X-ray telescope, HRMA, of the Chandra X-ray Observatory is highly renowned for its exceptional resolution, measuring less than 0.″5. The HRMA comprises a nested set of four mirror pairs configured to form Wolter-I type optics (Figure 4.2). Each mirror pair consists of a paraboloid as the front mirror and a hyperboloid as the back mirror. The

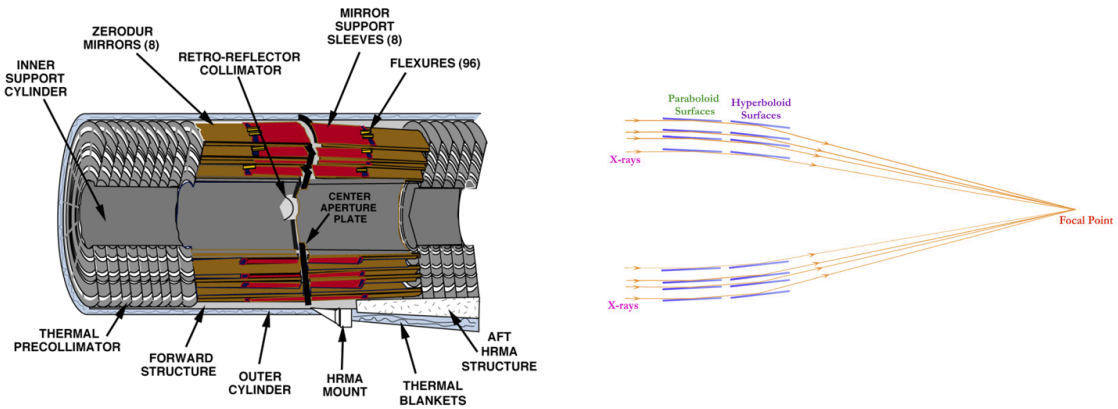

Figure 4.2: Left: Four HRMA mirror pairs and associated structures (Arenberg et al., 2014). Right: Schematic of grazing incidence of Wolter-I type optics (Credit: NASA/CXC/S. Lee).

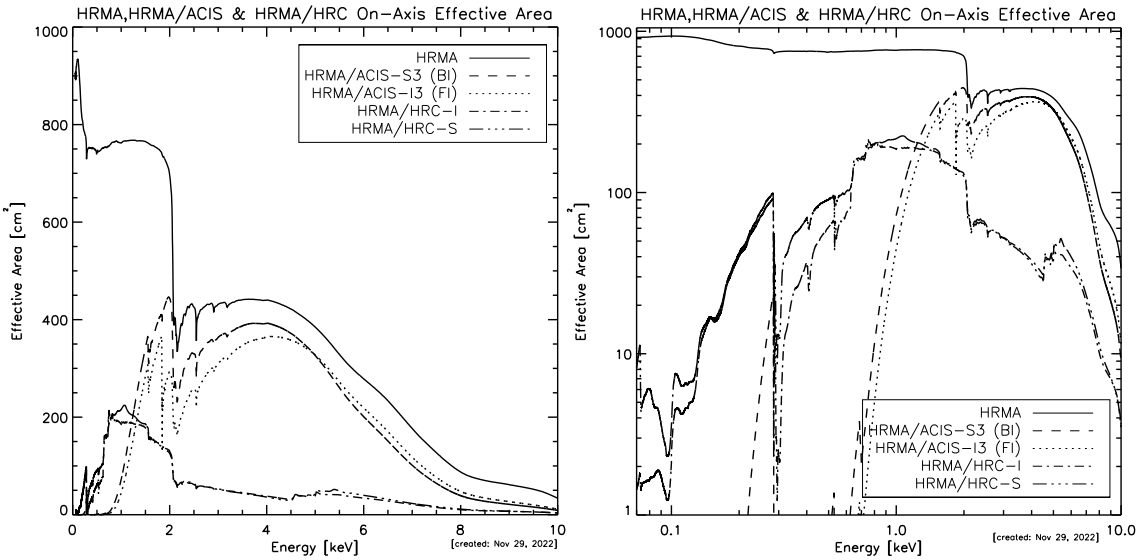

Figure 4.3: The effective area of HRMA, HRMA/ACIS, and HRMA/HRC against X-ray energy in linear-linear (left) and log-log (right) scale. The effective areas of HRMA/ACIS and HRMA/HRC are determined by multiplying the effective area of HRMA with the quantum efficiency of each detector at its aimpoint (Chandra X-ray Center, 2022).

length of each mirror is 84 cm, and the total length between pre- and post-collimator is 276 cm. The focal length is 10.070 ± 0.003 m.

4.2.2 Effective Area

The HRMA unobstructed geometric aperture measures 1145 cm^2. Supporting struts partially block the HRMA aperture, accounting for less than 10% obstruction. Consequently, the HRMA throughput varies with X-ray energy due to the dependence of optical reflectivity on both photon energy and grazing angle. Figure 4.3 (solid lines) shows the HRMA effective area released in CALDB 4.1.1. The values change around the iridium M-edge near 2 keV, with ~ 800 cm^2 on the low-energy side (0.1–2 keV)

Table 4.1: The properties of major X-ray observatories

Observatories	Mirrors	Detectors	Energy Range (keV)	Effective Area (cm^2)	HPD (arcsec)	References
Chandra	HRMA	ACIS	0.1–10	400 @ 5 keV	0.5	[1]
XMM-Newton	—	EPIC	0.1–10	1500 @ 2 keV	~ 15	[2,3]
Suzaku	XRT	XIS	0.2–12	440 @ 1.5 keV	120	[4]
Hitomi	SXT	SXI	0.4–12	590 @ 1 keV	~ 70	[5]
	HXT	HXI	5–80	174 @ 30 keV	~ 100	
NuSTAR	—	FPM	3–78.4	100 @ 30 keV	58	[6, 7]
XRISM	XMA	Xtend	0.3–12	~ 435 @ 6 keV	~ 1.′3	[8]

[1] Chandra X-ray Center (2022), [2] Jansen et al. (2001), [3] Aschenbach (2002), [4] Mitsuda et al. (2007)
[5] Takahashi et al. (2018), [6] Harrison et al. (2013), [7] Brejnholt et al. (2012), [8] XRISM Science Team (2020)

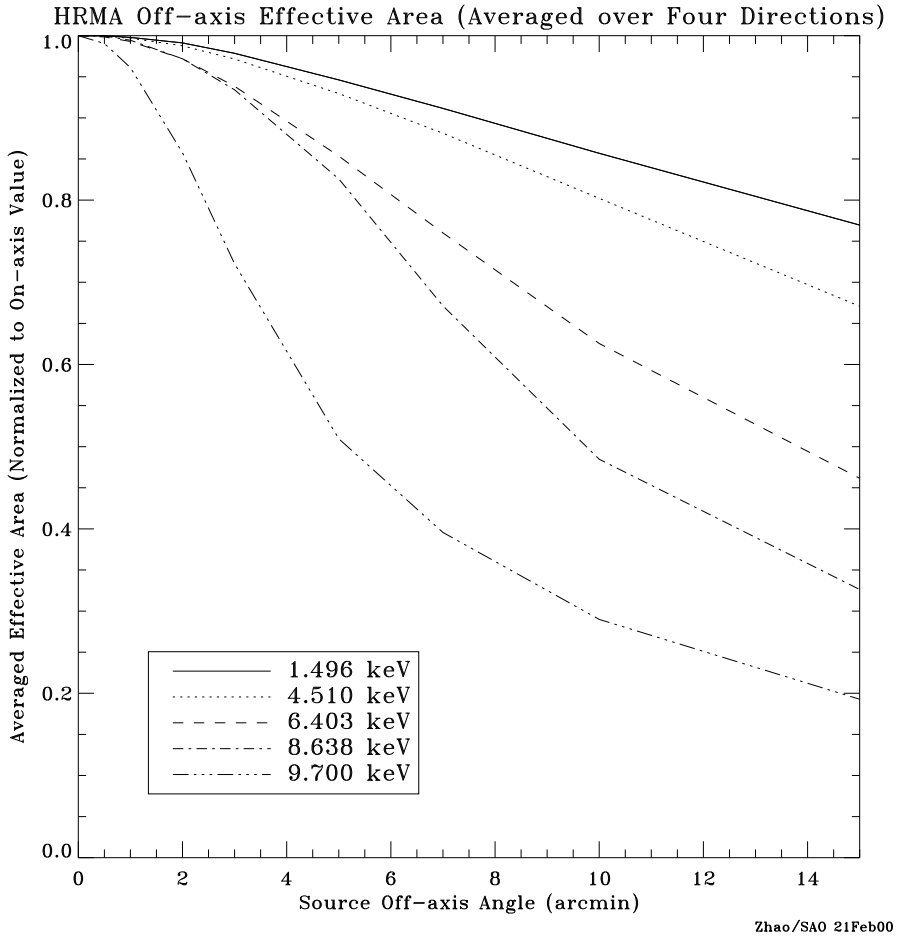

Figure 4.4: The HRMA effective area as a function of the off-axis angle of the position of the source (Chandra X-ray Center, 2022).

and ~ 300 cm^2 on the high-energy side (2–6 keV). As the photon energy increases, the effective area decreases, and it becomes almost insensitive around 10 keV.

The effective area also depends on the off-axis angle, as can be seen in Figure 4.4 (also known as vignetting). This is attributed to the reduction in the effective aperture of the telescope due to off-axis displacement, as well as the increased area where X-rays cannot be reflected due to the larger incidence angle. The effective area decreases more at off-axis angles as the photon energy increases. We analyze the X-ray data considering this effect and apply corrections accordingly.

4.2.3 Point Spread Function

As mentioned above, the angular resolution of the HRMA is superior to other X-ray observatories, constituting one of the notable attributes of the Chandra X-ray Observatory. Figure 4.5 shows the fractional encircled energy function (EEF) of the HRMA calculated for an on-axis point source. EEF is calculated by dividing the integrated energy of the point spread function (PSF) within a given radius by the total energy of the PSF. The

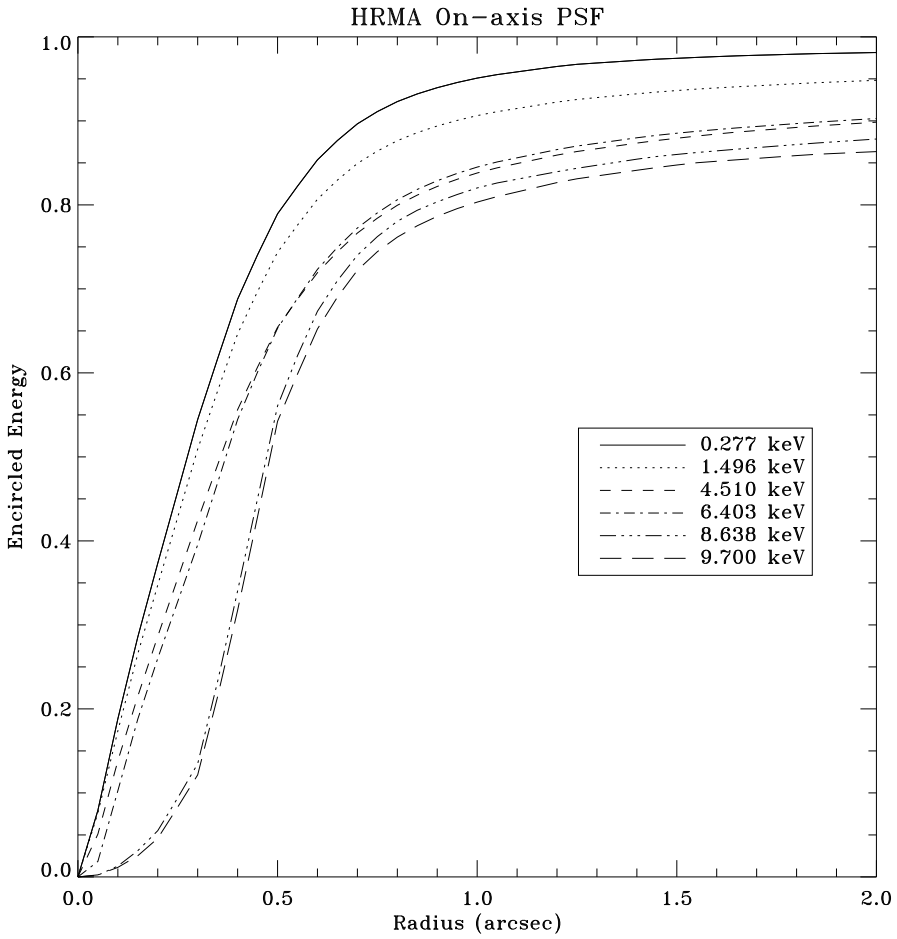

Figure 4.5: The encircled energy of HRMA versus angular radius generated for selected X-ray energies, assuming an on-axis point source (Chandra X-ray Center, 2022).

diameter where the EEF reaches 50% is called the half power diameter (HPD), which is often used to represent the angular resolution. Table 4.1 provides a reference for the properties of major X-ray observatory mirrors. It can be seen that HRMA has an angular resolution of 0.″5 that is at least an order of magnitude superior to other observatories.

4.3 Advanced CCD Imaging Spectrometer (ACIS)

4.3.1 Layout

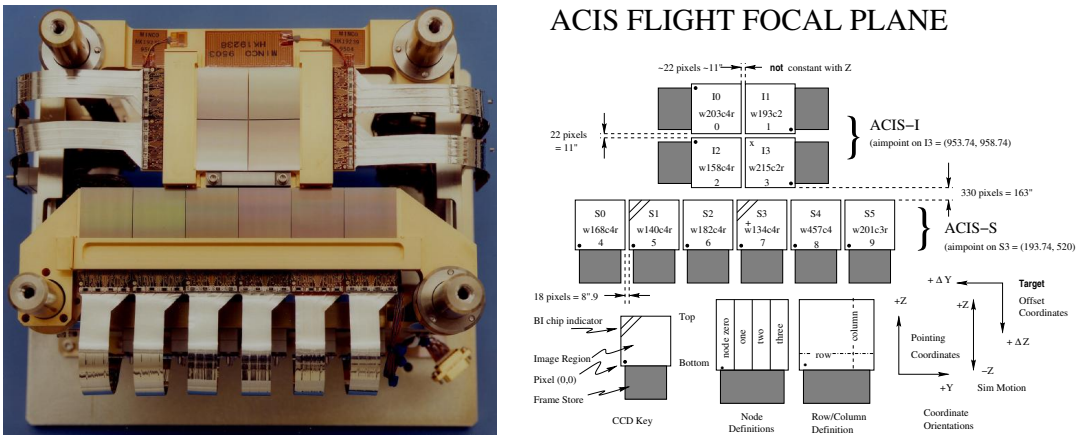

Figure 4.6: The Layout of ACIS (Chandra X-ray Center, 2022).

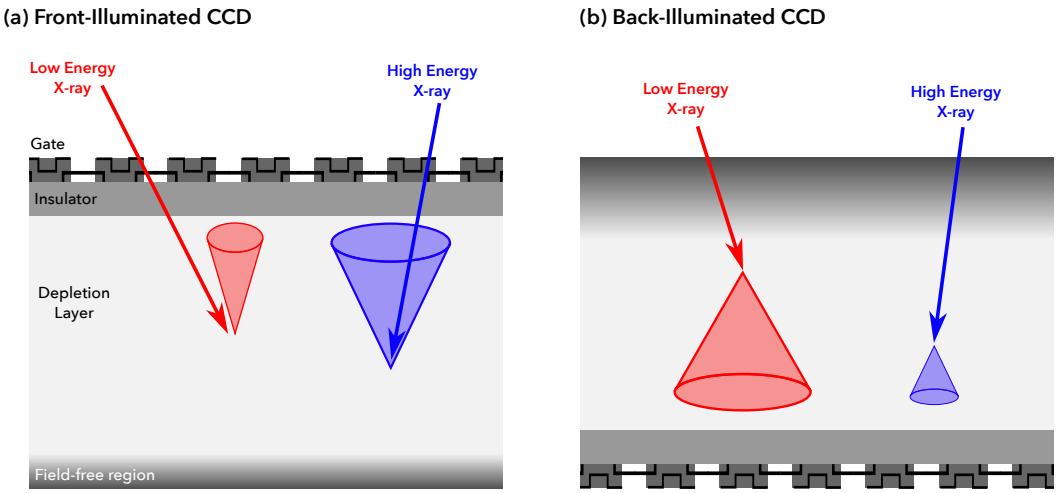

Figure 4.7: Schematic view of the front- (a) and back-illuminated (b) type of the CCD sensors.

The Advanced CCD Imaging Spectrometer (ACIS) can capture high-resolution images and acquire spectra of moderate resolution simultaneously. Figure 4.6 shows the layout of ACIS. ACIS comprises a total of 10 CCD chips: four ACIS-I chips arranged in a 2×2 configuration and six ACIS-S chips set linearly in a 1×6 arrangement. There are two types of chips on ACIS: front-illuminated (FI) and back-illuminated (BI) chips. Figure 4.7 shows a cross-section view of a CCD pixel, which consists of a depletion layer made primarily of silicon, an insulating layer including SiO_2, and electrodes for each pixel (Townsley et al., 2002). We note that the front side is the side on which the electrodes are arranged. While two chips (ACIS-S1 and S3) are back-illuminated (BI)

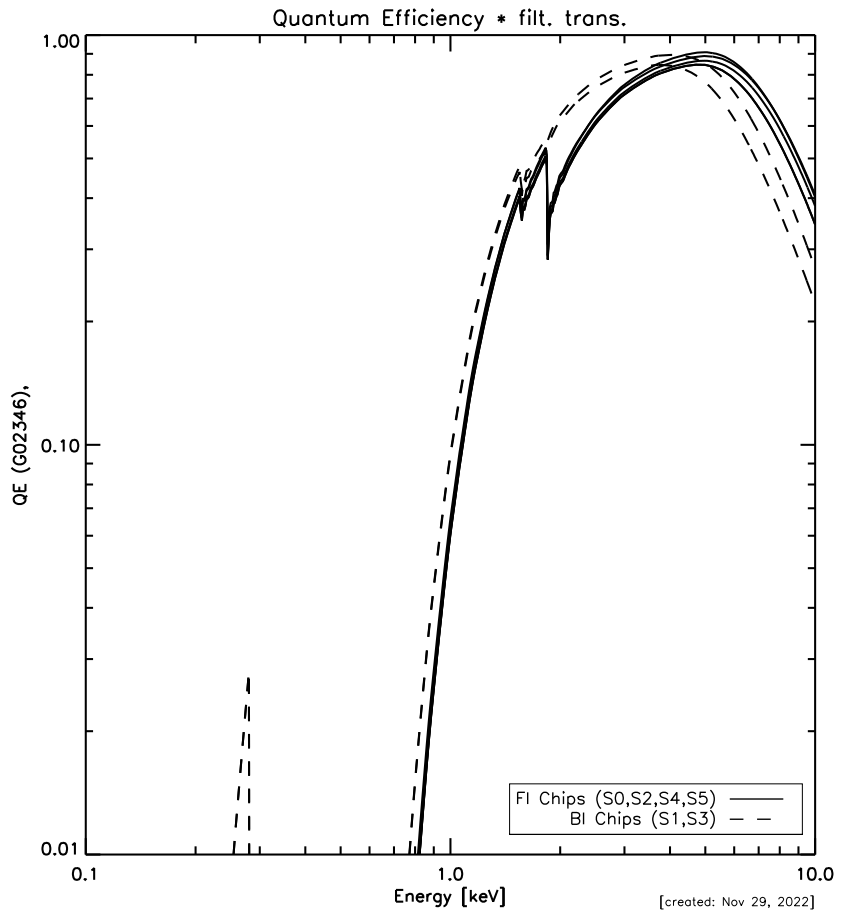

Figure 4.8: The quantum efficiency of ACIS, including the effect of molecular contamination on OBF (Chandra X-ray Center, 2022).

type, the other eight chips are front-illuminated (FI) chips. BI chips of ACIS have higher effective area in the soft band and better energy resolution than FI chips. The low-energy X-rays reaching the FI CCD sensors experience attenuation due to the electrodes at the gate, leading to reduced quantum efficiency, as depicted in Figure 4.3.

4.3.2 Quantum Efficiency

Quantum efficiency (QE) is the proportion of the incident photons that are converted to electrons, generally used to measure a CCD sensitivity. Figure 4.8 shows the QE as a function of the photon energy, considering the effect of molecular contaminations on optical blocking filters (OBFs). Given that the ACIS chips are sensitive not only to X-rays but also to optical/UV light (Lumb et al., 1991), OBFs are positioned between the chips and HRMA to prevent optical light from affecting the CCDs. The filters consist of polyimide placed between two thin aluminum layers. Based on astrophysical data and observations of external calibration sources, it is apparent that the ACIS effective area has degraded since launch due to the molecular contamination from out-gassed material on the cold ACIS OBFs. For calibration of the contamination, Chandra has

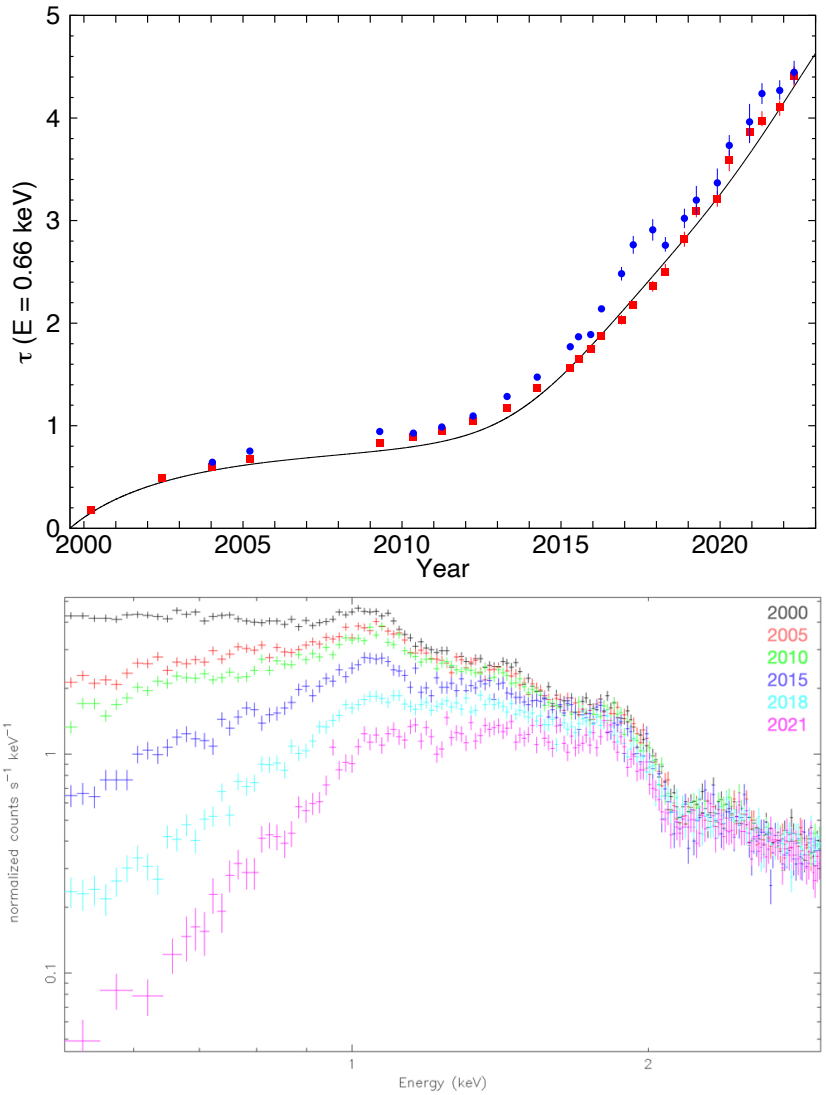

Figure 4.9: (Top): The optical depth at 0.66 keV as a function of the time (year). The blue circles and the red squares show the data of the ACIS-I and ACUS-S, respectively. The data is measured from observations of Abell 1795. (Bottom): The effects of the molecular contamination of the ACIS OBF on the spectra. The spectra are extracted from the ACIS-S data of Abell 1795 taken in 2000 (black), 2005 (red), 2010 (green), 2015 (blue), 2018 (cyan), and 2021 (magenta).

been observing Mkn 421 and PKS 2155−304 (blazars), and RX J1856−3754 (a neutron star) with LETG/ACIS-S and 1E 0102.2−7219 (SNR) with ACIS. Figure 4.9 shows the effect of the ACIS OBF contamination on the effective area. We note that the accumulation of OBF contamination has increased faster since 2014.

4.3.3 Angular Resolution and Field of View

The angular resolution of Chandra is determined by its pixel size of CCDs since HRMA has the high angular resolution as mentioned in Section 4.2. The ACIS chip has an

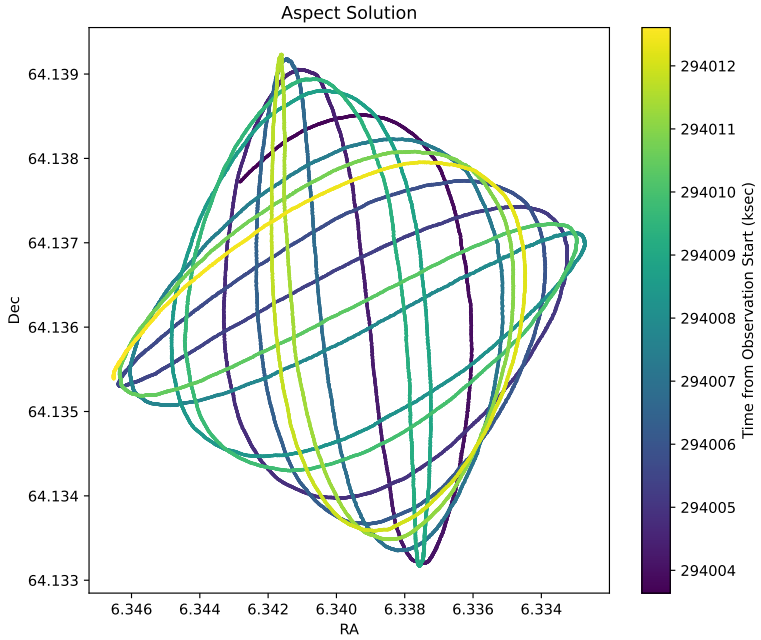

Figure 4.10: The dither pattern of ObsID: 8551. The color corresponds to the time from the start of the observation.

imaging area of 25 mm (~ 8.′3) square consisting 1024×1026 pixels. Thus, the pixel size is 23.985 μm square, which corresponds to 0.4920 ± 0.0001 arcsec squares (Chandra X-ray Center, 2023a). The EEF reaches 90% at 4 pixel and 5 pixel when the X-ray energy is 1.49 keV and 6.4 keV, respectively.

Unless there is a specific request, the spacecraft dithering is performed in a Lissajous pattern (Figure 4.10) during all observations. For ACIS observations, the default dither pattern currently encompasses 32 arcsec peak-to-peak range in both Y and Z directions. There are two major purposes of dithering: (i) to provide some exposure in the area corresponding to the CCD gaps and (ii) to smooth variations in the response in each pixel.

4.3.4 Energy Resolution

The pre-launch energy resolution approached the theoretical limit across most energy levels for the ACIS FI chips. In contrast, the BI chips showed lower performance, as shown in Figure 4.11. However, the resolution has degraded since the launch and the orbital activation due to higher charge transfer inefficiency (CTI), which is the ratio of transferred charges that are trapped and lost. The increased CTI was caused by low-energy protons (also known as soft protons) that reached the focal plane through HRMA by Rutherford scatterings during the radiation belt crossing. Thus, the resolution degrades as the row is far from the readout. A correlation algorithm for the lost energy resolution has been developed. The ACIS energy resolution on board can be monitored

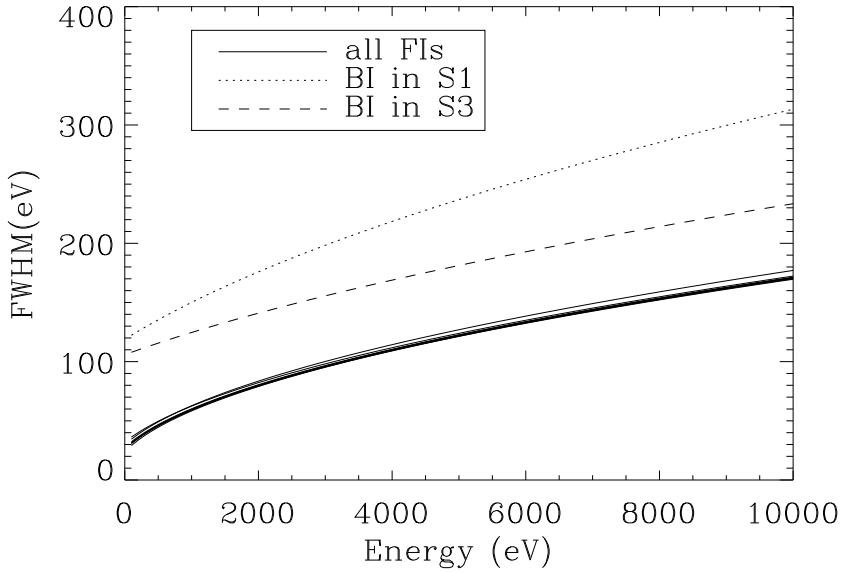

Figure 4.11: The ACIS pre-launch energy resolution versus X-ray energy (Chandra X-ray Center, 2022).

by the external calibration sources, Al Kα (1.49 keV) and Mn Kα (5.9 keV) lines. As can be seen in Figure 4.12, the resolution function of CHIPY improves after the correction.

4.3.5 Background

Chandra X-ray observation on the orbit path is affected by the non-X-ray background (NXB), which originates from external particles (e.g. CRs). In addition to this, ACIS also detects instrumental fluorescence lines generated from collisional excitations of e.g., Al, Au, and Si. These backgrounds affect the analysis in the high energy band ($\gtrsim$ 5 keV), where the photon counting rate from the stellar objects is relatively low. Figure 4.13 shows the NXB spectra taken by ACIS. While the BI chips have a peak around $\sim$ 10 keV originating from the minimum ionizing particles, the FI chips do not have such a structure. This is because the FI chips can partially retrieve NXB using grade filtering. Because NXB events enter ACIS without passing through HRMA, their incident angle is generally large, resulting in a wider NXB distribution on the focal plane. Grade filtering is an imaging analysis technique that classifies events from their distributions. The widths of the depletion layer of the FI and BI chips are 50–75 μm and 45 μm, respectively (Garmire et al., 2003). Thus, the NXB distribution of the BI chips is smaller than that of FI chips, leading to a challenging reduction of NXB by the grade filtering method. On the other hand, the NXB of FI can be reduced well by this method because of the high depth of the depletion layer.

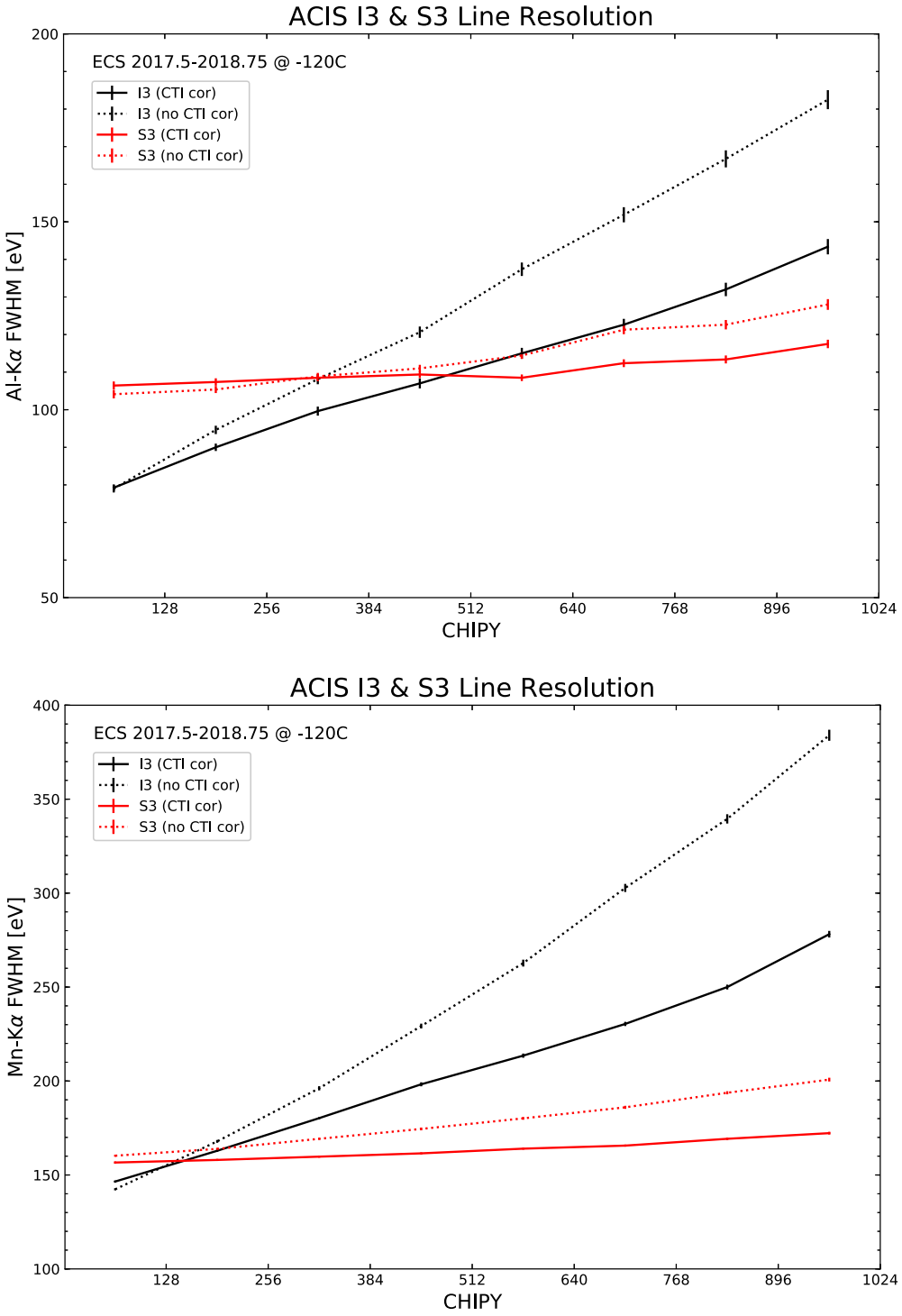

Figure 4.12: ACIS FWHM as a function of the row number (Chandra X-ray Center, 2022). The upper and lower panels are the data measured using the Al Kα and Mn Kα lines, respectively. Black and red correspond to I3 and S3 data, and solid and dotted lines correspond to the corrected and non-corrected data, respectively.

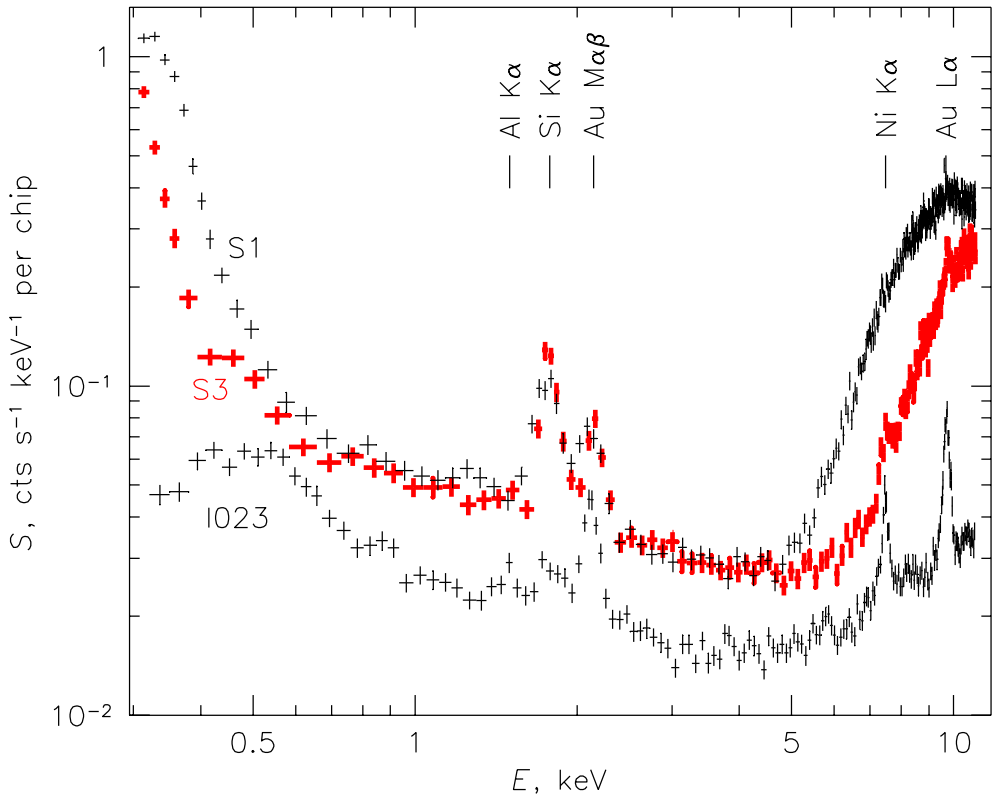

Figure 4.13: Non-X-ray background spectrum of ACIS (Chandra X-ray Center, 2022).

5

Particle Heating and Accleration Observed by X-ray Time Variability

Contents

5.1 Our Objective and Target Selection

Year-scale time variabilities in SNRs can provide information on real-time changes at the shock and post-shock, which is related to a number of unsettled problems, such as cosmic-ray acceleration and electron heating. Aiming to understand particle acceleration and electron-heating mechanisms of shock, we search for time variabilities in nonthermal and thermal X-rays in SNRs. Tycho's SNR (also known as G120.1+1.4) is a nearby and young SNR whose origin is a Type Ia SN in 1572 (e.g., Baade, 1945; Ruiz-Lapuente et al., 2004). Since the apparent diameter of the remnant is $\sim 8'$, we can observe fine structures with the high-resolution imaging of Chandra ($0.''5$ HPD). Therefore, we can expect the detection of time variabilities even on a small physical scale. Throughout this thesis, we assume the distance to be 2.5 kpc based on the work by Zhou et al. (2016) when calculating the actual scales and velocities.

Tycho's SNR is bright in nonthermal and thermal X-ray radiation; the former and latter dominate in the energy band of $\gtrsim$ 4 keV and $\lesssim$ 4 keV, respectively (e.g., Sato

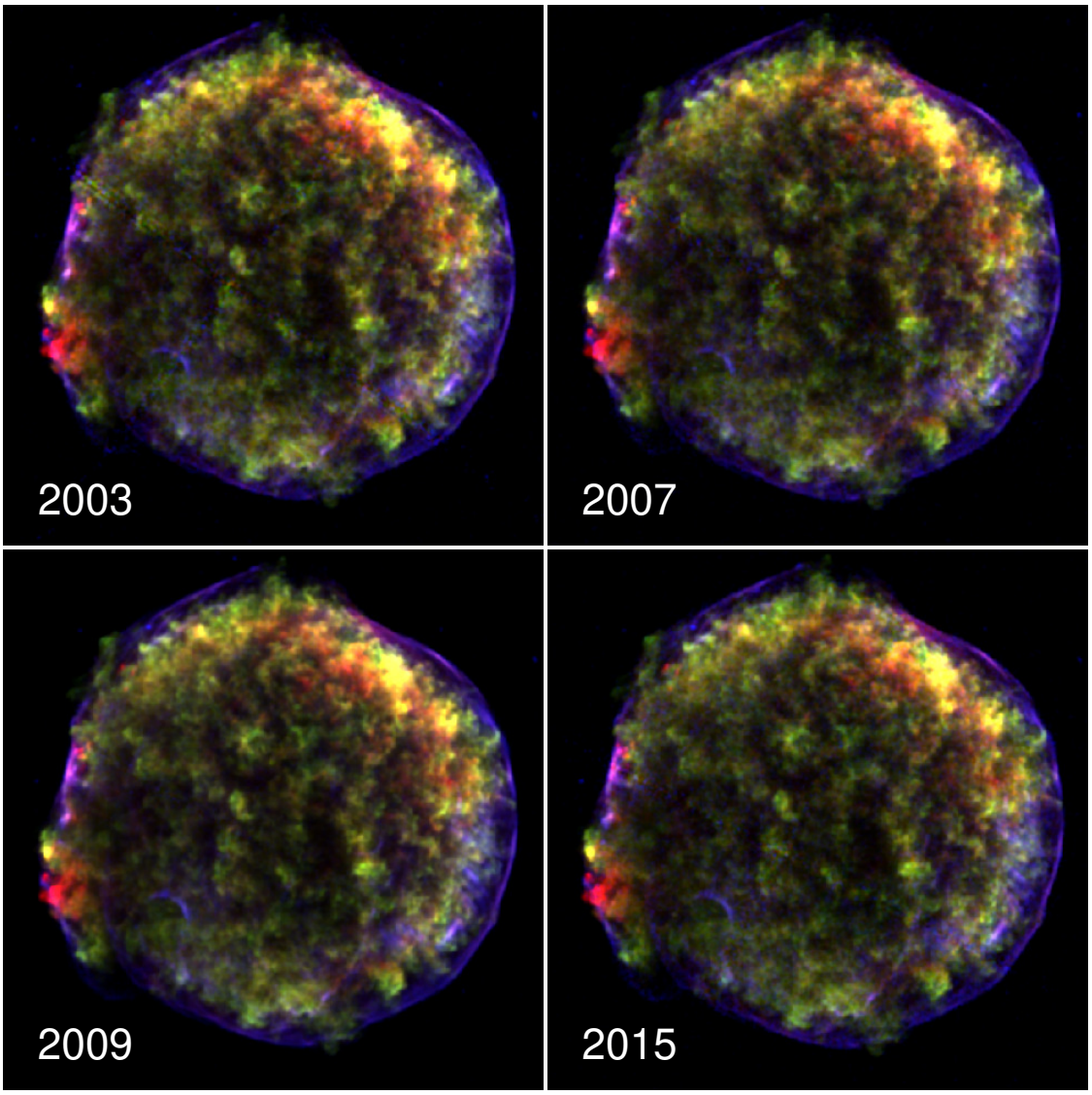

Figure 5.1: RGB image of Tycho's SNR taken by Chandra in 2003, 2007, 2009, and 2015. Red, green, and blue correspond energy bands of 0.7–1.5, 1.7–2.6, and 4.1–6.1 keV.

& Hughes, 2017). Figure 5.1 shows a three-color image. As can be seen in the figure, nonthermal radiation is bright in the outward shell, and thermal radiation is in the inside clump. Each radiation is widely thought to originate from synchrotron radiation and thermalized ejecta (e.g., Hwang et al., 2002).

The nonthermal radiation in the southwestern region has a peculiar structure called "stripe" (Figure 5.2). Eriksen et al. (2011), who discovered this structure, estimated the energies of the accelerated protons in this region to reach PeV, assuming that the gap between the stripes (8″) equals twice its gyroradius. Although some theoretical models were proposed to explain the structure, the origin is still open. Okuno, Matsuda, et al. (2020) reported the year-scale variable features of synchrotron X-rays in the southwestern regions of the remnant, which correspond to the part of stripes. Section 5.3 reports spectral and imaging studies of the whole of the stripe structure. We aim to

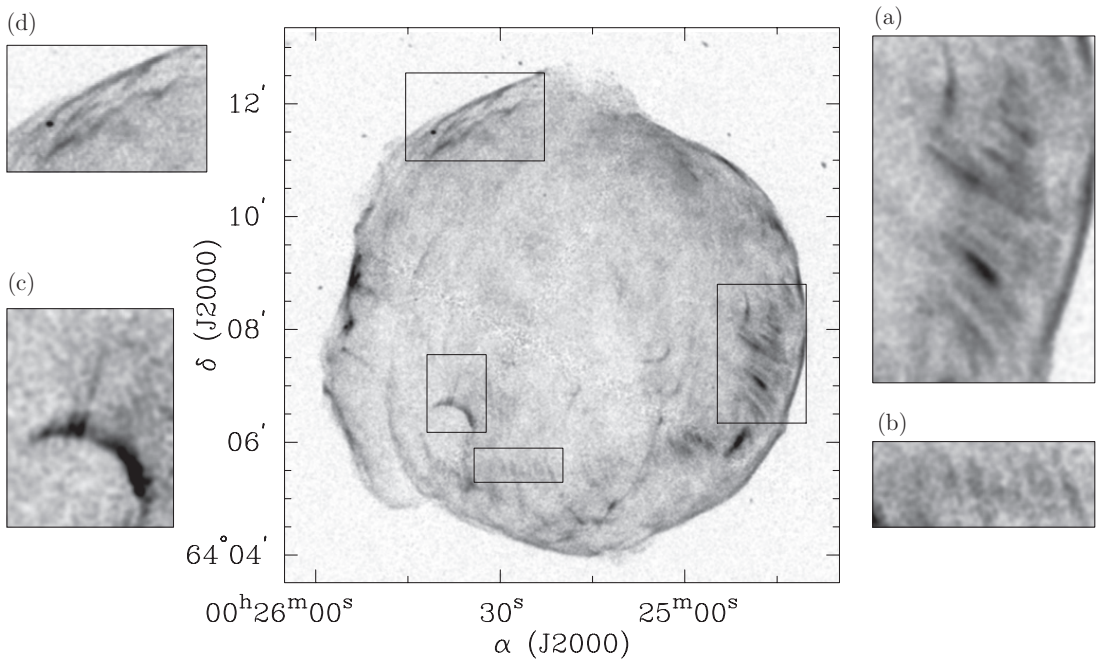

Figure 5.2: Chandra X-ray image in 4.0–6.0 keV band (Eriksen et al., 2011). Zoom-in views on both sides show characteristic structures, including "stripe" features in the panels (a) and (b).

study the temporal and spatial variabilities in synchrotron X-rays from the spectral and imaging analysis, whereas Okuno, Matsuda, et al. (2020) focused on two specific features.

The thermal radiation from the SNR is dominated by shock-heated ejecta (e.g., Hwang et al., 2002), where Yamaguchi et al. (2014) represented the evidence of collisionless electron heating as mentioned in Section 1.2.4. On the other hand, previous studies reported the interaction of forward shock with ISM with other wavelengths, including Hα lines (Ghavamian et al., 2000; J.-J. Lee et al., 2010), infrared light (Ishihara et al., 2010). Moreover, Tanaka et al. (2021) shows the recent shock-cloud collisions from the proper motions of shock waves. These results indicate that the shock wave heated the cloud very recently. Section 5.4 searches for the time variabilities in shock-heated ISM to reveal the evolution of heated plasma.

5.2 Observations and Data Reductions

The Chandra telescope observed Tycho's SNR in 2000, 2003, 2007, 2009, and 2015. The observation log can be seen in Table 5.1. The data in 2000 and in the other years were obtained with ACIS-S and ACIS-I, respectively. The observations in 2007 and 2009 were conducted twice and eight times All of the data is reprocessed with the Chandra Calibration Database (CALDB) version 4.10.7. We note that the observation in 2000 was observed with the back-illuminated chip (ACIS-S3).

We corrected the coordinates of the observed data based on the point source positions to improve the accuracy of imaging analysis. First, the coordinates of significant

Table 5.1: Observation Log

ObsID	Start Date	Effective Exposure (ks)	Chip	Astrometry Correction
115	2000 Oct 01	49	ACIS-S	Corrected
3837	2003 Apr 29	146	ACIS-I	Corrected
7639	2007 Apr 23	109	ACIS-I	Corrected
8551	2007 Apr 26	33	ACIS-I	Not corrected
10093	2009 Apr 13	118	ACIS-I	Corrected
10094	2009 Apr 18	90	ACIS-I	Corrected
10095	2009 Apr 23	173	ACIS-I	—
10096	2009 Apr 27	106	ACIS-I	Corrected
10097	2009 Apr 11	107	ACIS-I	Corrected
10902	2009 Apr 15	40	ACIS-I	Corrected
10903	2009 Apr 17	24	ACIS-I	Not corrected
10904	2009 Apr 13	35	ACIS-I	Not corrected
10906	2009 May 03	41	ACIS-I	Not corrected
15998	2015 Apr 22	147	ACIS-I	Corrected

point sources in the field are determined using the CIAO task `wavdetect` and are aligned based on the source coordinates detected in the dataset with ObsID 10095, whose effective exposure time is the longest, using the task `wcs_match`. All of the event files are reprocessed by the tasks `wcs_update`. Due to the dependence of frame alignment accuracy on photon statistics, short-time observations (ObsID 8551, 10903, 10904, and 10906) are excluded from the group of corrected observations. These observations are used only for spectral analysis.

5.3 Time Variabilities of Non-Thermal X-ray Radiation

5.3.1 Analysis and Results

5.3.1.1 Imaging Analysis

First, we search for notable time variabilities of the stripe structure from a difference map created by subtracting an exposure-corrected image taken in 2003 from one taken in 2015 as shown in Figure 5.3 (a). We select an energy band of 4.1–6.1 keV where the non-thermal emission is thought to be dominant (e.g., Eriksen et al., 2011). Figure 5.3 (b) shows a zoom-in view of the western region. Most stripe features seem to move outward, corresponding to the remnant expansion shown from the proper motion of the outer rim (Warren et al., 2005). However, focusing on the stripes, some flux changes cannot simply be explained by the expansion along the red curves in Figure 5.3 (c), which generally brighten from 2003 to 2015. Note that there are too faint features within the brightened stripes to appear in the exposure-corrected images shown in Figure 5.4. We also detect indications of the proper motion of the faint stripes oriented perpendicular to the shock normal.

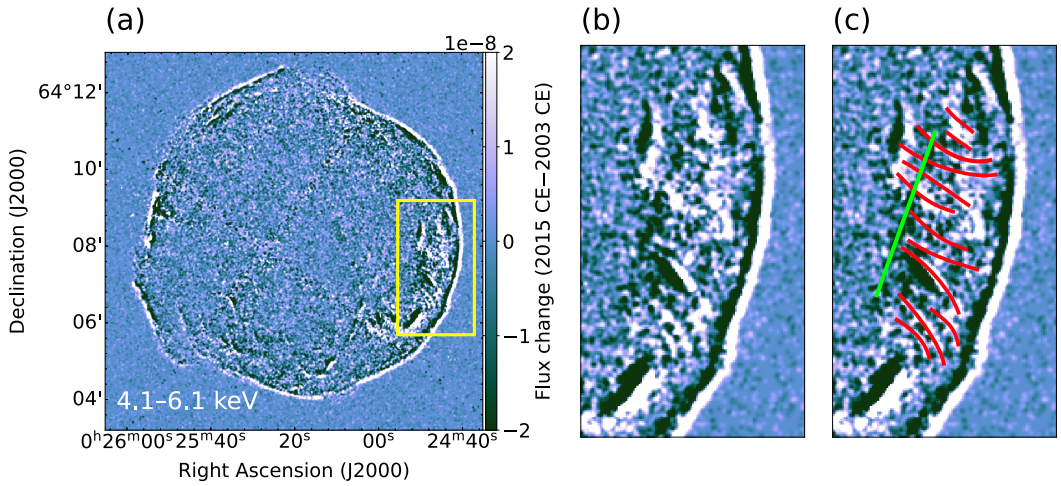

Figure 5.3: (a) Same as Figure 5.10, but in the energy band of 4.1–6.1 keV. The yellow box corresponds to the region delineated in panels (b), (c), and Figure 5.4. (b) Zoom-in view of the yellow box in the panel (a). (c) Similar to panel (b), with superimposed guides aiding in the identification of noteworthy features. The color scale is presented in units of photons s^{-1} cm^{-2}.

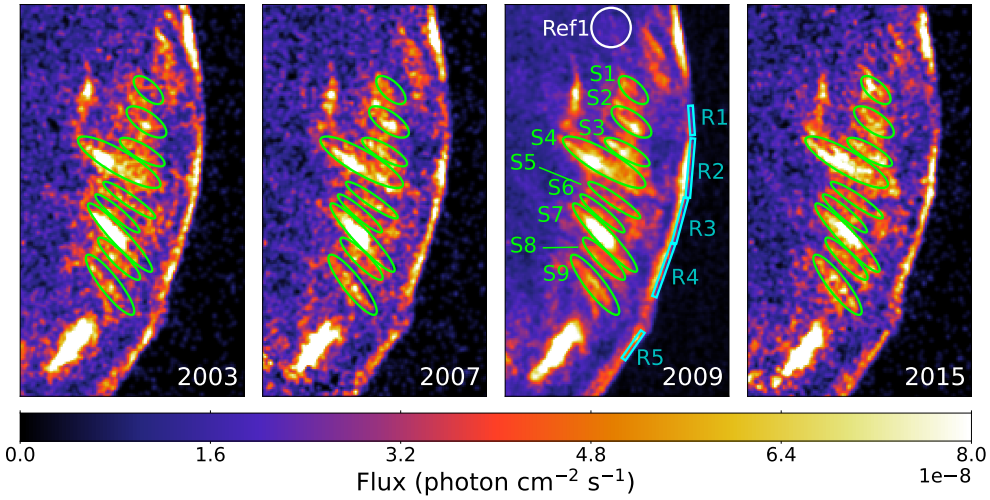

Figure 5.4: Chandra ACIS images of Tycho's SNR taken in 2003, 2007, 2009, and 2015, exposure-corrected and confined to the 4.1–6.1 keV band. The regions denoted as S1–9 (green ellipses) and R1–5 (cyan boxes) are earmarked for spectral analysis. The Ref region (white circle) serves the purpose of the parameter estimation for the thermal component of the stripe emissions.

We extract the 1D profile projected along the azimuthal direction from the rectangular region shown in Figure 5.5, where the brightest stripe (S7 in Figure 5.4) exists. We can detect the sharp and broad peaks corresponding to the rim and stripe. It is clear that both peaks move outward with time, as already indicated by the difference image in Figure 5.10. We measured the proper motion in the same way as (Tanaka et al., 2021) (see Section 6.2 for detailed explanations). A velocity of the rim is obtained as $0.''29 \pm 0.''01$ yr^{-1}, which can be translated into 3400 ± 100 km s^{-1}. This result is consistent with one reported by Williams et al. (2016); the region we analyzed roughly coincides

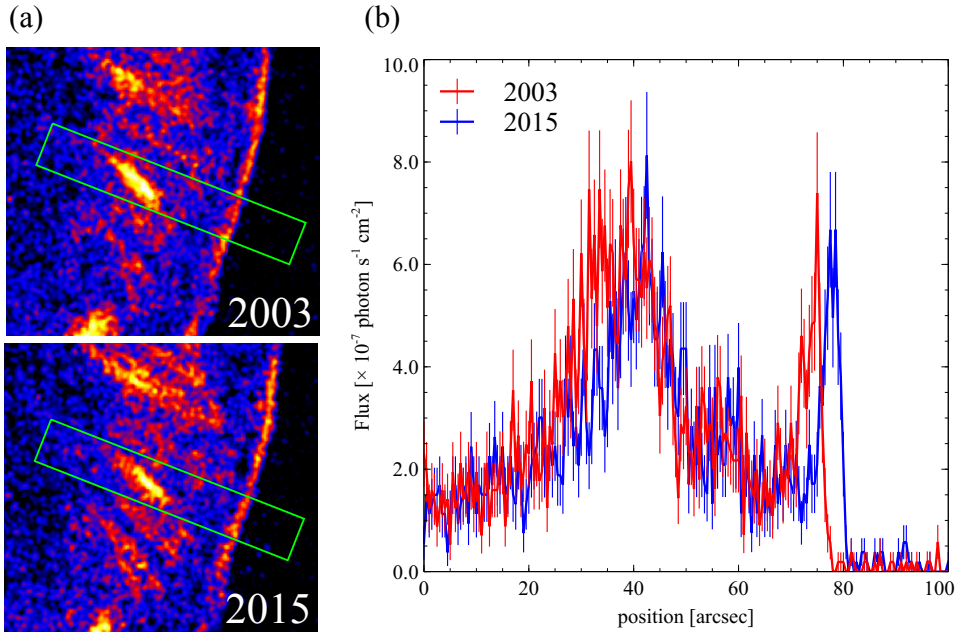

Figure 5.5: (a): The region used for the extraction of the radial profile of the brightest stripe (S7) region. We extracted the profile from the green box region. (b): The profile projected in the green box along the azimuthal direction. The zero point is the inner edge of the box.

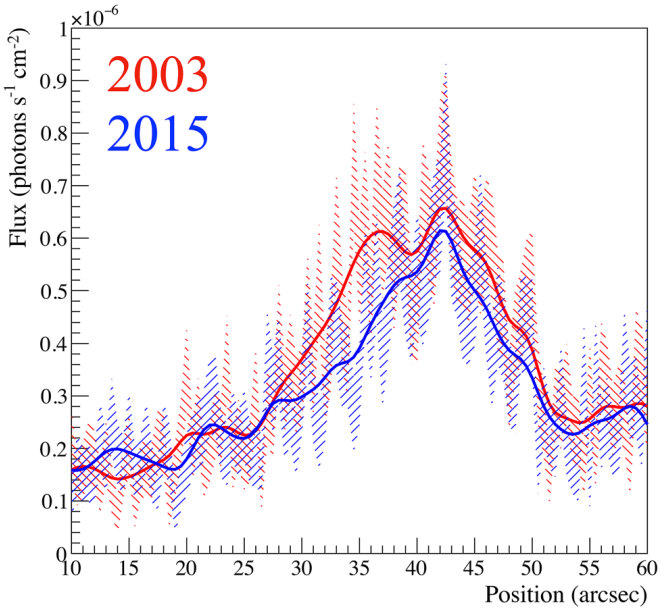

Figure 5.6: Comparison of the 2015 (blue) profile with the 2003 profile shifted by 3.″0 (red). Oblique lines represent the 1σ range. Solid lines depict smoothed profiles.

with their Reg 13. On the other hand, it is difficult to measure the proper motion of the stripe due to its time-variable shape. Examination of the profiles indicates that the peak corresponding to the stripe exhibits a narrower width in 2015 compared to 2003. This phenomenon is more evident in the smoothed profiles presented in Figure 5.6. In this figure, the profile in 2003 is moved by 3.″0, which corresponds to the travel distance of the shock in 12 years. The peak location exhibits rough alignment, indicating that the proper motion of the stripe is comparable to that of the rim.

5.3.1.2 Spectral Analysis

We analyze spectra of each bright stripe extracted from the nine regions labeled as S1–S9 depicted in Figure 5.4. We select a blank region outside of the remnant as a background region. We do not use ObsID 115 because its chip is back-illuminated, which makes the high background in the high-energy band, as mentioned in Chapter 4. We conduct spectral analysis using an X-ray spectral fitting package XSPEC version 12.13.1 (Arnaud, 1996). The spectra are binned so that each bin count is at least ten. The model for this analysis consists of a nonthermal component from synchrotron radiation and a thermal component from the ejecta. A Tüebingen-Boulder model, power law, and two non-equilibrium ionization (NEI) models are employed as the model of the interstellar absorption, synchrotron radiation, and thermal ejecta radiation, respectively.

Within the two components of the ejecta model, one characterizes the emission originating from iron and nickel (Fe component), while the other is dedicated to IMEs, namely magnesium, silicon, sulfur, argon, and calcium (IME component). The abundances of hydrogen, helium, and nitrogen are presumed to be absent since Tycho's SNR is a Type Ia remnant. We fix the abundance of oxygen and neon at the solar composition with respect to carbon, which has the lowest atomic number in the ejecta element. The abundances of other elements are free parameters. We also set the emission measure (EM), which is defined as $\int n_e n_{\rm C} dV/(4\pi d^2 [{\rm C/H}]_\odot)$, as a free parameter. Here, n_e and $n_{\rm C}$ are the number densities of electron and carbon, respectively, and V is the volume of the emitting plasma. The abundances of all elements are allowed to vary freely except for nickel, which is linked to one of iron. We link the emission measure of the Fe component to that of the IME component. The spectral fitting reveals an appearance of residuals at $\sim$ 1.2 keV, which are also seen in spectra of Tycho's SNR (e.g., Sato & Hughes, 2017; Okuno et al., 2020) as well as other SNRs (e.g., Okon et al., 2020). This residual is thought to derive from the uncertainties of the atomic data of Fe XXII relating to the emissivities of Fe L lines (e.g., Gu et al., 2022), so we add a Gaussian to the model for improvement of the fit. We set the centroid energies of all regions as free parameters except for that of the S9 region, which is fixed to 1.23 keV due to the impossibility of the constraint. Eventually, the analysis model is described as:

$$\texttt{Interstellar Abs.} \times [\texttt{NEI(IME)} + \texttt{NEI(Fe)} + \texttt{Gaussian} + \texttt{PowerLaw}]. \tag{5.1}$$

Since the stripe regions have strong nonthermal emission, it is difficult to determine the parameters of the NEI component. Therefore, for a constraint of the parameters,

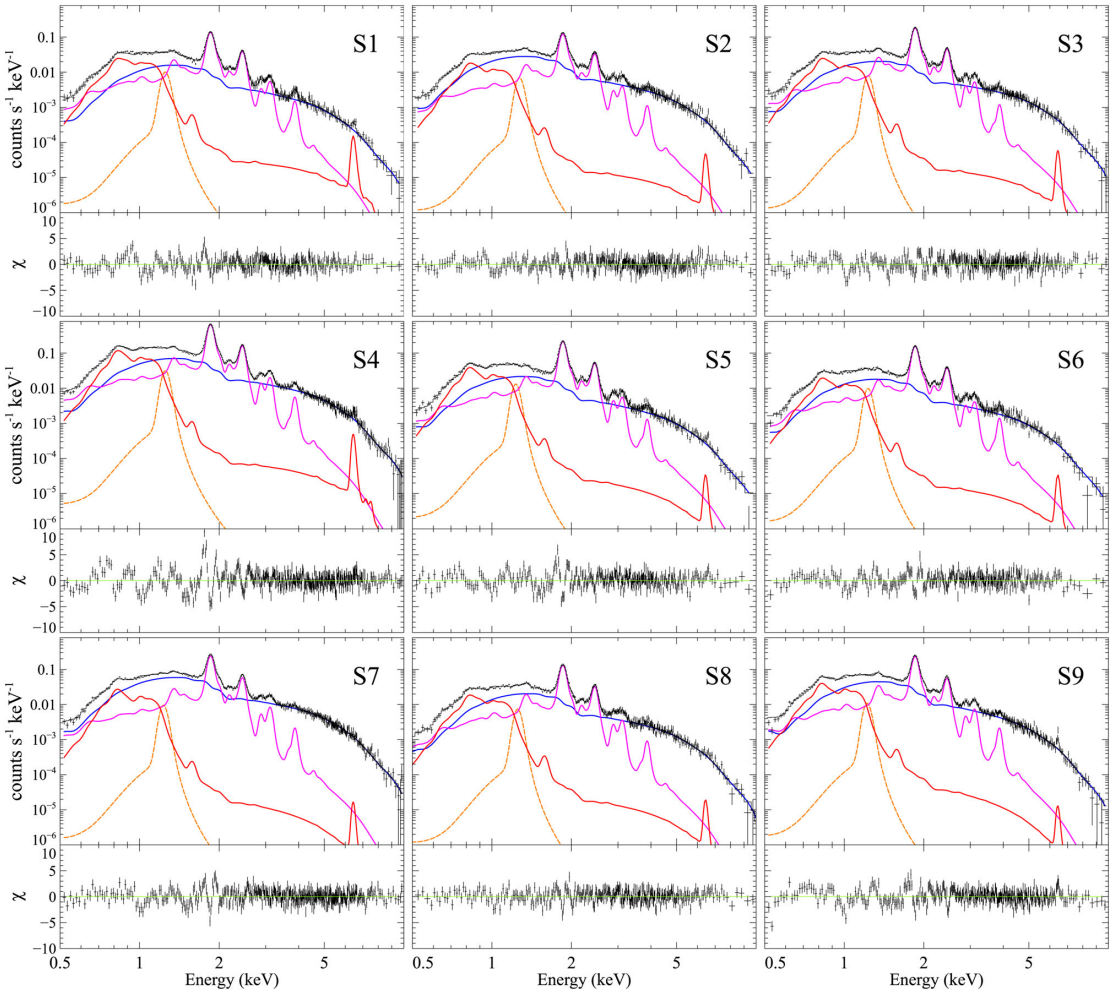

Figure 5.7: Spectra extracted from the stripe regions (S1–9) in 2009. The red and magenta curves show the NEI component of IME and Fe, respectively. The yellow curve is the Gaussian component. The blue curve is the power-law component.

we investigate the NEI component's parameter by analyzing spectra extracted from the region with less contribution from the nonthermal component, which is labeled as "Ref" in Figure 5.4. Since the distance from the remnant center to this region is comparable to that of the stripe, we presume common ionization ages ($n_e t$) between the "Ref" region and the stripes. These ionization ages are determined by fitting the spectrum obtained from the "Ref" region. We obtain the best-fit value of $n_e t$ as 4.52×10^{10} s cm^{-3} and 0.74×10^{10} s cm^{-3} for the IME and Fe components, respectively. When fitting the spectra of the stripe regions, $n_e t$ is fixed to these values.

We first fit spectra obtained from the observations in 2009, whose statistic is the highest as a result of the longest exposure time. Figure 5.7 shows the spectra and their best-fit models, and Table 5.2 lists the best-fit parameters. We then fit the spectra extracted from the observations in 20003, 2007, 2009, and 2015 to see the time variabilities of the stripe emissions. Figure 5.8 depicts the surface brightness of the nonthermal component as a function of the photon index (Γ), revealing a significant stripe-to-stripe

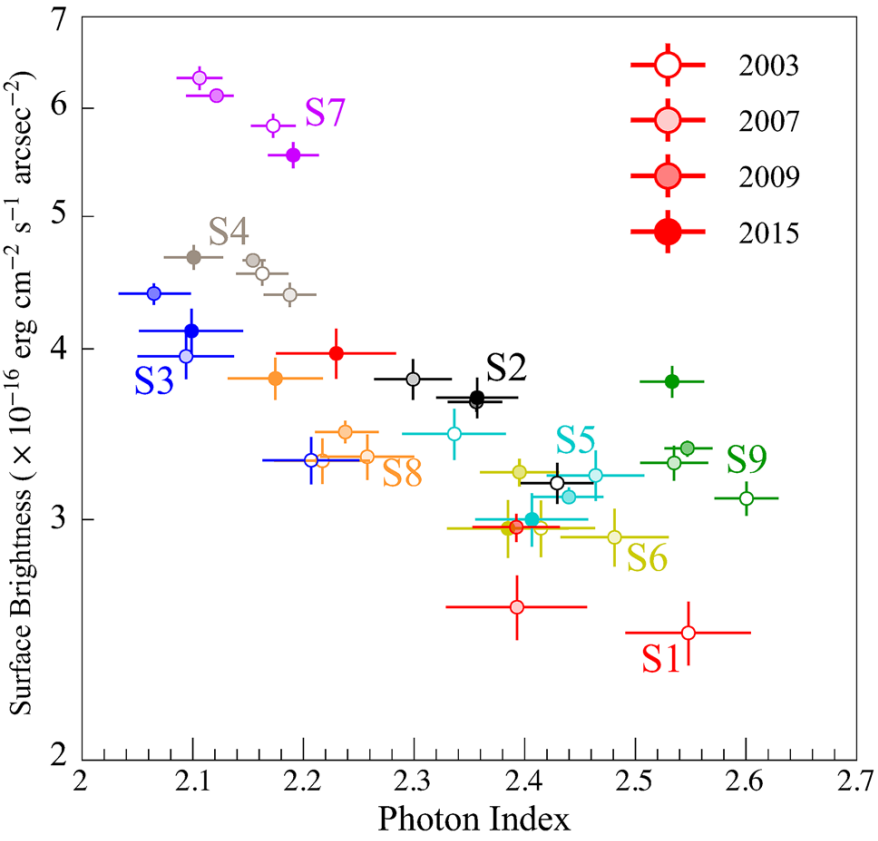

Figure 5.8: The surface brightness of the stripes in each year as a function of the photon index. The color of each label corresponds to individual regions. The brightness of the plots corresponds to the respective epochs of the data.

variation of the parameters as well as time variability of each stripe. An additional noteworthy finding is the robust inverse relationship observed between the surface brightness and the photon indices of the stripe emission.

5.3.2 Discussions

5.3.2.1 Accelerating and Cooling Timescale

Our imaging and spectral analyses have revealed time-variable features in all of the stripes we analyzed. The analyzed stripes have similar variabilities to those which Okuno, Matsuda et al. (2020) reported (corresponding to the S1 region), suggesting the universality of the variabilities in this part of the SNR. Figure 5.8 indeed shows especially significant flux variabilities of the S2, S3, S7, and S9 regions, as well as the S1 region. The fluxes of the S2 and S3 regions in 2003 are lower compared to subsequent years, while the S7 region experienced a flux increase from 2003 to 2007, followed by a subsequent decline. In the case of S9, a consistent flux augmentation is observed from 2003 to 2015. Additionally, the images in Figure 5.3 not only highlight the prominent bright stripes but also reveal that much fainter features exhibit variabilities.

The magnetic field strength of the emitting region can be estimated from the timescale of variabilities as explained in Chapter 3. We can attribute the flux increase to the generation of relativistic electrons through acceleration and the flux decay to the reduction of the electrons through synchrotron cooling. Assuming diffusive shock acceleration, the acceleration timescale can be written as

$$t_{\rm acc} = 4\eta \left(\frac{\varepsilon}{\rm keV}\right)^{0.5} \left(\frac{B}{400\ \mu{\rm G}}\right)^{-1.5} \left(\frac{v_{\rm sh}}{3400\ {\rm km\ s^{-1}}}\right)^{-2} {\rm yr}, \tag{5.2}$$

from Equation (1.37). Here, we assumed the shock velocity as $v_{\rm sh} = 3400$ km s^{-2} according to our measurement in Section 5.3.1.1. Following Equation (2.26), the synchrotron cooling timescale is

$$t_{\rm syn} = 4 \left(\frac{\varepsilon}{\rm keV}\right)^{-0.5} \left(\frac{B}{500\ \mu{\rm G}}\right)^{-1.5} {\rm yr}. \tag{5.3}$$

We here note that the above equations assume the monochromatic emission of synchrotron photons from electrons with a certain energy for simplicity. Given that the observed flux changes are several years, the above equations suggest that the magnetic field in the stripe region is $\sim$ 500 μG.

5.3.2.2 3D location of the stripe structure

Revealing the 3D location of the stripes would provide clues to their physical origin. In the magnetic field strength estimation in Section 5.3.2.1, the stripes are implicitly assumed to be located on the projected blast waves of the SNR. In this scenario, the stripes are expected to apparently move with slower velocities than the expansion, given that only a transverse velocity component is observable. The calculated transverse velocity is 0.″25 yr^{-1}, assuming a spherical shell expansion with a velocity of 0.″29 yr^{-1} (see Section 5.3.1.1). The difference between these two values is too small to be measured using the accessible data since the morphology of the stripe has also been changing with time (Figure 5.6). On the other hand, when we assume that the stripes are located inside the shell or far downstream from the blast waves, the transverse velocity of the stripes should differ from the above case. This scenario should be in favor of the proper motion of some structures perpendicular to the shock normal. Models proposed in previous studies (e.g., Bykov et al., 2011; Malkov et al., 2012; Caprioli & Spitkovsky, 2013; Laming, 2015) assume different locations. A future observation at another epoch would significantly enhance our ability to measure the proper motion of the stripes accurately. This precision is crucial for meaningful comparisons with the proper motion of the blast waves, ultimately aiding in determining the line-of-sight positions of the stripes.

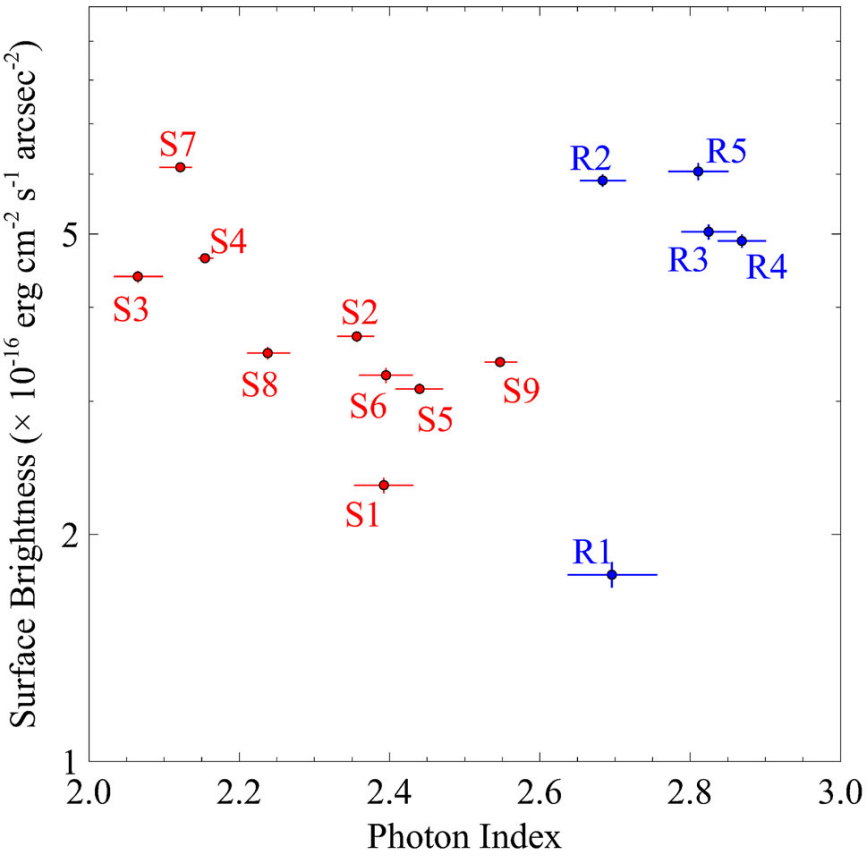

Figure 5.9: Same as Figure 5.8, but the stripe data only from 2009 (red) are shown, and the data extracted from the rim regions (blue) are added for the comparison between the stripe and rim.

5.3.2.3 The origin of the stripe structure

If the synchrotron radiation from the stripe structure has a universal mechanism, the emission from the synchrotron-dominant rim is also expected to exhibit the anti-correlation between surface brightness and photon indices, similar to what was seen in Figure 5.8. To see this, we perform the analysis of the spectra extracted from the R1–5 regions defined in Figure 5.4. Since we can neglect thermal emission in these regions, the spectral fitting is conducted with an absorbed power law. The results are plotted in Figure 5.9, alongside the data from the stripes observed in 2009. In contrast to the stripes, a significant anti-correlation does not appear within the data points from the rim. Our spectroscopy also revealed that the photon indices for the rim emission (Γ = 2.7–2.9) are comparatively softer than those of the stripes (Γ = 2.1–2.6). This aligns with the findings by Lopez et al. (2015), who indicated the emission with the highest roll-off energy using NuSTAR from the west of the remnant coinciding with the location of the stripes.

Then, what contributes to the increased hardness Γ of the spectra in the stripes? One interpretation is that the hardness change reflects the change of the cutoff energy, considering the analyzed energy band corresponds to the cutoff region of a synchrotron spectrum (Lopez et al., 2015). In this case, the harder the synchrotron radiation becomes,

the higher it means the cutoff energy is. We begin by considering the scenario in which the stripes share the same origin as the blast waves, although the discrepancy in spectra between the stripes and the blast waves (Figure 5.9) implies a lower likelihood of this hypothesis. Given the NuSTAR result by Lopez et al. (2015), the energy of synchrotron-emitting electrons is limited by the accelerated time corresponding to the age of the remnant (the age-limited case in the Section 2.2.3). The cutoff energy $\varepsilon_{\rm max}$ thus depends both on the magnetic field strength and on the shock velocity ($\varepsilon_{\rm max} \propto {v_{\rm sh}}^4 B^3$) as described in Equation (2.30). Therefore, the hard spectra observed in the stripes can be explained by the high shock velocity and/or the intense magnetic field within the region. Considering the unique morphology of the stripes, it is improbable that the increased hardness can be solely attributed to the high shock velocity. A more likely scenario is the enhancement of the magnetic field in the stripes, possibly through mechanisms such as the resonant (Skilling, 1975) or non-resonant (Bell, 2004) cosmic-ray streaming instability. In this scenario, explaining the observed variability on a yearly timescale is challenging, as the acceleration time scale is comparable to the age ($\sim$ 450 years). One possible explanation compatible with both the result by Lopez et al. (2015) and the fluctuating emissions in the stripes is the local amplification of the magnetic field at the stripe region: the acceleration time in most regions is limited by the remnant age, while that at the stripe region is limited by synchrotron cooling loss as the result of enhanced magnetic field. Since the analyzed energy range in this study is very limited, we can allow for various possibilities to be considered. We would constrain the origin of the hardening by future missions with both the wide energy range and high angular resolution, such as HEX-P (Madsen et al., 2019) and Lynx (Gaskin et al., 2018). Observation with Chandra indeed discovered such softening in Tycho's SNR by Cassam-Chenaï et al. (2007).

When we assume that the stripe location is far downstream of the shock, it is somewhat puzzling to understand the hardness of the spectra. In order to deliver the synchrotron-emitting electrons to the stripe region, the electrons need to be transported downstream through diffusion or advection after acceleration at the blast waves. The transported ultra-relativistic electrons undergo substantial synchrotron cooling losses, leading to a softening of the electron spectrum and, consequently, the synchrotron X-ray spectrum. A possible mechanism causing the hardening involves an enhanced magnetic field. As Equation (2.23) describes, the synchrotron photon energy ε depends on the parent electron energy E_e. It follows that the stronger magnetic field leads to the higher synchrotron cutoff energy, resulting in the observation of the harder synchrotron spectra with Chandra. Moreover, the presence of compressible waves/turbulence within the stripes might cause stochastic acceleration, resulting in a harder electron spectrum, as theoretically studied by Zhang (2015) and Wilhelm et al. (2020). Three-dimensional magnetohydrodynamic simulations by Inoue et al. (2012) suggested the possibility of magnetic field amplification downstream shock due to interactions between shock and clumps in ISM.

In either scenario discussed above, explanations of the anti-correlation shown in Figure 5.8 would pose a challenge. The findings suggest that only a few parameters are related to the observed temporal and spatial variation; otherwise, such a pronounced anti-correlation would not be observed. It is noteworthy that the surface brightness

is equivalent in each region. This equivalence implies that the line-of-sight depth is comparable between each stripe, assuming similar magnetic field strength and relativistic electron densities across the stripes. If this holds true, it is more plausible to consider the shape of the stripes as spheroids rather than thin sheets.

Table 5.2: Best-fit parameters of the stripe regions in 2009

Parameters (unit)	S1	S2	S3	S4	S5	S6	S7	S8	S9
Solid angle (arcsec^2)	143.8	210.2	172.7	505.3	161.7	141.1	338.8	183.4	311.6
Absorption									
$N_{\rm H}$ (10^{21} cm^{-2})	6.80 ± 0.17	$6.37^{+0.26}_{-0.10}$	$5.23^{+0.21}_{-0.12}$	$5.83^{+0.05}_{-0.06}$	$5.92^{+0.24}_{-0.20}$	$6.32^{+0.30}_{-0.19}$	$6.03^{+0.17}_{-0.12}$	$6.56^{+0.20}_{-0.28}$	$5.26^{+0.14}_{-0.12}$
Power law									
Γ	2.39 ± 0.04	$2.37^{+0.04}_{-0.03}$	2.06 ± 0.03	2.15 ± 0.01	2.44 ± 0.03	2.40 ± 0.04	$2.12^{+0.02}_{-0.03}$	$2.25^{+0.02}_{-0.03}$	2.55 ± 0.02
Flux (10^{-13} erg s^{-1} cm^{-2})	0.43 ± 0.01	0.77 ± 0.01	0.76 ± 0.01	2.35 ± 0.02	0.50 ± 0.01	0.46 ± 0.01	$2.08^{+0.02}_{-0.01}$	0.64 ± 0.01	$1.05^{+0.01}_{-0.02}$
IME component									
EM* (10^9 cm^{-5})	$3.31^{+0.42}_{-0.38}$	$1.48^{+0.41}_{-0.43}$	$1.71^{+0.24}_{-0.36}$	$4.97^{+0.86}_{-0.26}$	$2.11^{+0.70}_{-0.40}$	$1.51^{+0.54}_{-0.38}$	$1.50^{+0.49}_{-0.61}$	$2.22^{+0.50}_{-0.42}$	$0.35^{+0.06}_{-0.04}$
kT_e (keV)	$1.49^{+0.04}_{-0.03}$	$1.65^{+0.03}_{-0.05}$	$1.68^{+0.01}_{-0.04}$	1.55 ± 0.01	$1.58^{+0.03}_{-0.02}$	$1.57^{+0.04}_{-0.03}$	$1.71^{+0.03}_{-0.04}$	$1.45^{+0.01}_{-0.04}$	1.41 ± 0.03
$n_e t$ (10^{10} s cm^{-3})					4.53 (fixed)				
[Mg/C]/[Mg/C]$_\odot$	$4.8^{+0.6}_{-0.4}$	7.2 ± 1.4	$9.2^{+1.9}_{-0.8}$	$8.1^{+0.4}_{-0.7}$	$5.2^{+0.3}_{-1.3}$	$6.4^{+1.7}_{-1.6}$	$10.6^{+6.9}_{-2.1}$	$5.5^{+0.8}_{-0.9}$	4.8 ± 0.6
[Si/C]/[Si/C]$_\odot$	84^{+10}_{-9}	161^{+68}_{-35}	190^{+40}_{-27}	238^{+23}_{-22}	183^{+41}_{-37}	189^{+38}_{-46}	279^{+194}_{-69}	112^{+33}_{-20}	73^{+10}_{-9}
[S/C]/[S/C]$_\odot$	77^{+10}_{-8}	130^{+67}_{-28}	143^{+31}_{-19}	185^{+11}_{-20}	134^{+30}_{-28}	139^{+39}_{-36}	194^{+144}_{-48}	91^{+25}_{-16}	81 ± 11
[Ar/C]/[Ar/C]$_\odot$	85^{+14}_{-11}	105^{+40}_{-12}	110^{+13}_{-10}	175^{+8}_{-11}	99^{+24}_{-9}	106^{+31}_{-22}	202^{+140}_{-65}	77 ± 9	86^{+14}_{-13}
[Ca/C]/[Ca/C]$_\odot$	156^{+28}_{-25}	202^{+72}_{-26}	158^{+55}_{-25}	163^{+20}_{-29}	159^{+24}_{-23}	258^{+86}_{-77}	298^{+93}_{-77}	142 ± 24	168^{+33}_{-30}
Fe component									
EM* (10^9 cm^{-5})	3.31	1.48	1.77	4.97	2.11	1.51	1.50	2.22	0.37
kT_e (keV)	$5.54^{+0.91}_{-0.83}$	$4.30^{+1.30}_{-0.98}$	$3.85^{+1.20}_{-0.80}$	$4.63^{+0.40}_{-0.26}$	$2.36^{+0.35}_{-0.39}$	$3.00^{+1.84}_{-0.83}$	$2.04^{+0.62}_{-0.26}$	$2.41^{+0.26}_{-0.55}$	$1.53^{+0.12}_{-0.23}$
$n_e t$ (10^{10} s cm^{-3})					0.74 (fixed)				
[Fe/C]/[Fe/C]$_\odot$	$3.6^{+0.5}_{-0.4}$	$5.4^{+1.9}_{-1.2}$	$5.4^{+1.4}_{-0.5}$	$9.2^{+0.8}_{-1.0}$	$7.6^{+1.4}_{-1.1}$	5.5 ± 1.2	$8.0^{+3.2}_{-1.5}$	$3.8^{+0.8}_{-0.5}$	$4.8^{+0.6}_{-0.5}$
Gaussian									
Norm. (10^{-5} s^{-1} cm^{-2})	0.53 ± 0.05	0.33 ± 0.05	0.36 ± 0.04	$1.40^{+0.08}_{-0.07}$	0.60 ± 0.05	0.47 ± 0.05	$0.44^{+0.06}_{-0.07}$	$0.35^{+0.04}_{-0.05}$	$0.61^{+0.08}_{-0.07}$
Centroid (keV)	$1.25^{+0.02}_{-0.01}$	$1.28^{+0.05}_{-0.02}$	1.24 ± 0.01	$1.253^{+0.006}_{-0.001}$	$1.238^{+0.002}_{-0.007}$	1.234 ± 0.003	$1.232^{+0.022}_{-0.002}$	$1.254^{+0.007}_{-0.005}$	1.23 (fixed)
χ^2 (d.o.f.)	405 (291)	375 (331)	463 (338)	1153 (433)	593 (302)	451 (299)	598 (418)	392 (321)	606 (373)

* Emmission measures of Fe and IME component are defined by $\int n_{\rm e} n_{\rm C} dV / 4\pi d^2 \cdot [{\rm C/H}]_\odot$ and linked to each other.

† The parameter of [Fe/C]/[Fe/C]$_\odot$ is linked to one of [Ni/C]/[Ni/C]$_\odot$.

5.4 Time Variabilities of Thermal X-ray Radiation

5.4.1 Analysis and Results

5.4.1.1 Imaging Analysis

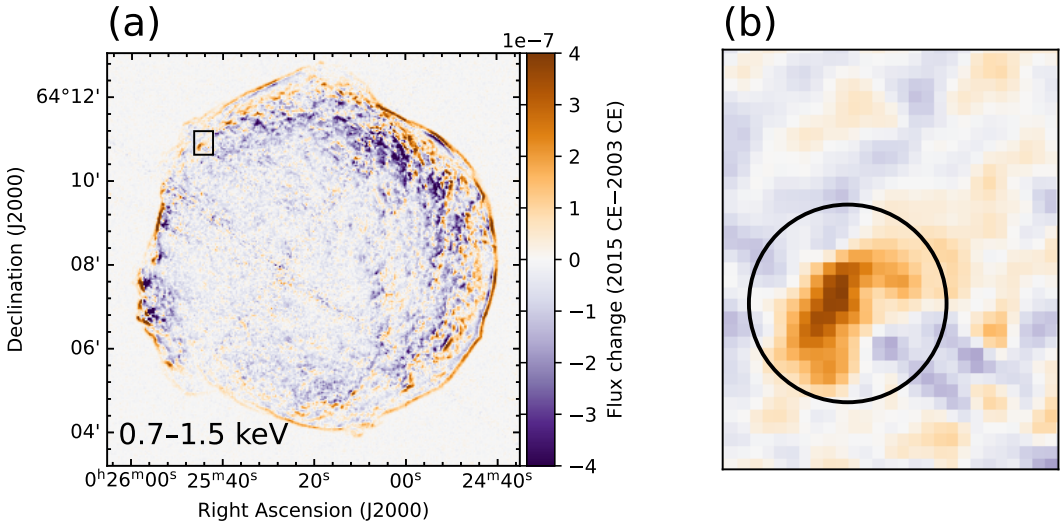

Figure 5.10: (a): A difference image of Tycho's SNR between 2003 and 2015 within the energy band of 0.7–1.5 keV. The color bar means the flux changes over the years in units of photons s^{-1} cm^{-2}. Positive values represent brightening, and negative values represent darkening. The box corresponds to the region delineated in panels (b) and Figure 5.11. (b): Zoom-in view of the box in the panel (a). The noteworthy feature is superimposed by a circle for aiding in the identification.

Figure 5.10 (a) shows a difference image made in the same way as Figure 5.3 but in the energy band of 0.7–1.5 keV, where the thermal radiation is dominant (e.g., Warren et al., 2005; Sato & Hughes, 2017). The thermal emission can be seen in the interior of the shell, while the nonthermal emission is dominant in the shell. In the difference maps, we can observe adjacent increases and decreases in most features. This phenomenon arises from the movement of bright structures between 2003 and 2015 due to the expansion of ejecta and the radial proper motion of the blast waves. In the northwest, however, there is a bright spot (hereafter, Knot1) where we discover a monotonical increase of photon counts over time without signs of proper motion as can be seen in the enlarged image of Figure 5.10 (b).

We present visual comparisons of Knot1 flux images in the energy bands of 0.7–1.5 keV (soft band), 1.6–2.5 keV (middle band), and 4.1–6.1 keV (hard band) in Figure 5.11. We note that thermal radiation predominantly contributes to the soft and middle bands, while nonthermal radiation dominates in the hard band (e.g., Warren et al., 2005). The gradual brightening of Knot1 is evident in the soft band images from 2000 through 2015 (Figure 5.11 a), consistent with the suggestion in Figure 5.10. In contrast, the

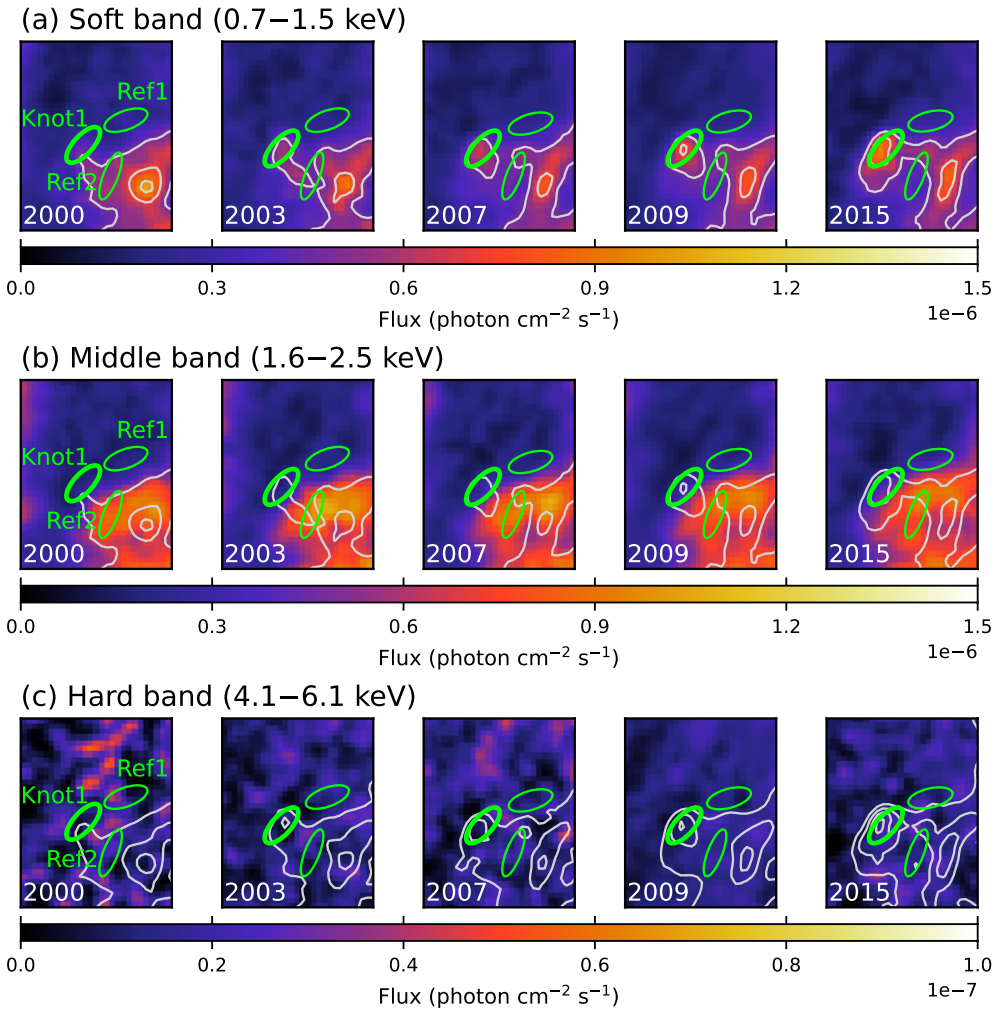

Figure 5.11: Exposure-corrected X-ray images of Knot1 in the soft (a), middle (b), and hard (c) bands taken in 2000, 2003, 2007, 2009, and 2015. The flux of the soft-band X-rays is shown with white contours. The Knot1, Ref1, and Ref2 regions used for spectral extraction are shown by green ellipses.

middle-band images (Figure 5.11 b) show no significant flux fluctuation, except for the ejecta expansion. Moreover, there is no correlation with the Knot1 structure in the soft-band images. These findings suggest that Knot1 originates differently from the middle-band X-rays. The hard-band images in Figure 5.11 (c) reveal relatively faint and stable synchrotron emission in Knot1, in contrast to the pronounced flux changes observed in the stripe regions in the southwest (Section 5.3; Okuno et al., 2020; Matsuda et al., 2020).

5.4.1.2 Spectral Analysis

For investigation of the nature of Knot1 and quantitative measurement of its time variabilities, we conducted the spectral analysis of the radiation from the region shown in Figure 5.11. We merged the datasets obtained in each year; thus, five spectra are obtained from five different epochs (2000, 2003, 2007, 2009, and 2015). The background

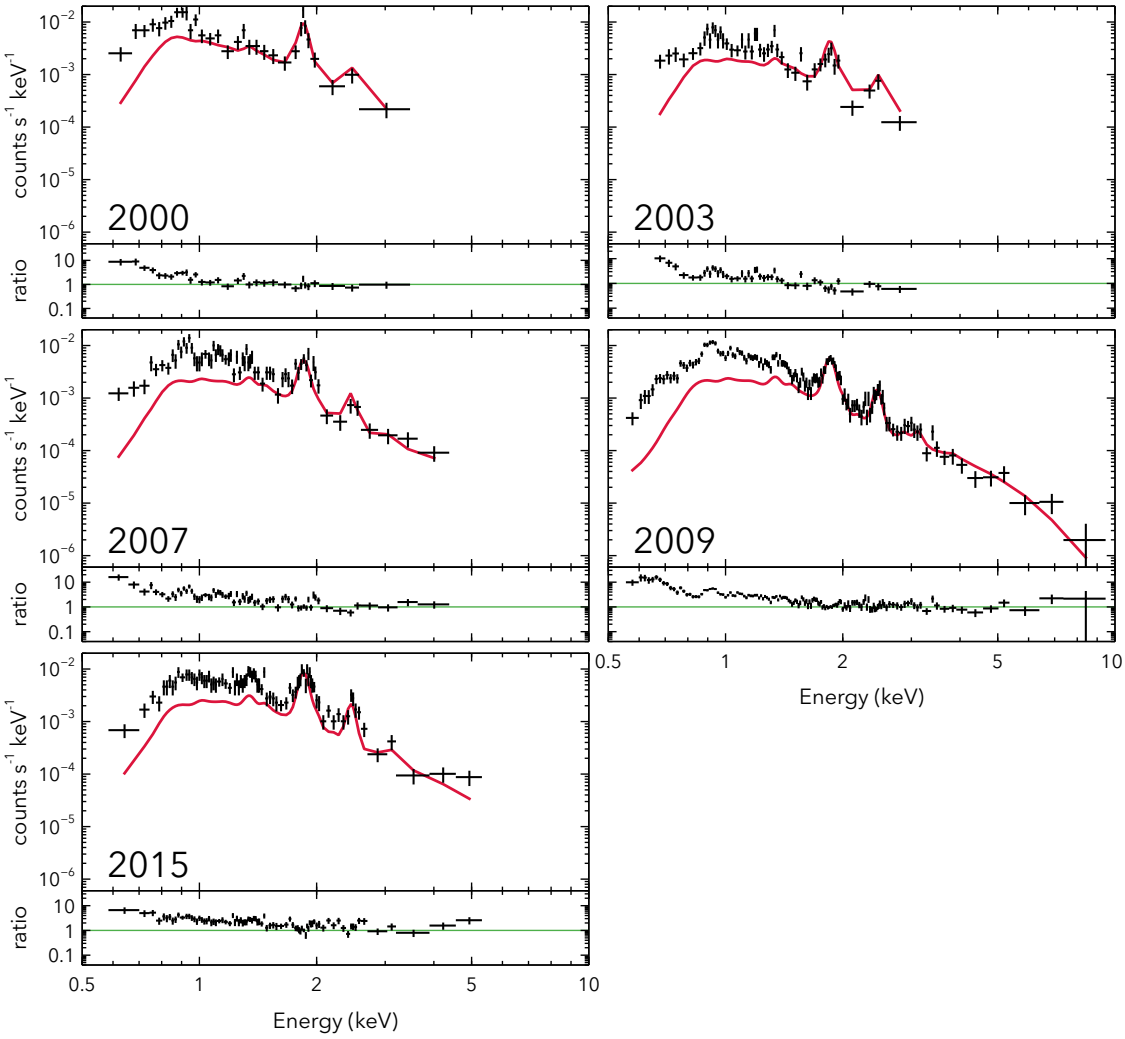

Figure 5.12: Comparison between the spectra of the Knot1 region (black) and the best-fit model of the Refl region (red). We apply the response of Knot1 to the Refl model. The bottom panel in the box of each year represents the ratio calculated by dividing the Knot1 counts by the Refl counts.

region is the same as that used in Section 5.3. The Knot1 region apparently has the contribution of X-rays unrelated to the brightening structure in the middle band, as can be seen in Figure 5.11 (b). In order to estimate that contribution, reference spectra are extracted from a nearby region (noted as "Refl" in Figure 5.11), whose middle-band flux is almost the same as Knot1.

Figure 5.12 shows comparisons between the Knot1 spectra and the best-fit model of Refl in each year. It becomes evident that the Knot1 emission in the $\lesssim$ 1.5 keV band is notably more intense than that of Refl, whereas this distinction is not observed in the higher energy band. A plausible interpretation is that the thermal radiation in Refl has the same origin as the southeastward diffusing ejecta since the thermal radiation in most regions inside is generally dominated by the ejecta emission (e.g., Cassam-Chenaï et al., 2007; Miceli et al., 2015). It can also be confirmed by its spectrum, which can be replicated

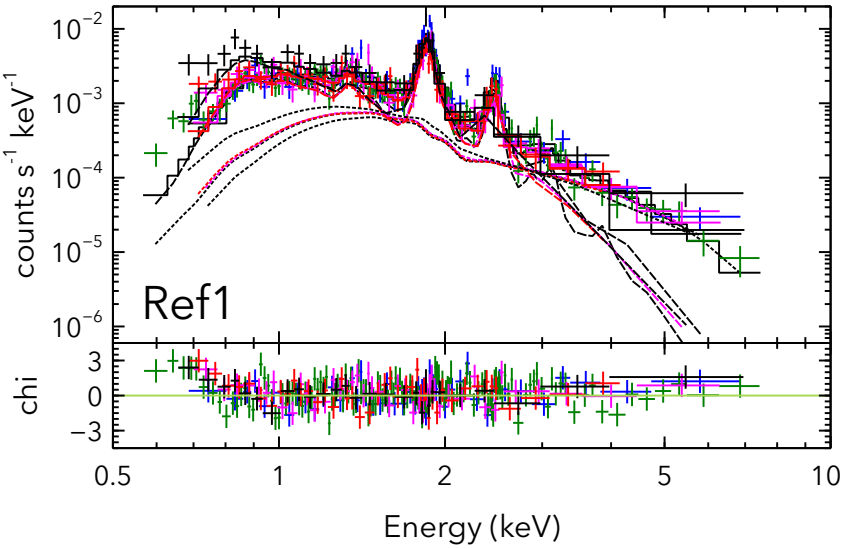

Figure 5.13: Spectra extracted from the Ref1 regions taken in 2000 (black), 2003 (red), 2007 (magenta), 2009 (green), and 2015 (blue). The dashed and dotted curves represent components of the NEI model originating from ejecta and power law, respectively.

using an NEI model with pure-metal composition. Meanwhile, the excess emission can be interpreted as the radiation emitted from the brightening structure. Figure 5.12 also suggests the energy range characterized by a high Knot1/Ref1 ratio is broadened toward higher energies year-by-year. It provides further support for the flux increase of the soft-band radiation from Knot1. For a more quantitative assessment of the temporal variability of the excess in the soft band, we conducted spectral fitting for Knot1 using the model of a soft NEI component added to the model used for the Ref1 region.

We perform simultaneous fitting for the Knot1 and Ref1 spectra taken in 2000, 2003, 2007, 2009, and 2015. This analysis uses XSPEC version 12.13.1 (Arnaud, 1996) with AtomDB version 3.0.9 (Foster et al., 2017). We bin the spectra so that each bin has at least ten counts and fit it over the 0.5–10 keV energy. The model of the Ref1 spectrum is composed of an absorbed metal-rich NEI and a power law, in accordance with previous studies (e.g., Yamaguchi et al., 2017) and expressed as:

$$\texttt{Interstellar Abs.} \times (\texttt{NEI} + \texttt{PowerLaw}). \tag{5.4}$$

The metal-rich NEI component represents the radiation from the ejecta. We assume electron temperature (kT_e), ionization timescale ($n_e t$), and abundances of the component to be shared for each year. The abundances of magnesium, silicon, sulfur, argon, and iron are set as free parameters, while those of calcium and nickel are linked to argon and iron, respectively. The settings for the abundance of other light elements are as same as those of the NEI model in Section 5.3. We also allow to vary EM freely. We fix the photon index (Γ) of the power-law component to 2.79, which is obtained by the spectral analysis of a nearby nonthermal-dominated region. The power-law flux is linked each year. These components are multiplied by the Tübingen-Boulder model (Wilms et al.,

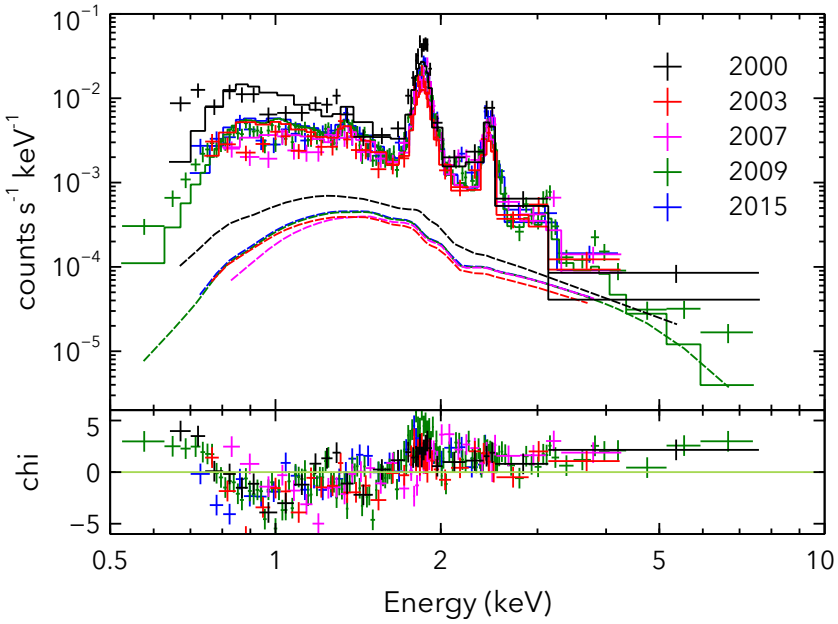

Figure 5.14: Spectra extracted from the Ref2 region. Each component represents the same one of Figure 5.13. The parameters, except for the normalizations, are the same as the best-fit parameters of the Ref1 region. The normalizations of ejecta and power law components are free parameters.

2000), which represents interstellar absorption. Figure 5.13 and Table 5.3 show fitting results and best-fit parameters of the Ref1 region, respectively.

The Knot1 spectra are fitted with a model consisting of the ejecta component, which is also employed for the Ref1 region, and an additional soft component. So the model for the Knot1 region can be expressed as:

$$\texttt{Interstellar Abs.} \times (\texttt{NEI(Soft)} + \texttt{NEI(ejecta)} + \texttt{PowerLaw}). \tag{5.5}$$

We fixed each elemental abundance to the solar value. We allow kT_e, n_et, and EMs to vary freely over years except for n_et in 2000. Only n_et in 2000 is fixed to that in 2003 minus 4×10^9 cm^{-3} s (= 42 cm^{-3} $\times$ 3 yr) since it cannot be determined due to a lack of statistics. Note that the other parameters did not vary beyond the 1σ confidence level as the result of fixing n_et. We linked the parameters of the ejecta component to the Ref1 spectra, but the EMs are free parameters.

The uncertainty in n_et for the year 2000 could potentially arise from X-ray contamination originating from the southwestern ejecta. Consequently, we explore the prospect of southwestern emission extension by examining the spectrum of an inner region of Knot1 directed towards the southwest (designated as the Ref2 region in Figure 5.11). In Figure 5.14, we present the Ref2 spectra along with models whose parameters, excluding EM, are fixed to those of Ref1. As depicted in the figure, the Ref2 spectra lack the soft-band excess observed in Knot1. This outcome indicates that the southwest extension is negligible and that the soft thermal emission is exclusively attributed to Knot1.

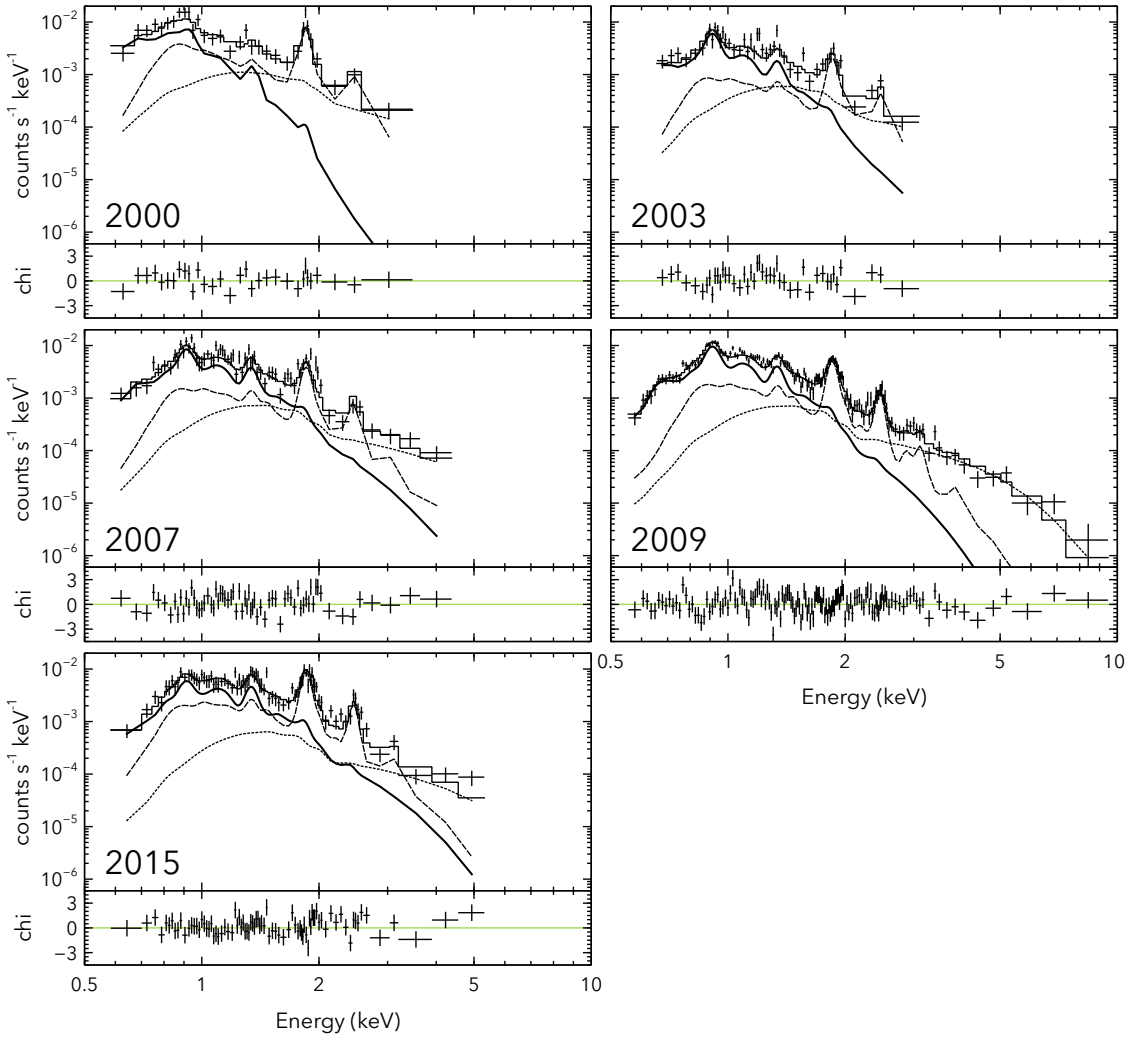

Figure 5.15: Spectra extracted from the Knot1 regions. The solid curve is the NEI component originating from ISM. The other curves represent the same components as Figure 5.13.

Figure 5.15 presents the spectra of Knot1 and the results of the spectral fit. Table 5.3 lists the best-fit parameters. It is confirmed that we can ascribe the time variability solely to the additional soft component. Given that the NEI model with the solar abundance effectively reproduces the Knot1 spectra in the soft band, the soft component is likely associated with ISM heated up by the blast wave. For a more detailed examination of the variability, Figure 5.16 depicts the value of kT_e, $n_e t$, and EM in each year. The results with $n_e t$ in 2000 as a free parameter are also shown in the same figure. The figure indicates that kT_e increases significantly from $0.30^{+0.05}_{-0.07}$ to $0.69^{+0.16}_{-0.12}$, which is almost equal in the other case. We further validate this by considering the kT_e change when $n_e t$ is fixed to 8×10^9 cm^{-3} s, positioned between the best-fit value (9×10^{10} cm^{-3} s) and the fixed value (4×10^9 cm^{-3} s). In this scenario, the best-fit value of kT_e in 2000, 2003, 2007, 2009, and 2015 are $0.47^{+0.20}_{-0.28}$, $0.42^{+0.10}_{-0.04}$, $0.59^{+0.13}_{-0.10}$, $0.53^{+0.03}_{-0.06}$, and $0.70^{+0.14}_{-0.13}$ keV, respectively.

Considering the observed kT_e increase, we also employ the `gnei` model as the soft component. The `gnei` model allows the ionization timescale averaged temperature to

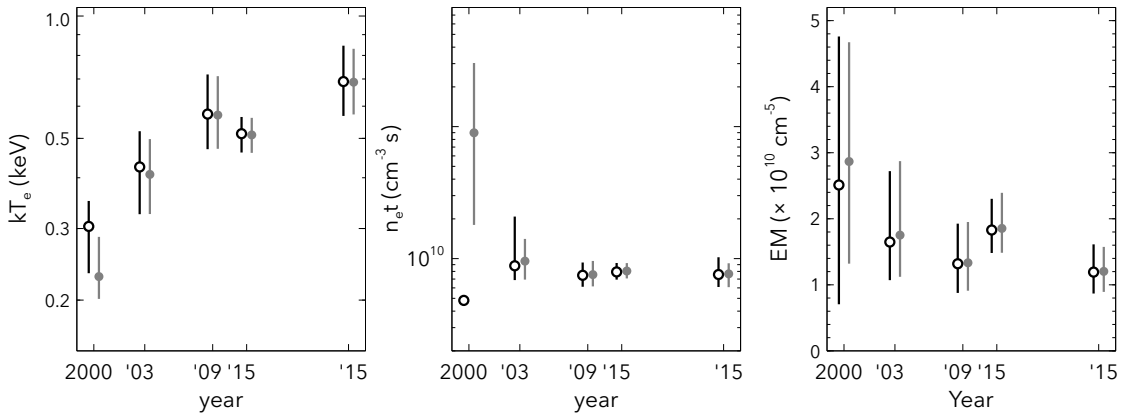

Figure 5.16: The best-fit values of kT_e, $n_e t$, and EM of the soft NEI component as a function of year. The black and gray plots correspond to the case in which $n_e t$ is fixed to 4×10^9 cm^{-3} s, and is free, respectively.

deviate from the current temperature. The resulting value of kT_e in `gnei` are $0.26^{+0.07}_{-0.05}$, $0.37^{+0.09}_{-0.07}$, $0.57^{+0.13}_{-0.10}$, $0.52^{+0.05}_{-0.07}$, and $0.70^{+0.17}_{-0.13}$ keV in 2000, 2003, 2007, 2009, and 2015, respectively, virtually identical to those obtained with the NEI model. Notably, there are no significant changes in $n_e t$ and EM over time. It can be interpreted that the observed flux change is a result of an increase in electron energy induced by shock heating.

5.4.2 Discussions

5.4.2.1 Origin of Knot1

As outlined in Section 5.4.1, Knot1 in Tycho exhibits a significant increase in soft-band X-ray flux. The result, coupled with the year-scale increase of the electron temperature, suggests that the blast wave recently heated a compact and dense clump. The model with the solar abundance successfully explains the spectra (see Table 5.3), indicating that the shock-heated gas originates from the ISM. However, we do not rule out the possibility of CSM origin, considering the known interaction with a cavity wall in southwestern shell (Tanaka et al., 2021). Note that Knot1 represents the first example of ISM/CSM X-ray emission in Tycho's SNR, which is known as an ejecta-dominated SNR. Future observations with improved statistics or spectroscopy could facilitate the measurement of elemental abundances, shedding light on the true origin and potentially providing clues to the progenitor system of Type Ia SN of Tycho's SNR.

Previous Hα observations have unveiled the presence of Balmer-dominated filaments in the northeast region of the remnant, interpreted as forward-shocked neutral gas and shock precursors (e.g., Ghavamian et al., 2000; J.-J. Lee et al., 2007). Figure 5.17 (the left and middle panels) compares the soft-band X-ray image from 2015 with the Hα image from 2012 (Knežević et al., 2017). This figure demonstrates a strong spatial correlation between the soft X-rays and a bright Hα structure in the Knot1 region, supporting the inference that the origin of Knot1 is associated with the ISM or CSM. It is

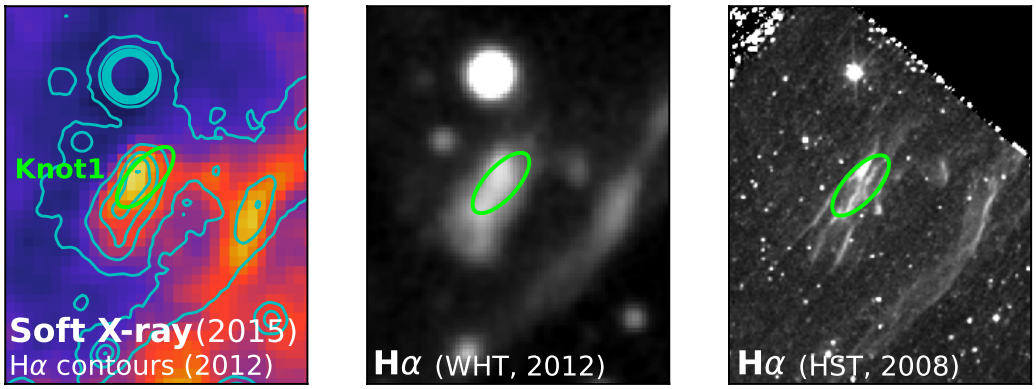

Figure 5.17: Spacial correlation of the Knot1 region between X-rays and Hα lines. In the left panel, the Chandra X-ray image captured in 2015 (same as the rightmost panel of Figure 5.11 (a)) is superimposed with contours from an Hα image obtained in 2012 (refer to the middle panel). The middle panel shows the Hα image, acquired in 2012 using GHαFaS on the William Herschel Telescope (WHT; Knežević et al., 2017). The right panel is the Hα image taken in 2008 with WFPC2 on HST (J.-J. Lee et al., 2010).

worth noting that we can observe the bright and complicated shell structure only around Knot1 in the entire Hα image on the northeast of the SNR taken with the HST (the right panel of Figure 5.17 and cf. J.-J. Lee et al., 2010). Similar localized filaments are found in other SNRs. For instance, Patnaude & Fesen (2007, 2014) found the region in which X-ray and H$alpha$ are spatially coincident ("XA" region) in SNR Cygnus Loop. Moreover, Patnaude & Fesen (2007, 2014) reported the time-variable X-ray knots originated from ejecta in Cassiopeia A, which spatially coincide with optical light, as mentioned in Section 3. Its physical scale is 0.02–0.03 pc, roughly consistent with the estimated size of Knot1: $\simeq$ 0.04 pc. While these structures in Cassiopeia A are interpreted as dense ejecta clumps engulfed by the reverse shock, Knot1 is likely to originate from a small-scale clumpy ISM/CSM heated by the forward shock.

The density of Knot1 can be estimated using the best-fit parameters as follows. Assuming that the emitting region of Knot1 takes the form of an oblate spheroid with long and short radii of 0.05 pc and 0.02 pc, respectively, we calculate its volume to be $V \simeq 6 \times 10^{51}$ cm^3. We derive a proton density of $n_{\rm H} = 35^{+6}_{-4}$ cm^{-3} utilizing the EM best-fit parameter of the soft component in 2015, $n_e n_{\rm H} V / 4\pi d^2 = (1.2^{+0.4}_{-0.3}) \times 10^{10}$ cm^{-5}. Contrastingly, the post-shock density of Tycho's SNR is estimated to be $n_{\rm H} = 0.1$–2 cm^{-3} based on the flux ratio of the 70 μm to 24 μm infrared emission (Williams et al., 2013), leading to the Knot1 density to be roughly 10–100 times higher than its surroundings.

5.4.2.2 Time Variability of Knot1

Time variability of Ionization Sate Given that the parameter $n_e t$ in XSPEC represents the ionization timescale in case of constant kT_e, the ionization timescale $n_e t$ cannot simply be considered as a product of density and actual time passed from the time in

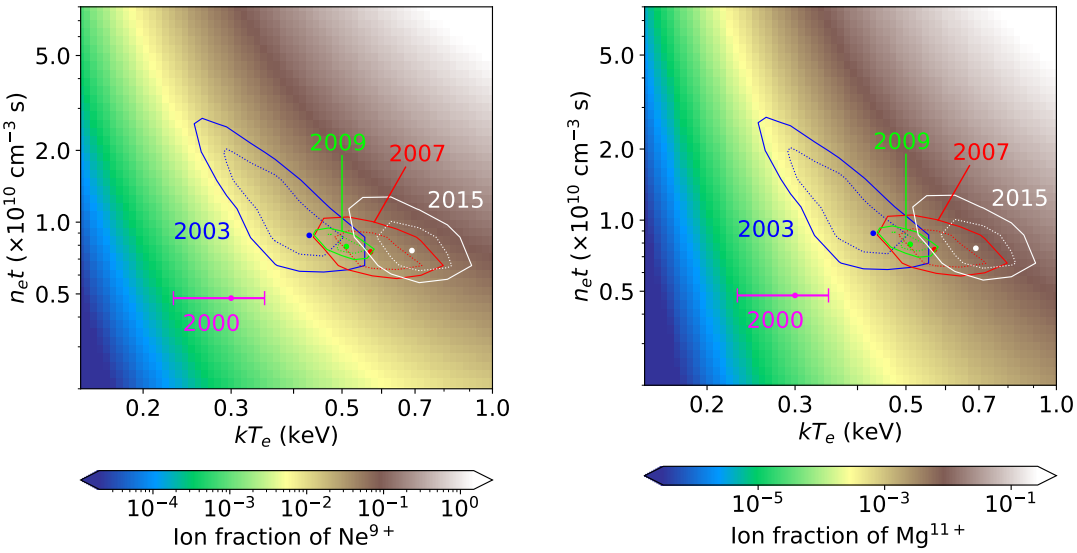

Figure 5.18: H-like ion fraction of neon (Ne^{9+}; left) and magnesium (Mg^{11+}; right) as a function of electron temperature (kT_e) and ionization timescale ($n_e t$). The contours represent the confidence level of $\Delta\chi = 1.0$ (dotted) and 2.3 (solid) in 2003 (blue), 2007 (red), 2009 (green), and 2015 (white). The points show the best-fit values in each year. The data in 2000 show only the uncertainty of kT_e because we fix $n_e t$ in this analysis. The ion fraction is the result of the calculation with PyAtomDB (Foster et al., 2017).

which shock passed. We thus discuss the change in the ionization state of Knot1 using ion fractions of the soft component each year. As depicted in Figure 5.18, H-like neon and magnesium are both increasing, suggesting the progression of ionization from 2003 to 2015. Therefore, we take into account that an SNR shock recently propagating into a small cloud has heated and ionized Knot1 from year to year.

Cloud Crushing Time The time scale of the property change for clump in ISM is often characterized by the cloud-crushing time (Klein et al., 1994). Let us consider the clump with the density ρ_c and the pressure P_c in ISM with the density ρ_i and the pressure P_i as depicted in Figure 5.19. Under an assumption of ram pressure equilibrium ($P_c = P_i$), the relation $\rho_i u_i^2 = \rho_c u_c^2$ can be derived from the Equation 1.2, where u is the shock velocities in the ISM (subscript i) and the clump (subscript c). Thus, we can describe the velocity of the shock decelerated inside the clump as follows:

$$u_c = \frac{u_i}{\chi^{1/2}}, \tag{5.6}$$

where χ ($\equiv \rho_c/\rho_i$) is the density contrast between the clump and ISM. The shock velocity inside the clump u_c can be determined to be 1500–2500 km s^{-1}, given that χ is estimated to be $\chi \sim 10$ from Section 5.4.2.1 and the typical forward-shock velocity u_i of Tycho's SNR is 4000–8000 km s^{-1} (Tanaka et al., 2021). A cloud-crushing time can be defined as follows:

$$t_{cc} \equiv \frac{\chi^{1/2} a_0}{u_i} = \frac{a_0}{u_c}. \tag{5.7}$$

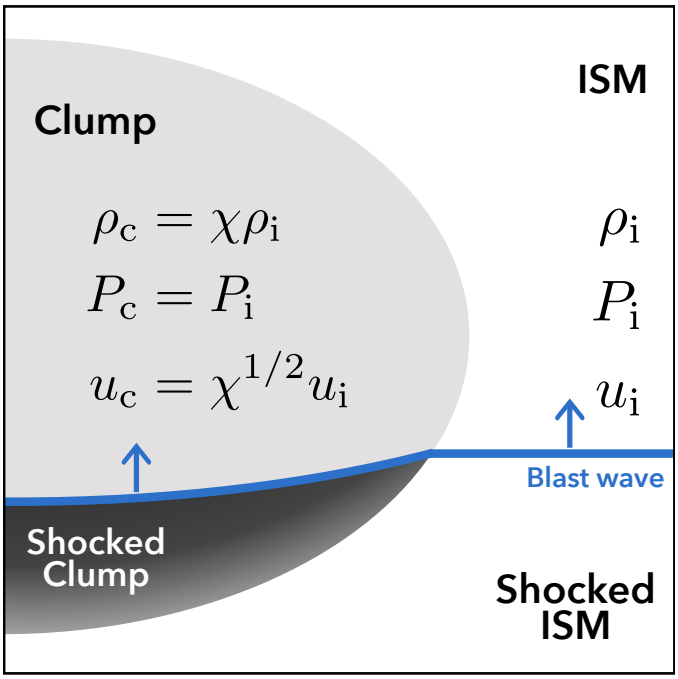

Figure 5.19: Schematic of the Knot1 region and the shock waves.

Here, a_0 is the radius of the clumps. The emitting region of Knot1 has a radius of $a_0 \simeq 0.02$ pc, the cloud-crushing time can be calculated as $t_{cc} = 18 \times (u_i/2000 \text{ km s}^{-1})^{-1}$ yr. Note that the result is roughly consistent with the year-scale change of the X-ray flux in Knot1. However, the X-ray-emitting volume should increase over time in this scenario, leading to the increasing EM. This contradicts the observed result. Considering the multiple filaments discovered with the HST image (Figure 5.17 right), Knot1 is thought to constrain multiple clumps with radii finer than $a_0 = 0.02$ pc, leading to a shorter cloud-crushing time. Thus, the more likely scenario is that the brightening is attributed to the kT_e increase after the shock wave has passed on a short timescale of about one year.

Heating Timescale For an explanation of the observed increase in kT_e, we first consider the case of thermal equilibration via electron–ion Coulomb collisions without collisionless heating at the shock transition region. The temperature immediately downstream for shock velocity u_c derive from Equation (1.20):

$$kT_i = \frac{3}{16} m_i u_c^2. \tag{5.8}$$

Given that the electron temperature T_e is initially lower than the ion temperature T_i in downstream plasma, the electron temperature is expected to increase monotonically. The time evolution is described by Equation (1.22) and (1.23). A convenient expression of the Coulomb logarithm can be given for X-ray emitting plasma (Masai, 1984):

$$\ln \Lambda = 24.8 + \ln \left[\left(\frac{kT_e}{\text{eV}} \right) \left(\frac{n_e}{\text{cm}^{-3}} \right)^{-1/2} \right]. \tag{5.9}$$

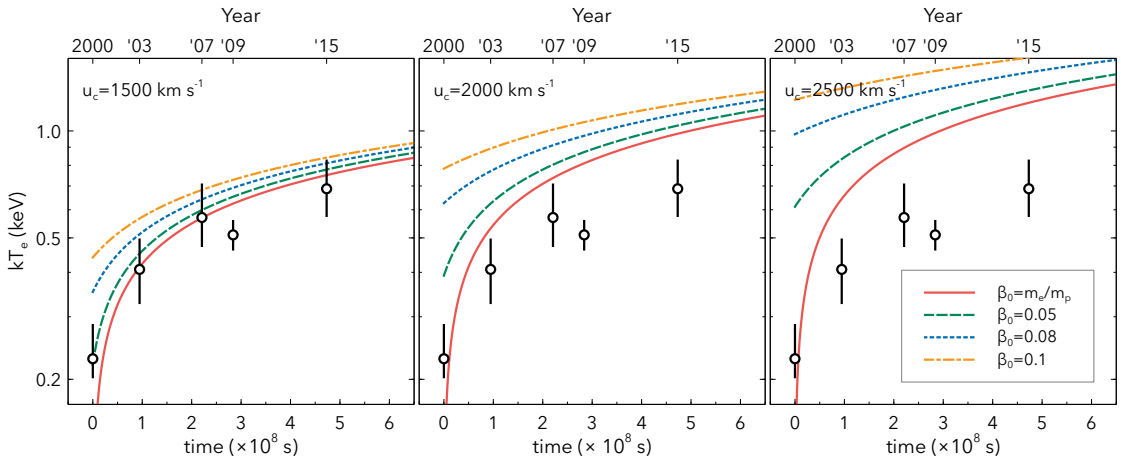

Figure 5.20: The comparison electron temperature as a function of the time between the observation and the calculation assuming the shock velocity in the clump to be u_c = 1500 (left), 2000 (middle), and 2500 km s^{-1}(right). The plots represent the observed results, and the curves are the calculation results when $\beta_0 = m_e/m_p$ (red), 0.05 (green), 0.08 (blue), and 0.1 (yellow).

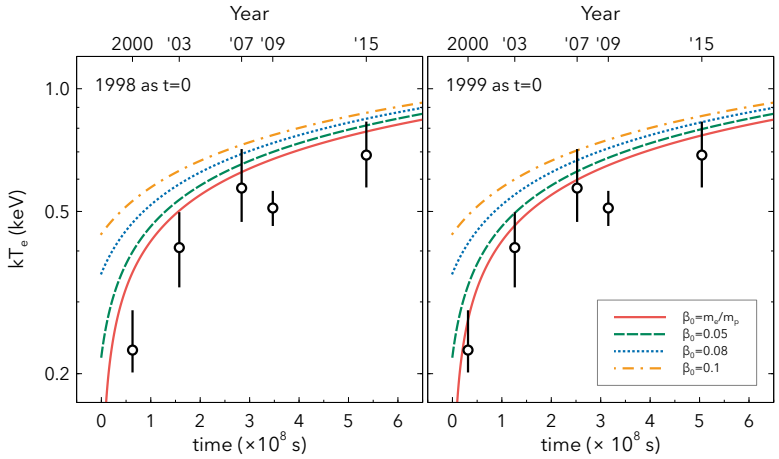

Figure 5.21: Same as Figure 5.20, but the time in which the shock heating was started is assumed to be 1998 (left) and 1999 (right)

We adopt an electron number density n_e = 42 cm^{-3} based on $n_{\rm H}$ = 35 cm^{-3} (Section 5.4.2.1) and $n_e = 1.2 n_{\rm H}$. Neglecting contributions from ions heavier than hydrogen for simplicity, the time evolution of kT_e can be calculated as shown in Figure 5.20. The electron-to-proton temperature ratio ($\beta_0 \equiv T_e/T_p$) at $t = 0$ without collisionless electron heating is equivalent to the particle mass ratio, i.e., $\beta_0 = m_e/m_p \simeq 5 \times 10^{-4}$. Based on the above estimation, we give the case in which the shock velocity inside the clump u_c is 1500, 2000, 2500 km s^{-1}. The timescale in which kT_e reaches around 0.7 keV (the value derived from data in 2015) becomes short as the shock velocity increases. This is because the greater the shock velocity, the larger the temperature difference between electrons and protons. Figure 5.20 indicates that the model for u_c = 1500 km s^{-1} can explain the observed data. While the plausible range of the shock velocity u_c is between 1500 km s^{-1} to 2000 km s^{-1} as estimated above, the lower velocity case is discussed in Appendix A. The timescale reaching kT_e = 0.7 is longer than observed in this scenario.

For astrophysical shocks, collisionless electron heating is often effective at the shock transition, as explained in Section 1.2.4. Secondly, let us consider this case. In this case, the ratio β_0 becomes larger than m_e/m_p ($\simeq 5 \times 10^{-4}$). We calculate the temperature evolution when $\beta_0 = 0.05$, 0.08, and 0.1 as plotted in Figure 5.20. When $m_e/m_p \leq \beta_0 \leq 0.05$, the model is in good agreement with the data. Considering the uncertainty regarding when the forward shock indeed hit Knot1, we also conduct comparisons using calculations with different assumptions about $t = 0$, specifically for $u_0 = 1500$ km s^{-1}, as illustrated Figure 5.21. Even when the year 1998 corresponds to $t = 0$, observed data can still be explained by the model with $m_e/m_p \leq \beta_0 \leq 0.05$. However, it seems more plausible when the year 1999 corresponds to $t = 0$.

Optical observations also estimate β_0 of some SNRs with different shock velocities using flux ratios of the broad-to-narrow components of the Hα line (e.g., van Adelsberg et al., 2008, also see Section 1.2.4). Especially with regard to Tycho's SNR, Ghavamian et al. (2001) and van Adelsberg et al. (2008) obtained $\beta_0 < 0.1$ and $\beta_0 = 0.046^{+0.007}_{-0.006}$, respectively, in "knot g" region, located $\sim 2'$ southeast of Knot1. In other SNRs with strong shocks of $v_{\rm sh} > 1000$ km s^{-1}including SN 1006 and Kepler's SNR, the temperature rato β_0 is given as $\beta_0 \sim 0.05$ (Fesen et al., 1989; Ghavamian et al., 2002). From our comparison of the observations with the calculations, Knot1 has $m_e/m_p \leq \beta_0 \leq 0.05$ with a shock velocity of ~ 1500 km s^{-1}. It suggests that collisionless electron heating in Knot1 has a comparable efficiency with the result of the previous Hα observations.

The measurement of β_0 in X-rays has not been definitive, except for the diagnostics of low-ionized Fe fluorescence emission proposed by Yamaguchi et al. (2014). This uncertainty stems from the challenges of selective analysis of X-ray-emitting plasma that has not yet been influenced by Coulomb heating. Therefore, Hα line diagnostics are often employed for the measurement, as they can measure β_0 in just the region where hydrogen atoms have not reached a fully ionized state, coinciding with the area where collisionless electron heating is effective. However, estimations using the Hα line come with systematic uncertainties in shock models (e.g., van Adelsberg et al., 2008). The analysis presented in this thesis introduces a new method for estimating β_0 independently of the Hα measurements.

Table 5.3: Best-fit Parameters of Refl and Knot1 Regions

Components	Parameters (Units)	2000	2003	2007	2009	2015
Absorption	$N_{\rm H}$ (10^{22} cm^{-2})			$1.01^{+0.04}_{-0.03}$		
Refl region						
NEI comp.	EM* (10^{9} cm^{-5})	$2.4^{+1.3}_{-1.1}$	$1.6^{+1.4}_{-1.2}$	$2.3^{+1.3}_{-1.2}$	$3.0^{+1.4}_{-1.2}$	$5.2^{+2.2}_{-2.0}$
	kT_e (keV)			0.70 ± 0.03		
	$n_e t$ (10^{11} cm^{-3} s)			$5.0^{+1.3}_{-1.2}$		
	[Mg/C]/[Mg/C]$_\odot$			$1.4^{+0.8}_{-0.4}$		
	[Si/C]/[Si/C]$_\odot$			11^{+5}_{-3}		
	[S/C]/[S/C]$_\odot$			11^{+6}_{-3}		
	[Ar/C]/[Ar/C]$_\odot$(=[Ca/C]/[Ca/C]$_\odot$)			9^{+6}_{-4}		
	[Fe/C]/[Fe/C]$_\odot$(=[Ni/C]/[Ni/C]$_\odot$)			$1.1^{+0.8}_{-0.4}$		
Power law	Γ			2.79 (fixed)		
	Flux† (10^{-15} erg cm^{-2} s^{-1})			1.7 ± 0.1		
Knot1 region						
Soft comp.	EM‡ (10^{10} cm^{-5})	$2.5^{+2.2}_{-1.8}$	$1.6^{+1.1}_{-0.6}$	$1.3^{+0.6}_{-0.4}$	$1.8^{+0.4}_{-0.3}$	$1.2^{+0.4}_{-0.3}$
	kT_e (keV)	$0.30^{+0.05}_{-0.07}$	0.43 ± 0.10	$0.57^{+0.14}_{-0.10}$	0.51 ± 0.05	$0.69^{+0.16}_{-0.12}$
	$n_e t$ (10^{9} cm^{-3} s)	4.8	$8.8^{+12.0}_{-1.9}$	$7.5^{+1.9}_{-1.4}$	$7.9^{+1.3}_{-1.0}$	$7.6^{+2.7}_{-1.5}$
	abundance			fixed to the solar value		
Reference comp.¶	EM* (10^{9} cm^{-5})	$2.4^{+1.0}_{-0.9}$	$1.4^{+0.7}_{-0.3}$	$2.3^{+1.0}_{-0.9}$	$2.9^{+1.1}_{-1.0}$	$5.2^{+2.4}_{-2.1}$
Power law	Γ			2.79 (linked to Refl)		
	Flux† (10^{-15} erg cm^{-2} s^{-1})			1.7 (linked to Refl)		
χ^2 (d.o.f.)				731 (629)		

* EMs for the NEI components are defined as $\int n_e n_{\rm C} dV/(4\pi d^2 [{\rm C/H}]_\odot)$.

† The energy flux in the energy band of 4–6 keV.

‡ EMs for the soft components are defined as $\int n_e n_{\rm H} dV/4\pi d^2$.

¶ The parameters of the reference components other than the EMs are linked to the NEI component for the Refl region.

6

Future Works

Contents

6.1 Overview

In Chapter 5, we presented the energy-transfer investigations of the shock-heated or shock-accelerated particles through X-ray time variabilities. These phenomena are frequently observed in regions where SNR shocks interact with dense clouds (e.g., Ghavamian et al., 2000; Ackermann et al., 2013). We can also raise the possibility of an interaction between shock and dense cloud in Tycho's SNR from both the magnetic field amplification suggested in Section 5.3 and the discovery of shock-heated clumps in Section 5.4. Tanaka et al. (2021) reported indications of recent collisions of shock with the wall using the remnant expansion (see Chapter 3). In Section 6.2, we measure the shock velocity with newly observed Chandra data to investigate further the surrounding environments of Tycho's SNR.

The analysis in Section 5.4 confined β_0 in Knot1 of Tycho's SNR, introducing a new method to measure β_0 independently of a previous measurement with Hα observation. To enhance the usefulness and reliability of the method, we propose two applications in Section 6.3 and 6.4. In Section 6.3, we search for the time variabilities in Kepler's SNR,

Table 6.1: Observation Log for Proper-Motion Analysis

ObsID	Start Date	Effective Exposure (ks)	Chip
24420	2021 May 20	14.88	ACIS-I
25046	2021 May 21	14.71	ACIS-I
23538	2021 Sep 27	28.70	ACIS-I
24419	2021 Oct 01	28.70	ACIS-I
24421	2021 Oct 17	29.69	ACIS-I
24418	2022 May 25	14.88	ACIS-I
26426	2022 May 26	14.88	ACIS-I

considering possibilities to understand the spatial dependences of β_0. In Section 6.4, we discuss the application to time variabilities of ion temperatures with high-resolution spectroscopy to compare the time evolution of electron temperature.

6.2 Probing the Shock–Cloud Interaction from Variability of Expansion Velosity

6.2.1 Our Objectives

The shock waves of Tycho's SNR are likely to have various properties, e.g., velocities and pre-shock densities. Katsuda et al. (2010) estimated the pre-shock ambient density surrounding Tycho's SNR to have azimuthal non-uniformity from the proper motion measurement of the forward shock. Williams et al. (2013) also reported the azimuthal density distribution from the infrared flux ratio with *Spitzer*. As explained in Chapter 3, Tanaka et al. (2021) indicated a recent shock–wall interaction from the time variabilities of shock velocities. From these studies, we can expect the various shock properties in the azimuthal angle and the time. It is crucial to comprehend the impact of the shock–wall interaction on the shock properties in terms of not only the shock physics but also its potential to constrain the characteristics of the progenitor system. This section presents the analysis results of new data observed in 2022–2023 with Chandra added to data used by Tanaka et al. (2021) and future prospects, aiming to study the proper motion after 2015 and the spectral variability of synchrotron radiation as a result of the changes of shock properties.

6.2.2 Observations and Data Reductions

We use the Chandra data taken in 2021–2022 as a guest observer program proposed by Williams (2020), in addition to the data used in Chapter 5. Table 6.1 shows the additional data log. Similar to the analysis in Chapter 5, we conduct astrometry correction for the data of ObsID 24420, 25046, 24418, and 26426, which are thought to have almost no annual parallax for point sources. Since the statistic of each observation is too low,

we cannot detect enough point sources to correct the astrometry. Thus, after merging the observations, we detect the sources and correct the astrometry in the same way as Section 5.2. We used the data after the correction for imaging analysis, and the total effective exposure time is 59.35 ks. For spectral analysis, we add the data of ObsID 23538, 24419, and 24421, whose astrometries are not corrected, to improve the statistic, resulting in a total exposure time of 146.44 ks.

6.2.3 Analysis and Results

6.2.3.1 Imaging Analysis

We used the Chandra flux image in the energy band of 4.1–6.1 keV, where the synchrotron emission is dominant, as mentioned in Section 5.3.1 for the profile extraction. Radial profiles are extracted from the regions positioned at the rim of the remnant (labeled as "1–13" in Figure 6.1 (top)). These regions are the same as those used by Tanaka et al. (2021). The box rotation angles are determined by hand in order to extract the profile perpendicular to the rim. The bin width of the profile is 0.″5. Examples of the profiles are shown in Figure 6.2. The shock position corresponds to the peak of the profile. The profiles in the regions generally move over the years, as discovered by Katsuda et al. (2010), Williams et al. (2016), and Tanaka et al. (2021).

We investigated rim expansion using the same method as Tanaka et al. (2021). We explored the displacement distance to achieve the best alignment between the rim peaks in the profiles from two epochs through an artificial shifting of one profile. This distance can correspond to the actual distance traveled by the rim. When the shift distance is non-integer multiples of the bin, the shifted profile is reconstructed by distributing the counts between two bins using a weighted binomial distribution. Comparing two profiles with flux f_i and g_i of bin index i, we calculate chi-squared defined as:

$$\chi^2 = \sum_i \frac{(f_i - g_i)^2}{(df_i)^2 + (dg_i)^2}, \tag{6.1}$$

where df and dg are the standard deviations of each profile. We used the chi-squared as the quantified degree of matching between the profiles. The obtained chi-squared is shown in Figure 6.3. The velocity that makes chi-squared the minimum value $\chi_{\rm min}$ is obtained by fitting with a quadratic function, as can be seen from the figure. The 1σ confidence range is defined as the range to be $\chi \leq \chi_{\rm min} + 1$.

The velocity of the shock proper motion is measured in three intervals: 2003–2009 (interval A), 2009–2015 (interval B), and 2015–2021 (interval C). The results are represented in Figure 6.4 and Table 6.2. The decelerations in the interval A and B in Region #6–11 are consistent with the previous measurement by Tanaka et al. (2021). Focusing on Region #8 and #9, we reveal that the shock waves decelerated further until 2021. Additionally, the deceleration is shown in Regions #12 and 13, where the analysis by Tanaka et al. (2021) reported constant velocities. On the other hand, Regions #5–7, where Tanaka et al. (2021) discovered significant deceleration from 2003 to 2015, show no significant velocity change between the intervals B and C.

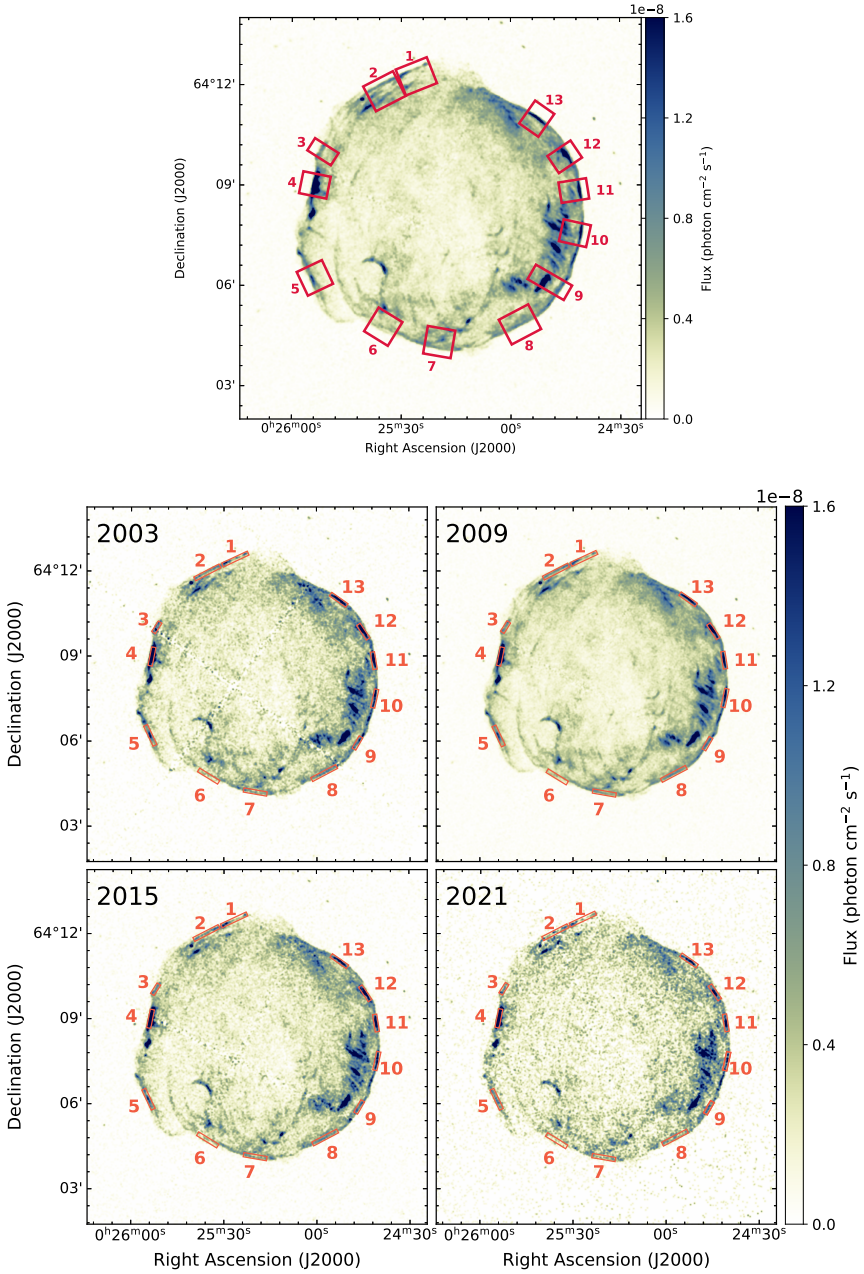

Figure 6.1: (Top): The flux image of Tycho's SNR in the energy band 4.1–6.1 keV taken with Chandra in 2009. The red boxes are the regions to extract profiles. (Bottom): The flux images obtained in 2003, 2007, 2009, and 2015. The orange boxes represent regions for spectral extractions.

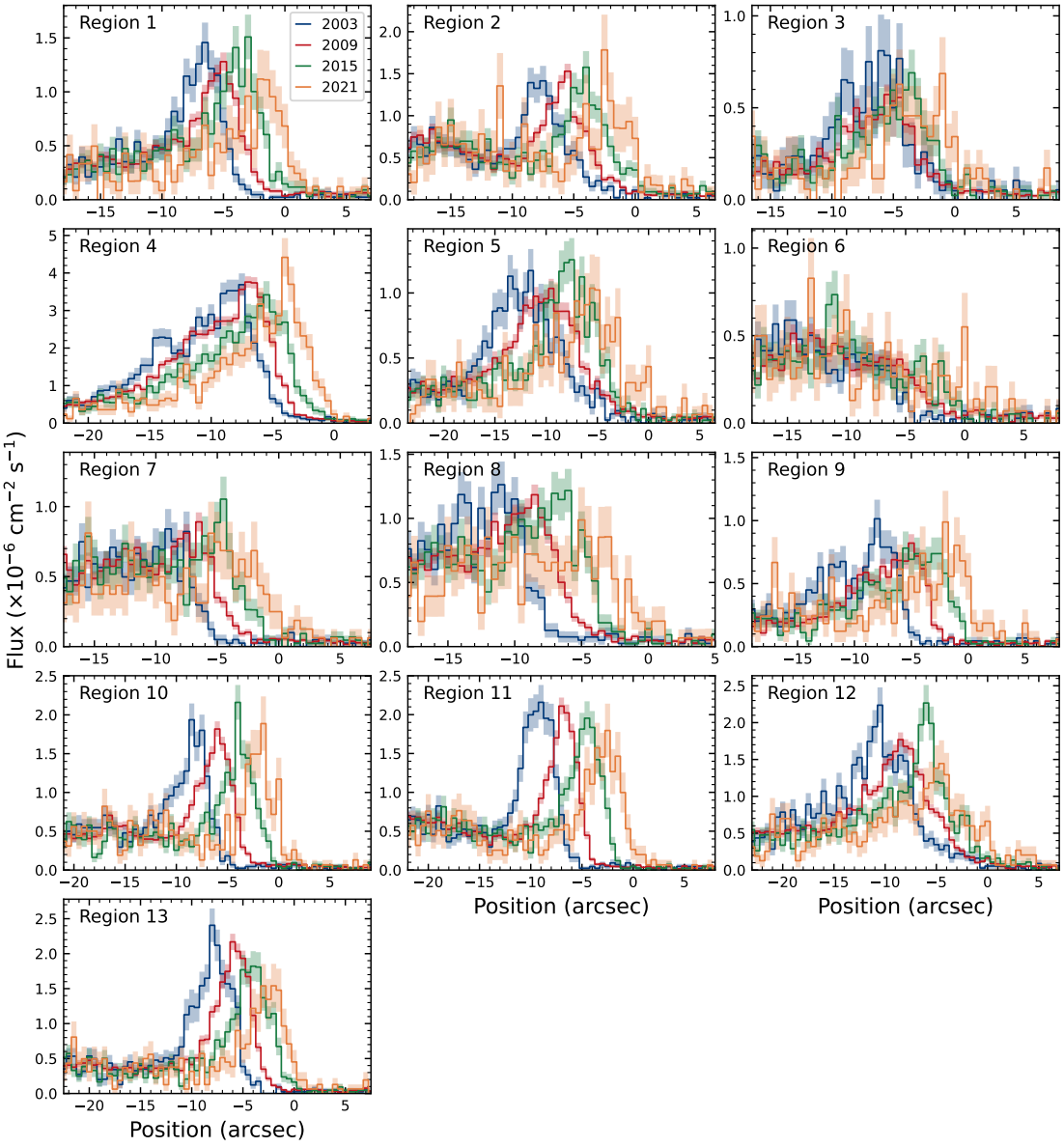

Figure 6.2: Radial profiles of the shocks of Tycho's SNR extracted from each region. The blue, red, green, and yellow lines represent the 2003, 2009, 2015, and 2021 data, respectively. The x-axes show the distance from the rim position in 2021 in the outward direction.

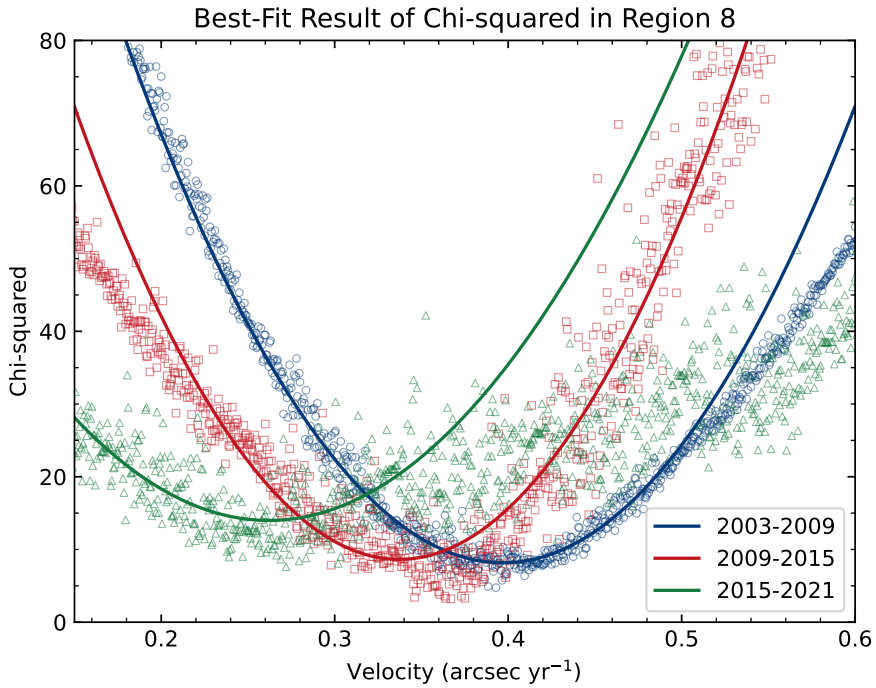

Figure 6.3: The chi-squared in measuring the rim proper motion and the best-fit quadratic function in Region #8. The chi-squared is calculated from Equation (6.1) by moving a profile artificially under assumptions of given shock velocities in intervals of 2003–2009 (blue), 2009–2015 (red), and 2015–2021 (green).

Table 6.2: The observed proper motions of shock waves

Region No.	2003–2009 (arcsec yr^{-1})	2009–2015 (arcsec yr^{-1})	2015–2021 (arcsec yr^{-1})
1	0.25 ± 0.02	0.26 ± 0.02	0.31 ± 0.04
2	0.30 ± 0.02	0.29 ± 0.02	0.27 ± 0.04
3	0.14 ± 0.03	0.20 ± 0.05	0.20 ± 0.04
4	0.22 ± 0.01	0.23 ± 0.01	0.25 ± 0.03
5	0.28 ± 0.03	0.25 ± 0.03	0.24 ± 0.05
6	0.43 ± 0.04	0.30 ± 0.06	0.27 ± 0.04
7	0.35 ± 0.02	0.27 ± 0.03	0.25 ± 0.07
8	0.40 ± 0.03	0.34 ± 0.02	0.26 ± 0.03
9	0.39 ± 0.02	0.32 ± 0.03	0.21 ± 0.05
10	0.39 ± 0.01	0.37 ± 0.01	0.31 ± 0.01
11	0.39 ± 0.01	0.38 ± 0.01	0.30 ± 0.03
12	0.31 ± 0.03	0.33 ± 0.02	0.22 ± 0.04
13	0.30 ± 0.01	0.31 ± 0.02	0.22 ± 0.03

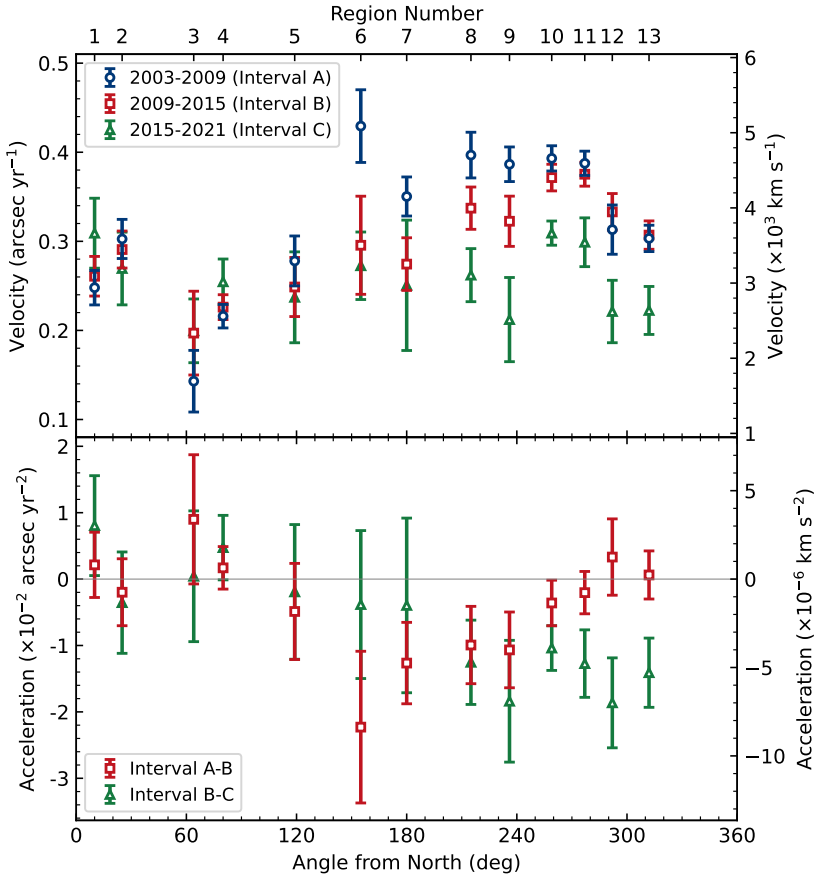

Figure 6.4: The shock velocities (top) and accelerations (bottom) in each region as a function of the azimuthal angle. In the top panel, the circle, squared, and triangle plots represent the velocities in 2003–2009 (Interval A), 2009–2015 (Interval B), and 2015–2021 (Interval C), respectively. The plots in the bottom panel show the acceleration rate in Interval A–B (square) and B–C (triangle) under an assumption of the constant rate over the interval. The angle is measured from the north direction based on the geometric center ($\alpha = 00^{\rm h}25^{\rm m}19\overset{\rm s}{.}9$, $\delta = 64^\circ08'18\overset{''}{.}2$ (J2000)) measured by Ruiz-Lapuente et al. (2004).

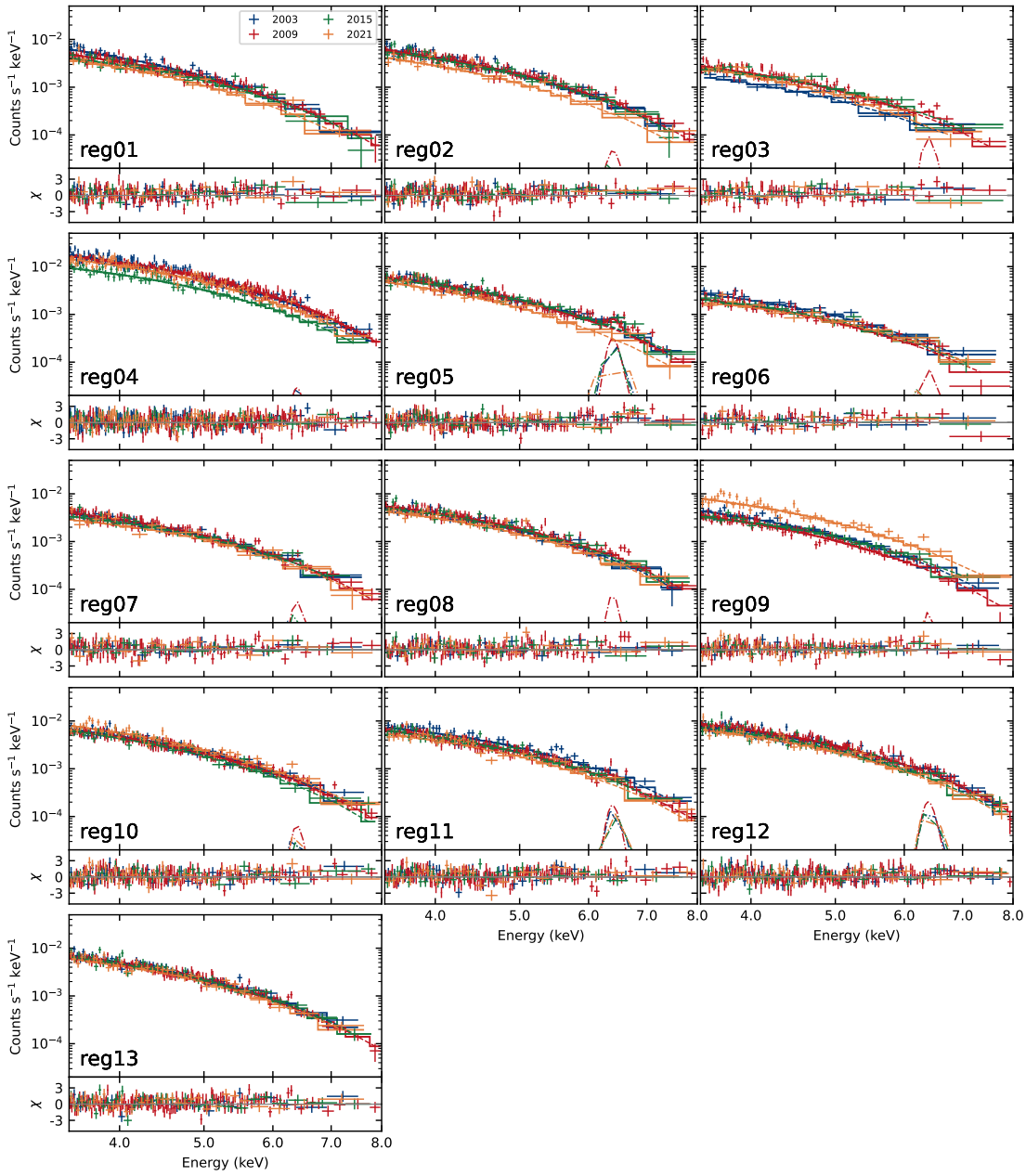

Figure 6.5: Fitting result of the spectra extracted from Regions #1–13. The blue, red, green, and yellow plots correspond to the 2003, 2009, 2015, and 2021 data. The dashed and dash-dotted curves represent the power-law and Gaussian components. The solid steps are the total model of all components.

6.2.3.2 Spectral Analysis

The shock-velocity changes can change synchrotron emission properties from the rim. To investigate the changes in the synchrotron radiation, we extract the spectra from regions represented in Figure 6.1 (bottom). Each region has a width of 0.″15, located at the bright rim structure. The extracted spectra are binned so that each bin has at least ten

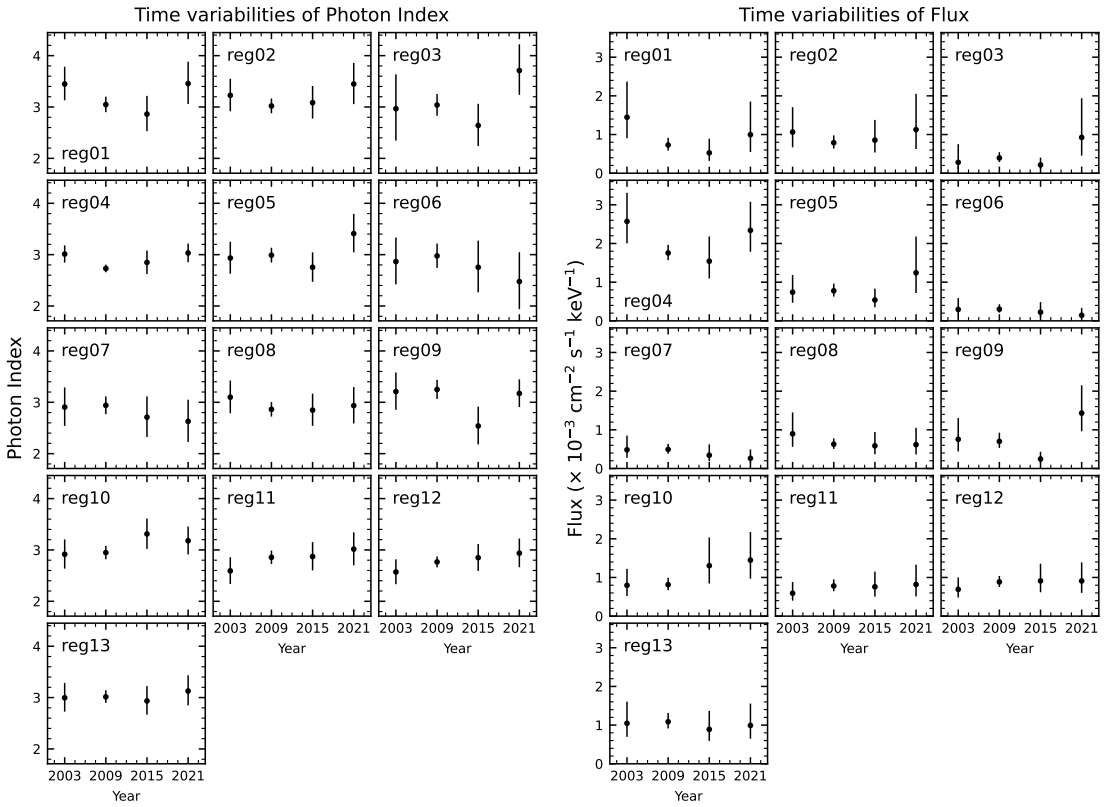

Figure 6.6: The best-fit parameters of the power-law component, i.e., photon index (left) and flux (right), as a function of the observed year.

counts. The analyzing range is 3.5–8.0 keV, where the synchrotron emission dominates. Although radiation from these regions consists mainly of synchrotron emission, some spectra demonstrate peaks around 6.4 keV, corresponding to the energy of a Fe Kα fluorescence line. Thus, we used a power-law function for synchrotron radiation and a Gaussian for a Fe Kα line to reproduce the spectra. We allow flux and photon index (Γ) to vary in different years while parameters of the Gaussian are linked each year. The centroid energy of the Gaussian component is fixed at 6.4 keV. We multiplied these two components by the absorption model (the Tüebingen-Boulder model; Wilms et al., 2000). The column density for the absorption model is fixed at the best-fit value in Section 5.4, $n_{\rm H} = 1.0 \times 10^{22}$ cm^{-2}, because it can not be determined in the analyzed energy band. The extracted spectra and the best-fit models are shown in Figure 6.5, and the best-fit parameters are listed in Table 6.3. We can reproduce the extracted spectra with the power law model with a Gaussian.

We plot the best-fit parameters as a function of years in Figure 6.6. As seen in the figure, the spectral analysis reveals no significant time-variabilities that exceed the 90% (= 1.64σ) confidence interval. However, focusing on Region #10–12, there are increasing trends in photon indices.

Table 6.3: Best-Fit Parameters of Spectral Analysis

		Power law		Gaussian[1]
Region No.	Year	Γ	Flux[2]	Norm.[3]
1	2003	3.4 ± 0.3	$1.4^{+0.9}_{-0.5}$	≤ 1.1
	2009	$3.0^{+0.2}_{-0.1}$	$0.7^{+0.2}_{-0.1}$	
	2015	$2.9^{+0.4}_{-0.3}$	$0.5^{+0.3}_{-0.2}$	
	2021	3.5 ± 0.4	$1.0^{+0.9}_{-0.4}$	
2	2003	3.2 ± 0.4	$1.1^{+0.6}_{-0.4}$	≤ 1.5
	2009	3.0 ± 0.1	0.8 ± 0.2	
	2015	3.1 ± 0.3	$0.9^{+0.5}_{-0.3}$	
	2021	3.4 ± 0.4	$1.1^{+0.9}_{-0.5}$	
3	2003	$3.0^{+0.7}_{-0.6}$	$0.3^{+0.5}_{-0.2}$	$1.5^{+1.2}_{-1.1}$
	2009	3.0 ± 0.2	0.4 ± 0.1	
	2015	2.6 ± 0.4	$0.2^{+0.2}_{-0.1}$	
	2021	3.7 ± 0.5	$0.9^{+1.0}_{-0.5}$	
4	2003	3.0 ± 0.2	$2.6^{+0.7}_{-0.6}$	≤ 2.6
	2009	2.7 ± 0.1	1.8 ± 0.2	
	2015	2.8 ± 0.2	$1.5^{+0.6}_{-0.4}$	
	2021	3.0 ± 0.2	$2.3^{+0.7}_{-0.6}$	
5	2003	2.9 ± 0.3	$0.7^{+0.4}_{-0.3}$	5.1 ± 1.8
	2009	3.0 ± 0.1	$0.8^{+0.2}_{-0.1}$	
	2015	2.8 ± 0.3	$0.5^{+0.3}_{-0.2}$	
	2021	3.4 ± 0.4	$1.2^{+0.9}_{-0.5}$	
6	2003	$2.9^{+0.5}_{-0.4}$	$0.3^{+0.3}_{-0.1}$	1.5 ± 1.3
	2009	3.0 ± 0.2	0.3 ± 0.1	
	2015	2.8 ± 0.5	$0.2^{+0.2}_{-0.1}$	
	2021	$2.5^{+0.6}_{-0.5}$	$0.14^{+0.19}_{-0.08}$	
7	2003	2.9 ± 0.4	$0.5^{+0.4}_{-0.2}$	≤ 1.4
	2009	2.9 ± 0.2	0.5 ± 0.1	
	2015	2.7 ± 0.4	$0.3^{+0.3}_{-0.2}$	
	2021	2.6 ± 0.4	$0.3^{+0.2}_{-0.1}$	
8	2003	3.1 ± 0.3	$0.9^{+0.6}_{-0.3}$	1.5 ± 1.5
	2009	2.9 ± 0.1	0.6 ± 0.1	
	2015	2.8 ± 0.3	$0.6^{+0.4}_{-0.2}$	
	2021	$2.9^{+0.4}_{-0.3}$	$0.6^{+0.4}_{-0.3}$	
9	2003	3.2 ± 0.4	$0.8^{+0.5}_{-0.3}$	≤ 1.1
	2009	3.2 ± 0.2	0.7 ± 0.2	
	2015	2.5 ± 0.4	0.2 ± 0.1	

Continued on the next page

Table 6.3: Best-Fit Parameters of Spectral Analysis (*Contunued*)

Region	Year	PhoIndex	Flux[2]	Norm.[3]
9	2021	3.1 ± 0.3	$1.4^{+0.7}_{-0.5}$	≤ 1.1
10	2003	2.9 ± 0.3	$0.8^{0.4}_{-0.3}$	≤ 1.5
	2009	2.9 ± 0.1	$0.8^{+0.2}_{-0.1}$	
	2015	3.3 ± 0.3	$1.3^{+0.7}_{-0.5}$	
	2021	3.2 ± 0.3	$1.4^{+0.7}_{-0.5}$	
11	2003	2.6 ± 0.3	$0.6^{+0.3}_{-0.2}$	2.9 ± 1.8
	2009	2.9 ± 0.1	$0.8^{+0.2}_{-0.1}$	
	2015	2.9 ± 0.3	$0.8^{+0.4}_{-0.3}$	
	2021	3.0 ± 0.3	$0.8^{+0.5}_{-0.3}$	
12	2003	2.6 ± 0.2	$0.7^{+0.3}_{-0.2}$	3.4 ± 2.1
	2009	2.8 ± 0.1	$0.9^{+0.2}_{-0.1}$	
	2015	2.8 ± 0.3	$0.9^{+0.4}_{-0.3}$	
	2021	2.9 ± 0.3	$0.9^{+0.5}_{-0.3}$	
13	2003	3.0 ± 0.3	$1.0^{+0.6}_{-0.3}$	≤ 1.7
	2009	3.0 ± 0.1	1.1 ± 0.2	
	2015	2.9 ± 0.3	$0.9^{+0.5}_{-0.3}$	
	2021	3.1 ± 0.3	$1.0^{+0.6}_{-0.3}$	

[1] The centroid energy is fixed at 6.4 keV.

[2] The flux at 1 keV. The unit is 10^{-3} ph keV^{-1} cm^{-2} s^{-1}

[3] The total photons in a line. The unit is 10^{-7} ph cm^{-2} s^{-1}

6.2.4 Discussion

Using Chandra data observed in 2021, our analysis reveals the proper motion of Tycho's SNR shock after 2015, where Tanaka et al. (2021) reported a deceleration in Regions #6–11 from 2003 to 2015. Tanaka et al. (2021) and Kobashi et al. (2023) proposed that shock deceleration is a consequence of interacting with a wall characterized by a spatial density gradient in the cavity-to-wall boundary. Assuming this hypothesis, it is likely that the shocks in Regions #6 and 7, which exhibit constant velocities from 2009 to 2021, have already traversed the gradient boundary. It follows that the shock had already reached the wall with a spatially constant density before 2009. On the other hand, shocks in Regions #8 and 9 show even lower velocities in interval C than those in interval B. Notably, the acceleration rate is almost the same between intervals A–B and B–C. This result indicates that shocks in these regions have been traversing the gradient boundary from 2003 to 2021. The shocks in Regions #10–13, which show larger deceleration from interval B to C than before, indicate more recent (around 2015) interaction with the wall than in the other regions.

Kobashi et al. (2023) studied the spatial density distribution surrounding Tycho's SNR using an updated hydrodynamic shock model considering an effect of a wind-like cavity

with $\rho(r) \propto r^{-2}$. Their model concluded that the shock in Region 11–13 indicated the interaction with the boundary before 2003, contradicting our results. This contradiction likely arises from an implicit assumption in their analysis: the boundary is inside the shock position in 2015. It is anticipated that the incorporation of our results, which indicate the start and end positions of the cavity-to-wall boundary layer, into their model will enable a more accurate determination of the cavity and wall locations, leading to a more precise estimation of the mass-loss rate from the progenitor system of the remnant.

The interaction of the shock with the wall might lead to changes in the properties of synchrotron radiation from the shock. Although the spectra exhibit no significant changes, we observe a softening from 2003 to 2015 in regions #10, 11, and 12, as can be seen from the increasing photon indices in Figure 6.5 (left). When attributing the change in photon index to the variation of the maximum electron energy, the decrease in shock velocity can cause softening, as suggested by $E_{\rm max} \propto v_{\rm sh}^2$ of Equation (1.40), given that the maximum energy of accelerated electrons is generally limited by the remnant age (Lopez et al., 2015). As the shock velocities in interval A become $\simeq$ 79%, $\simeq$ 77%, and $\simeq$ 70% in regions #10, 11, 12, respectively, the rolloff energy of synchrotron radiation should decrease to approximately 20–40% from $\varepsilon \propto v_{\rm sh}^4$ of Equation (2.30), likely affecting the photon index in the analyzed energy band.

However, the above scenario is rather simple and cannot explain the changes in other regions, especially regions #6, 7, 8, and 9, with the significant velocity decreases. One possibility is that the amplified magnetic field raises the cutoff energy. Inoue et al. (2012) indeed suggested that the interaction between shock waves and the clumpy interstellar medium can amplify the magnetic field after the shock through turbulent dynamo action by three-dimensional magnetohydrodynamic simulations. If the wall contains clumpy interstellar clouds, a more complex scenario is required to explain the photon index change.

In any case, discussing the spectral time variabilities based only on our results with insufficient statistics is challenging. Future long-duration observations with Chandra will enable us to study time variabilities in more detail. Additionally, a comparison with a hydrodynamical simulation of accelerated particle production in SNRs proposed by S.-H. Lee et al. (2012) will provide clues about the effect of the shock deceleration on the photon index.

6.3 Time Variabilities in Kepler's SNR

In the previous chapters, we present the discoveries of time variability in thermal X-rays, nonthermal X-rays, and the proper motions of shock waves in Tycho's SNR. This analysis can be applied to other regions in Tycho or other young SNRs. Exploring other thermal time variabilities can provide some clues to collisionless electron heating because it might allow us to investigate the dependency of electron–ion temperature ratio $T_e/T_{\rm ion}$ on other parameters: shock the velocity, the magnetic field, and the obliquity angle between shock normal and upstream magnetic field. Although the magnetic field

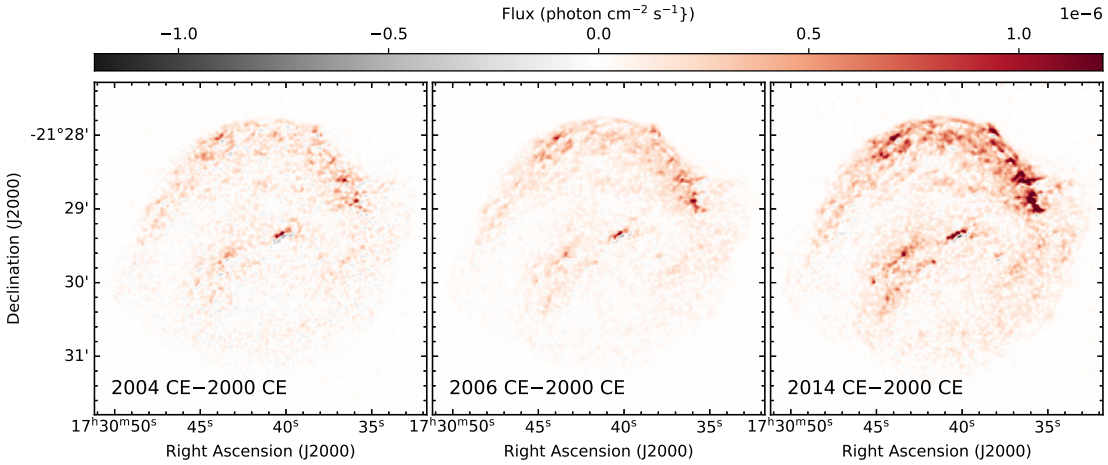

Figure 6.7: The images of flux change of Kepler's SNR in the energy band of 0.5–0.7 keV. The images are made by subtracting Chandra flux images taken in 2000 from 2004 (left), 2006 (middle), and 2014 (right). The positive values represent the brightening.

dependency is remarkably thought to affect the collisionless electron heating (Bohdan, 2023), there is poor observational evidence in SNRs.

We apply the methodology to Kepler's SNR, a remnant of SN 1604 located at 3–7 kpc (Kerzendorf et al., 2014). The remnant is a rare Type Ia event (e.g., Kinugasa & Tsunemi, 1999) whose thermal X-rays from CSM are detected (Reynolds et al., 2007; Katsuda et al., 2015). The CSM densities are estimated to be 10–100 cm^{-3}, comparable to that of Knot1 in Tycho's SNR in Chapter 5 (Matsuda et al., 2022). Since the thermal equilibrium timescale is proportional to a reciprocal of the plasma density, we can anticipate the detection of the time variability in a similar time scale as Knot1. Moreover, Reynolds et al. (2021) reported the spatial variations of magnetic field amplification in the shocks of Kepler's SNR. Thus, we can also expect the potential of comparisons between the magnetic field and $T_e/T_{\rm ion}$.

We conducted a search for significant flux changes in Kepler's SNR by making flux difference images using Chandra data from 2000, 2004, 2006, and 2014 (Figure 6.7). We identify a gradual brightening in 0.5–0.7 keV over a broad region, coinciding with bright thermal X-rays from CSM (Katsuda et al., 2015; Kasuga et al., 2021). It is noteworthy that the brightening region spatially aligns with an Hα+[N II] image (Sankrit et al., 2008). Figure 6.8 shows the spectra extracted from a region exhibiting significant brightening. The residuals between data and the model reveal an excess in the $\lesssim 1$ keV band only in 2014, with no corresponding excess in 2000, 2004, and 2006. By applying the analysis outlined in Section 5.3, we would unveil the dependence of the electron-to-ion temperature ratio $T_e/T_{\rm ion}$ on the magnetic fields.

The time variabilities in the broad region suggest that we can also observe time variability in other SNRs with bright thermal radiation from shocked ISM/CSM, such as N103B (Yamaguchi et al., 2021) and SNR 0519−69.0 (Guest et al., 2023). The application to several SNRs enables us to investigate $T_e/T_{\rm ion}$ in different shock velocities.

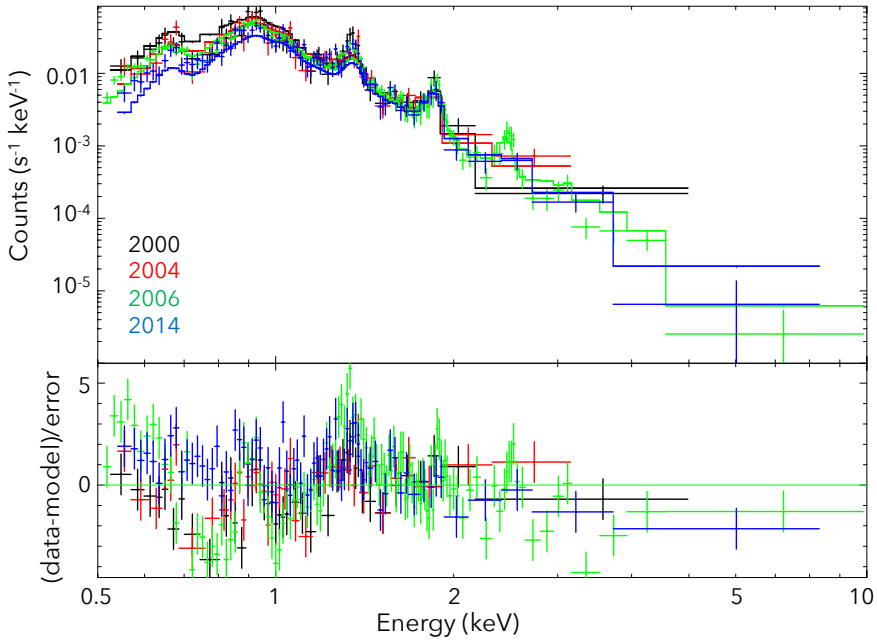

Figure 6.8: Example of the spectra which are extracted from the part of time variable region in Kepler's SNR. Black, red, green, and blue plots correspond to the data taken in 2000, 2004, 2006, and 2014. The models in each year are the same.

6.4 Measuring Ion Temperature

In Section 5.4, we developed a method to investigate the shock heating process and measure $\beta_0 \equiv T_e/T_p$ at the shock transition. To enhance the reliability of this approach, it is beneficial to compare the temperature variabilities of electrons with those of protons and other ions, which should have a relation depicted in Figure 1.4. Since Hα emission occurs immediately behind the shock, we can measure the proton temperature before being influenced by Coulomb collisions using the Hα line width broadened by thermal fluctuations. Proton temperature has been successfully measured in the east rim of Tycho's SNR through Hα observations (Ghavamian et al., 2000). By conducting a similar observation in Knot1, we can compare the proton temperature in Knot1 with the electron temperature change measured in this thesis.

Measuring the temperatures of other ions poses a challenge with currently active X-ray telescopes due to their limited energy resolution. The high-resolution spectroscopy provided by the recently launched XRISM telescope can overcome this difficulty. The Resolve instrument onboard XRISM has superior energy resolution of $\sim$ 7 eV FWHM @ 6 keV (XRISM Science Team, 2020), enabling the measurement of ion temperatures from emission lines. Meanwhile, analyzing small spatial features like Knot1 is impractical, given the Resolve angular resolution of $\sim$ 1.′7, which is not as high as that of Chandra. The ion temperature of this feature would be revealed with future missions of X-ray observatories with high resolution of angle and energy like HUBS (Bregman et al., 2023) and Lynx (Gaskin et al., 2018).

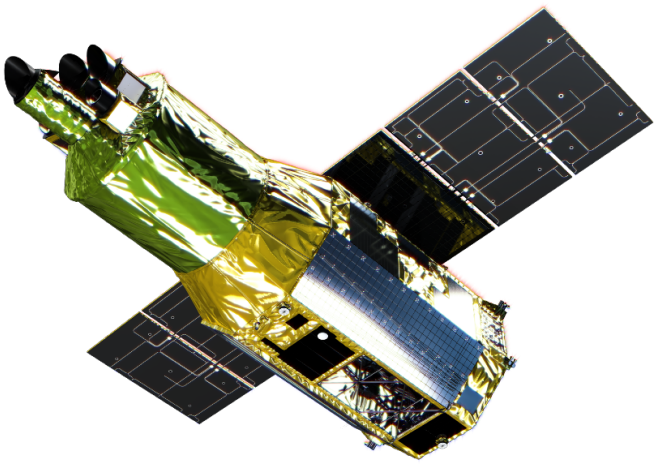

Parameter	Requirement	Hitomi Values
Energy resolution	7 eV (FWHM)	5.0 eV
Energy scale accuracy	± 2 eV	± 0.5 eV
Residual Background	2 x 10^{-3} counts/s/keV	0.8 x 10^{-3} counts/s/keV
Field of view	2.9 x 2.9 arcmin	same, by design
Angular resolution	1.7 arcmin (HPD)	1.2 arcmin
Effective area (1 keV)	> 160 cm^2	250 cm^2
Effective area (6 keV)	> 210 cm^2	312 cm^2
Cryogen-mode Lifetime	3 years	4.2 years (projected)
Operational Efficiency	> 90%	> 98%

Figure 6.9: The overview of XRISM and its pre-launch requirements (XRISM Science Team, 2020).

If the plasma is distributed over a larger spatial scale than the Resolve angular resolution, the Resolve can extract X-rays from shocked ISM plasma. To investigate the thermalized ISM distribution in Tycho's SNR, we focus on an analytical technique, the general morphological component analysis (GMCA), introduced by Picquenot et al. (2019). GMCA categorizes the observed data into distinct groups without losing the multidimensional (position and energy) information. Consequently, we can obtain some groups with different morphologies and spectral signatures, such as thermalized ejecta and nonthermal radiation. Yamaguchi et al. (2021) used GMCA in the analysis of N103B, retrieving three components interpreted as having origins of the CSM, the Fe-rich ejecta, and IME ejecta origins (Figure 6.10).

GMCA enables us to understand distributions of X-ray components even when their contribution is relatively low, potentially serving as an indicator to search for thermal X-rays from ISM in Tycho's SNR. Applying GMCA to Tycho's SNR, we successfully identify an X-ray component that spatially correlates with the distribution of the Hα line, suggesting X-rays originating from thermalized ISM/CSM. As can be seen in Figure 6.11, the Hα counterpart component the Hα counterpart component appears relatively bright not only in Knot1 but also in the east and northwest regions, indicating the potential to

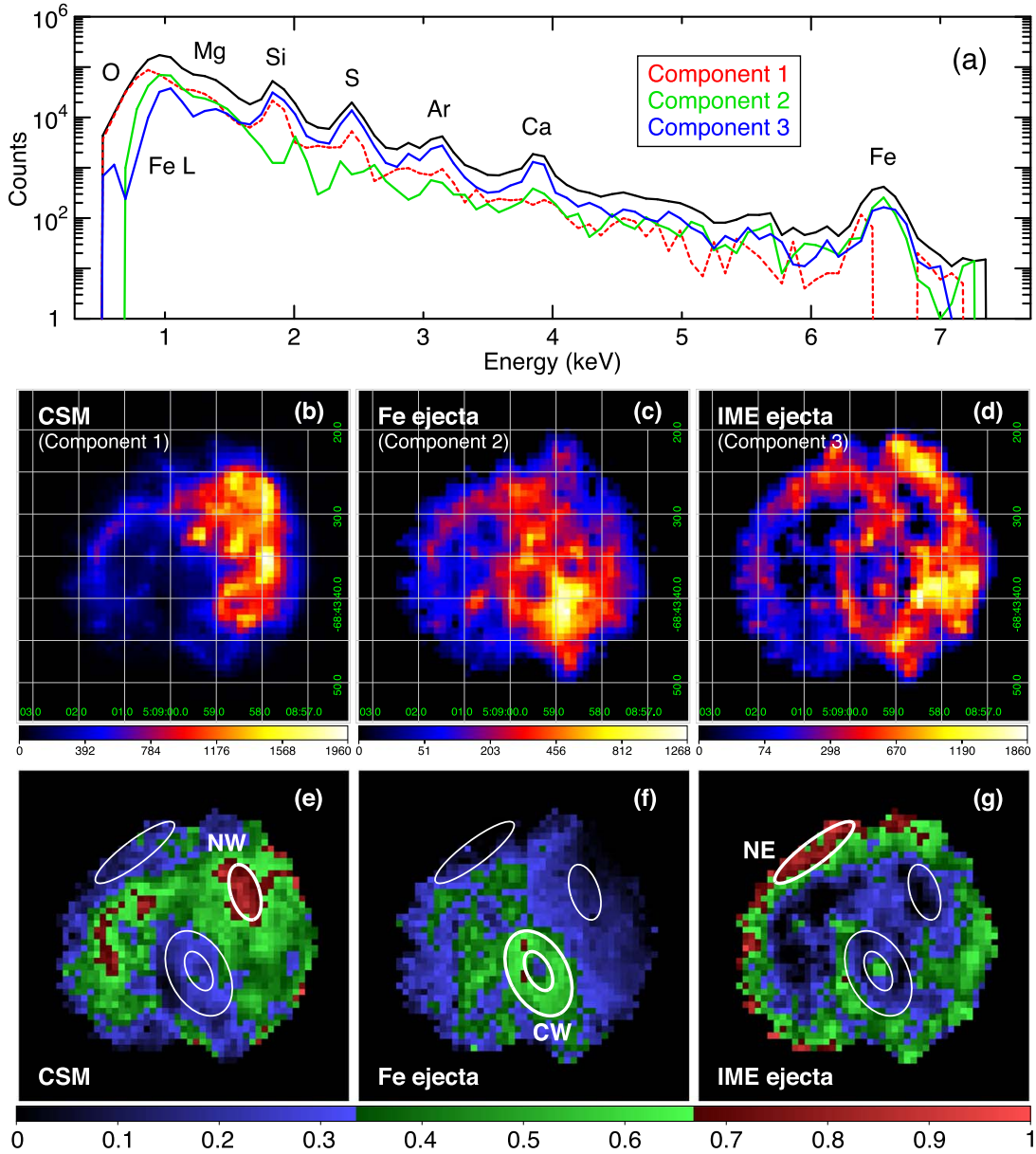

Figure 6.10: An example of the GMCA result applied to SNR N103B Yamaguchi et al. (2021). The top and middle panels show spectra and images of the separated components, respectively. The bottom panel shows the fraction of each component. The white ellipses show the regions that they used for spectral extractions.

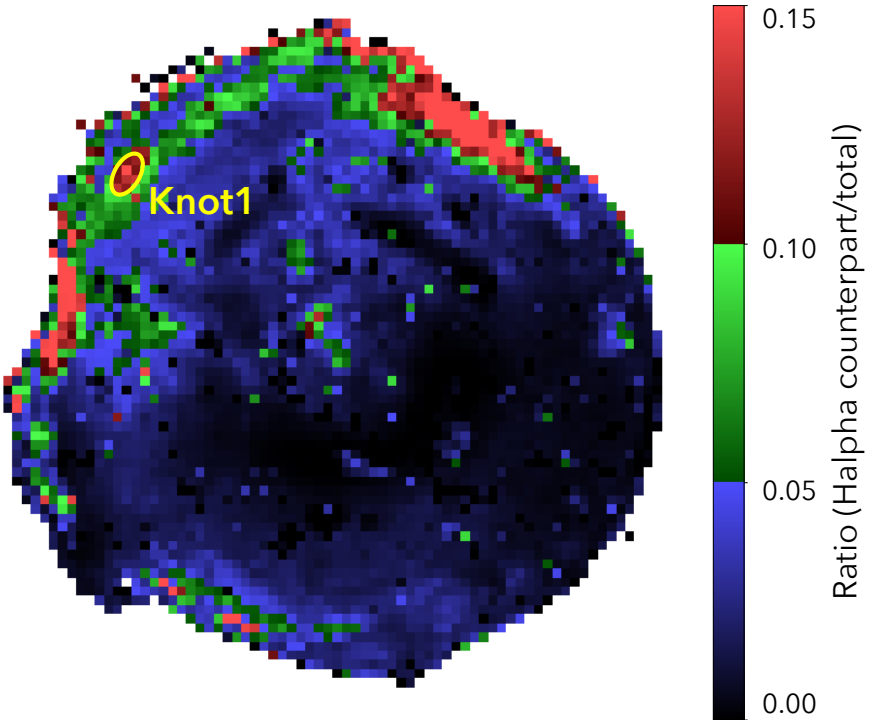

Figure 6.11: The ratio image made by separating counts of the Hα counterpart component and the total counts. The yellow ellipse represents the region of Knot1.

analyze X-rays from shocked ISM or CSM in these areas, even though their counts constitute only about 15% of the total counts.

To confirm that Resolve can detect the ISM component, we simulate the spectra of Tycho's SNR, comprising thermalized ejecta emission and thermalized ISM emission, with the latter having 10% of the flux of the ejecta component, as illustrated in Figure 6.12. The simulation suggests that we can retrieve the ISM component from the spectra. The prominent emission lines from O VII ($\simeq$ 0.654 keV) and Ne IX ($\simeq$ 0.922 keV) indicate the potential to measure the ion temperature of oxygen and neon, respectively, with the line width of thermal broadening. The simulation suggests that we can retrieve the ISM component from the spectra. The prominent emission lines from O VII ($\simeq$ 0.654 keV) and Ne IX ($\simeq$ 0.922 keV) suggest the potential to measure the ion temperature of oxygen and neon with the line width of thermal broadening. As shown in Figure1.4, the ion temperatures of oxygen and neon decrease from $\simeq$ 30 keV to $\simeq$ 10 keV over a timescale of $n_e t \simeq 10^{10}$ cm^{-3} s. This timescale corresponds to approximately ten years when the electron density n_e is 50 cm^{-3}. Consequently, if XRISM observes Tycho's SNR several times over a few decades, we could measure the time variability of ion temperature, revealing the temperature changes of electrons and ions behind the shock through energy transfer. Furthermore, high-resolution spectroscopy will unveil the composition of the ISM component, providing insights into the origin of the wall investigated in Chapter 6.2.

The measurement of ion temperature can also be applied to other SNRs with bright X-rays from shocked ISM or CSM. Miceli et al. (2015) indeed measured the ion temperature

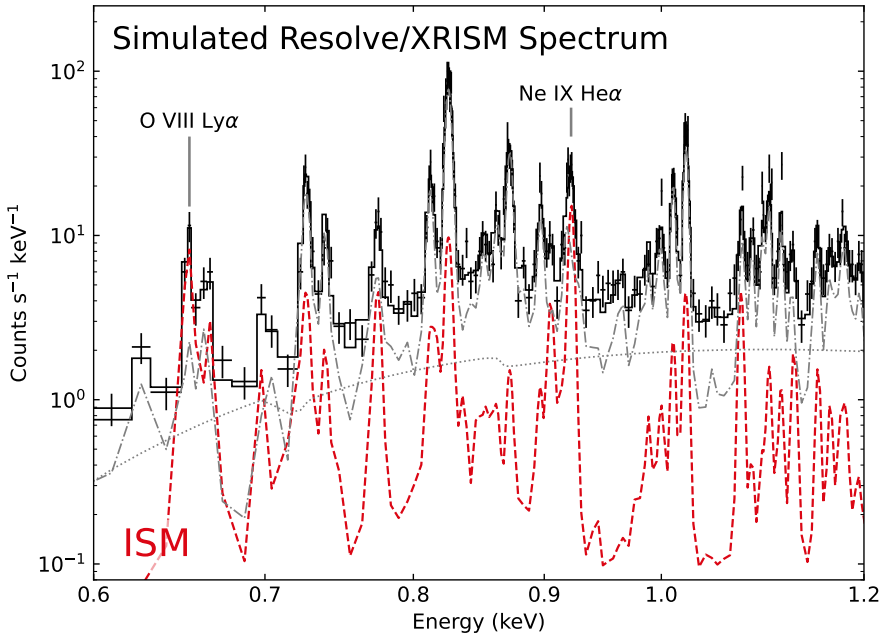

Figure 6.12: Simulated XRISM spectrum of Tycho's SNR. The dashed red curve is a component from thermalized ISM whose flux in 0.5–1.0 keV is assumed to be 10% of ejecta. The dash-dotted and dotted curves in grey are the ejecta and power-law components, respectively.

of certain ion species in post-shock plasma. By measuring the ion temperature of SNRs with different ages, we can track temperature changes in a still longer timescale until the post-shock plasma reaches thermal equilibrium between electrons and ions.

7

Conclusions

We discovered the year-scale variabilities of X-ray fluxes and the expansions of Tycho's SNR with Chandra, aiming to understand the energy transfers between shock waves and particles and the shock–cloud interaction. We outline the important results below:

1. We investigated time variabilities in X-rays within the western "stripe" structure of Tycho's SNR using Chandra images from 2003, 2007, 2009, and 2015. The flux difference image unveiled time variabilities in synchrotron emission along each stripe, including faint ones. Our spatially resolved spectroscopy also detected significant time variabilities in photon indices and brightness of synchrotron radiation from most stripes. Assuming that the flux increased and decreased due to the increase in averaged electron energy through DSA and their decrease through synchrotron cooling, respectively, we concluded that the magnetic field is required to be amplified to $\sim$ 500 μG to account for the observed variability timescale. A comparison of synchrotron emission between the stripe and rim revealed harder spectra for the stripe (Γ = 2.1–2.6) than the rim (Γ = 2.7–2.9), indicating amplified magnetic fields or stochastic acceleration far downstream of the shock. The discovery of a tight anti-correlation between brightness and photon index was also noteworthy, suggesting that a small number of parameters are related to the spatial and temporal variability of the stripe. Our results indicate the possibility of an effective acceleration far downstream of the shock.

2. We applied a time variability analysis to the thermal emission of Tycho's SNR, aiming to understand the processes involved in electron heating within SNR plasma. By examining thermal X-ray time variabilities using Chandra data from 2000, 2003, 2007, 2009, and 2015, we identified a significant brightening in a knot-like feature (Knot1) in the northeast region of the remnant. Our X-ray spectral analysis, combined with the distribution of the Hα line, revealed that Knot1 originated from thermalized ISM/CSM by the forward shock, with a density of $n_{\rm H} \sim 30$ cm^{-3}. Our

spectral analysis firstly detected a significant increase in electron temperature from $0.30^{+0.05}_{-0.07}$ keV to $0.69^{+0.16}_{-0.12}$ keV over the 15-year period. These findings suggest that the brightening is attributed to electron heating through Coulomb collisions following an encounter of the forward shock with dense clumps around 2000. The calculated evolution of electron temperatures required the electron-to-proton temperature ratio immediately behind the shock ($\beta_0 \equiv T_e/T_p$) to be $m_e/m_p \leq \beta_0 \leq 0.05$, assuming a shock velocity of 1500 km s^{-1}. We introduced a new method to detect the thermal emission from shock-heated gas and measure β_0 independently of the previous estimation using Hα lines.

3. Our analysis of the flux change in Tycho's SNR suggests the interaction between shock and clouds surrounding the remnant. To investigate the surrounding environment in another way, we measured the proper motion of the shock waves using newly observed data from 2022–2023 with Chandra added to data analyzed by Tanaka et al. (2021). Our result reveals further deceleration in the western shell from 2015 to 2021 beyond the velocity in 2003–2015 measured by Tanaka et al. (2021). It supports the existence of the wall formed by the wind from a progenitor white dwarf during mass accretion. We conducted a spectral analysis of synchrotron radiation from the shock front to study the effect of the shock–wall interaction on it. Although we could not observe significant changes in the X-ray spectra, we discovered softening trends in some regions. The result implies a decrease in cutoff energy due to the decrease in shock velocity.

4. We proposed extending the observation of X-ray time variabilities to other SNRs. Initially, we verified the application to Kepler's SNR, which is similar in age, distance, and explosion type to Tycho's SNR. Flux difference images of Kepler's SNR show a flux brightening of thermal X-ray over large areas that spatially coincide with an Hα image. Extracted X-ray spectra also suggest an increase in flux in low-energy band $\leq$ 1 keV from 2006 to 2014. Examining such time variability in thermal X-rays would enable us to investigate the dependence of β_0 on the environment, including factors like the ambient magnetic field.

5. We found an indication of thermalized ISM plasma extending across a wide area in the northeast of Tycho's SNR using the General Morphological Component Analysis (GMCA) method. GMCA is an analytical technique that categorizes the observed data into some groups based on spatial and spectral information jointly (Picquenot et al., 2019). While the X-ray radiation from the plasma is likely to account for at most 15% of the total flux, the high-resolution spectroscopy with the XRISM telescope would allow us to resolve it. It could reveal the time variabilities of ion temperatures, offering insights into the energy transfer between electrons and ions behind the shock.

Appendices

A

Time Evolution of Electron Temperature with Low Shock Velocities

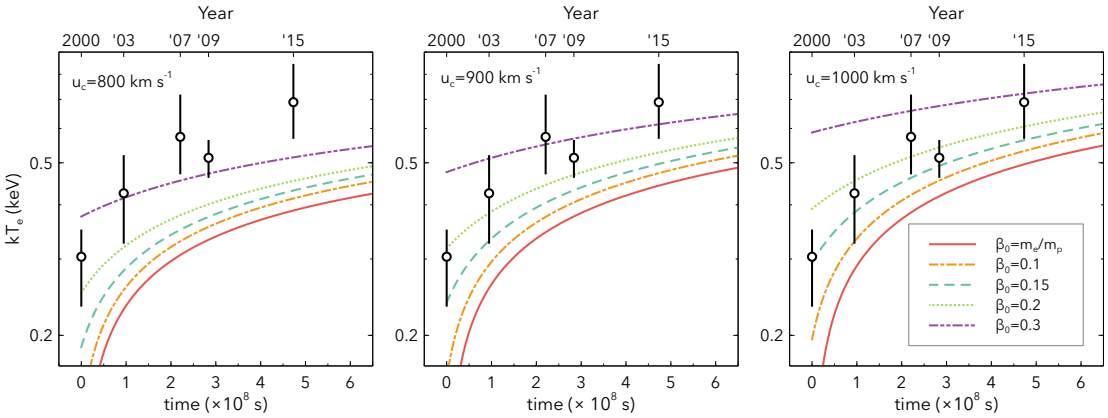

Figure A.1: Compatrison between electron temperature change in Knot1 and calculations under assumptions of $u_c = 800$ (left), 900 (middle), and 1000 (right). The solid, dashed-dot, dashed, dotted, and dash-dot-dotted curves show results when $\beta = m_e/m_p$, 0.1, 0.15, 0.2, and 0.3, respectively.

We calculate the time evolution of electron temperature under the assumption of lower shock velocities than those discussed in Section 5.4.2.2 since the trend of the kT_e observed in Section 5.4 may indicate it. The time variations of kT_e in the case of $u_c \leq 1000$ km s^{-1} is shown in Figure A.1. The slower the shock velocity is, the longer time it takes for the electron temperature to increase from ~ 0.5 keV to ~ 0.7 keV. The observed kT_e is roughly explained in the case of $\beta_0 \simeq 0.15$ when u_c is 1000 km s^{-1} while it cannot be explained in any case of β_0 when u_c is lower.

Figure A.2 shows the temperature evolution under the different assumptions of $t = 0$ for $u_c = 1000$ km s^{-1}. In these case, the case of $m_e/m_p \lesssim \beta_0 \lesssim 0.15$ is reasonable to explain the observed data. In summary, the observed kT_e change can be also

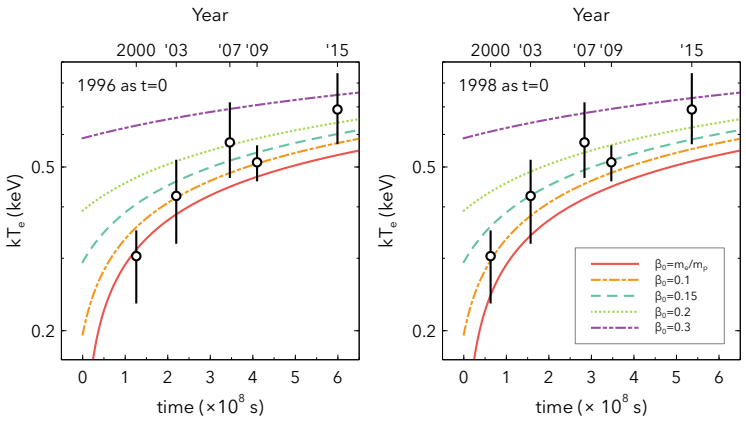

Figure A.2: Same as Figure A.1, but the time in which the shock heating was started is assumed to be 1996 (left) and 1999 (right).

roughly explain $m_e/m_p \lesssim \beta_0 \lesssim 0.15$ for $u_c = 1000$ km s^{-1} in addition to the case of $u_c \geq 1500$ km s^{-1} discussed in Section 5.4. If u_c is indeed slower, it implies a larger density contrast χ or a slower forward-shock velocity u_i. Future observations with better statistics or high-resolution imaging should constrain these parameters.

Estimation of β_0 by Hα lines got greater value than 0.1 in SNRs with slow shocks ($v_{sh} \leq 1000$ km s^{-1}) such as Cygnus Loop, RCW 86 (Ghavamian et al., 2001), and SNR 0548−70.4 (Smith et al., 1991). Thus, we note that it can be consistent with Hα observations even if the shock velocity is lower.

References

Abbott, B. P., R. Abbott, T. D. Abbott, F. Acernese, K. Ackley, et al. (2017). "GW170817: Observation of Gravitational Waves from a Binary Neutron Star Inspiral". *Phys. Rev. Lett.* **119**, 161101. DOI: 10.1103/PhysRevLett.119.161101.

Acero, Fabio, Satoru Katsuda, Jean Ballet & Robert Petre (2017). "Measurement of the X-ray Proper Motion in the South-East Rim of RX J1713.7–3946". *A&A* **597**, A106. DOI: 10.1051/0004-6361/201629618.

Ackermann, M., M. Ajello, A. Allafort, L. Baldini, J. Ballet, et al. (2013). "Detection of the Characteristic Pion-Decay Signature in Supernova Remnants". *Science* **339**, 807–811. DOI: 10.1126/science.1231160.

Alekseev, E. N., L. N. Alekseeva, I. V. Krivosheina & V. I. Volchenko (1987). "Detection of the Neutrino Signal from Supernova 1987A Using the INR Baksan Underground Scintillation Telescope". **26**, 237.

Arenberg, Jonathan, Gary Matthews, C. Atkinson, L. Cohen, C. Golisano, et al. (2014). "Lessons We Learned Designing and Building the Chandra Telescope". In: *Space Telesc. Instrum. 2014 Ultrav. Gamma Ray*. Space Telescopes and Instrumentation 2014: Ultraviolet to Gamma Ray. **9144**. SPIE, 238–254. DOI: 10.1117/12.2055515.

Arnaud, K. A. (1996). *XSPEC: The First Ten Years*, p. 17.

Arnett, W. David (1969). "A Possible Model of Supernovae: Detonation of 12C". *Astrophys. Space Sci.* **5**, 180–212. DOI: 10.1007/BF00650291.

Aschenbach, Bernd (2002). "In-Orbit Performance of the XMM-Newton x-Ray Telescopes: Images and Spectra". In: International Symposium on Optical Science and Technology. Ed. by Paul Gorenstein & Richard B. Hoover. San Diego, CA, USA, 8. DOI: 10.1117/12.454367.

Axford, W. I., E. Leer & G. Skadron (1977). "The Acceleration of Cosmic Rays by Shock Waves". In: International Cosmic Ray Conference. **11**, 132.

Baade, W. (1945). "B Cassiopeiae as a Supernova of Type I." *The Astrophysical Journal* **102**, 309. DOI: 10.1086/144761.

Baade, W. & F. Zwicky (1934). "Cosmic Rays from Super-novae". *Proc. Natl. Acad. Sci.* **20**, 259–263. DOI: 10.1073/pnas.20.5.259.

Banovetz, John, Dan Milisavljevic, Niharika Sravan, Robert A. Fesen, Daniel J. Patnaude, et al. (2021). "The Center of Expansion and Age of the Oxygen-rich Supernova Remnant 1E 0102.2–7219". *ApJ* **912**, 33. DOI: 10.3847/1538-4357/abe2a7.

Bell, A. R. (1978a). "The Acceleration of Cosmic Rays in Shock Fronts - I." *MNRAS* **182**, 147–156. DOI: 10.1093/mnras/182.2.147.

— (1978b). "The Acceleration of Cosmic Rays in Shock Fronts - II." *MNRAS* **182**, 443–455. DOI: 10.1093/mnras/182.3.443.

— (2004). "Turbulent Amplification of Magnetic Field and Diffusive Shock Acceleration of Cosmic Rays". *Mon Not R Astron Soc* **353**, 550–558. DOI: 10.1111/j.1365-2966.2004.08097.x.

Blandford, Roger & David Eichler (1987). "Particle Acceleration at Astrophysical Shocks: A Theory of Cosmic Ray Origin". *Phys. Rep.* **154**, 1–75. DOI: 10.1016/0370-1573(87)90134-7.

Bohdan, Artem (2023). “Electron Acceleration in Supernova Remnants”. *Plasma Phys. Control. Fusion* **65**, 014002. DOI: 10.1088/1361-6587/aca5b2.

Borkowski, Kazimierz J., Peter Gwynne, Stephen P. Reynolds, David A. Green, Una Hwang, Robert Petre & Rebecca Willett (2017). “Asymmetric Expansion of the Youngest Galactic Supernova Remnant G1.9+0.3”. *ApJ* **837**, L7. DOI: 10.3847/2041-8213/aa618c.

Borkowski, Kazimierz J., Stephen P. Reynolds, Brian J. Williams & Robert Petre (2018). “Expansion and Age of the X-Ray Synchrotron-dominated Supernova Remnant G330.2+1.0”. *ApJL* **868**, L21. DOI: 10.3847/2041-8213/aaedb5.

Bregman, Joel, Renyue Cen, Yang Chen, Wei Cui, Taotao Fang, et al. (2023). “Scientific Objectives of the Hot Universe Baryon Surveyor (HUBS) Mission”. *Sci. China Phys. Mech. Astron.* **66**, 299513. DOI: 10.1007/s11433-023-2149-y.

Brejnholt, Nicolai F., Finn E. Christensen, Niels J. Westergaard, Charles J. Hailey, Jason E. Koglin & William W. Craig (2012). “NuSTAR On-Ground Calibration: II. Effective Area”. In: SPIE Astronomical Telescopes + Instrumentation. **8443**. Amsterdam, Netherlands, 84431Y. DOI: 10.1117/12.925631.

Brussaard, P. J. & H. C. van de Hulst (1962). “Approximation Formulas for Nonrelativistic Bremsstrahlung and Average Gaunt Factors for a Maxwellian Electron Gas”. *Rev. Mod. Phys.* **34**, 507–520. DOI: 10.1103/RevModPhys.34.507.

Burrows, David N., Eli Michael, Una Hwang, Richard McCray, Roger A. Chevalier, et al. (2000). “The X-Ray Remnant of SN 1987A”. *Astrophys. J.* **543**, L149–L152. DOI: 10.1086/317271.

Bykov, A. M., S. M. Osipov & D. C. Ellison (2011). “Cosmic Ray Current Driven Turbulence in Shocks with Efficient Particle Acceleration: The Oblique, Long-Wavelength Mode Instability”. *Mon Not R Astron Soc* **410**, 39–52. DOI: 10.1111/j.1365-2966.2010.17421.x.

Caprioli, D. & A. Spitkovsky (2013). “Cosmic-Ray-induced Filamentation Instability in Collisionless Shocks”. *ApJL* **765**, L20. DOI: 10.1088/2041-8205/765/1/L20.

— (2014). “Simulations of Ion Acceleration at Non-relativistic Shocks. II. Magnetic Field Amplification”. *The Astrophysical Journal* **794**, 46. DOI: 10.1088/0004-637X/794/1/46.

Cargill, P. J. & K. Papadopoulos (1988). “A Mechanism for Strong Shock Electron Heating in Supernova Remnants”. *ApJL* **329**, L29–L32. DOI: 10.1086/185170.

Cassam-Chenaï, Gamil, John P. Hughes, Jean Ballet & Anne Decourchelle (2007). “The Blast Wave of Tycho’s Supernova Remnant”. *ApJ* **665**, 315. DOI: 10.1086/518782.

Chandra X-ray Center (2022). *Proposers’ Observatory Guide*. URL: https://cxc.harvard.edu/proposer/POG/html/ (visited on 07/04/2023).

— (2023a). *ACIS: Advanced CCD Imaging Spectrometer*. URL: https://cxc.harvard.edu/proposer/POG/html/chap6.html (visited on 02/05/2024).

— (2023b). *Tracking Chandra*. URL: https://chandra.harvard.edu/about/tracking.html (visited on 06/29/2023).

Chevalier, Roger A. (1974). “The Evolution of Supernova Remnants. Spherically Symmetric Models”. *ApJ* **188**, 501–516. DOI: 10.1086/152740.

Cioffi, Denis F., Christopher F. McKee & Edmund Bertschinger (1988). “Dynamics of Radiative Supernova Remnants”. *ApJ* **334**, 252. DOI: 10.1086/166834.

Deaconu, Cosmin (2008). *The Supernova Problem*. URL: http://large.stanford.edu/courses/2008/ph204/deaconu1/ (visited on 11/12/2023).

Drury, L. O’C (1983). “An Introduction to the Theory of Diffusive Shock Acceleration of Energetic Particles in Tenuous Plasmas”. *Rep. Prog. Phys.* **46**, 973. DOI: 10.1088/0034-4885/46/8/002.

Elias, J. H., K. Matthews, G. Neugebauer & S. E. Persson (1985). "Type I Supernovae in the Infrared and Their Use as Distance Indicators." *ApJ* **296**, 379–389. DOI: 10.1086/163456.

Enoto, Teruaki, Toshio Terasawa, Shota Kisaka, Chin-Ping Hu, Sebastien Guillot, et al. (2021). "Enhanced X-Ray Emission Coinciding with Giant Radio Pulses from the Crab Pulsar". *Sci. Vol. 372 Issue 6538 Pp 187-190 2021* **372**, 187. DOI: 10.1126/science.abd4659.

Eriksen, Kristoffer A., John P. Hughes, Carles Badenes, Robert Fesen, Parviz Ghavamian, et al. (2011). "Evidence for Particle Acceleration to the Knee of the Cosmic Ray Spectrum in Tycho's Supernova Remnant". *ApJL* **728**, L28. DOI: 10.1088/2041-8205/728/2/L28.

Evoli, Carmelo (2020). *The Cosmic-Ray Energy Spectrum*. Zenodo. DOI: 10.5281/zenodo.7948212.

Fesen, Robert A., Robert H. Becker, William P. Blair & Knox S. Long (1989). "High-Velocity, Nonradiative Shock Emission in Kepler's Supernova Remnant". *AJ* **338**, L13. DOI: 10.1086/185389.

Fleisher, R. L., P. B. Price & R. M. Walker (1975). *Nuclear Tracks in Solids: Principles and Applications*.

Foley, Ryan J., O. D. Fox, C. McCully, M. M. Phillips, D. J. Sand, et al. (2014). "Extensive HST Ultraviolet Spectra and Multiwavelength Observations of SN 2014J in M82 Indicate Reddening and Circumstellar Scattering by Typical Dust". *Mon. Not. R. Astron. Soc.* **443**, 2887–2906. DOI: 10.1093/mnras/stu1378.

Foster, Adam R., Randall K. Smith & Nancy S. Brickhouse (2017). "Data for Non Equilibrium Modeling with AtomDB". In: *At. Process. Plasmas APiP 2016*. **1811**. American Institute of Physics Conference Series, 190005, 190005. DOI: 10.1063/1.4975748.

Garmire, Gordon P., Mark W. Bautz, Peter G. Ford, John A. Nousek & George R. Ricker Jr (2003). "Advanced CCD Imaging Spectrometer (ACIS) Instrument on the Chandra X-ray Observatory". In: *X-Ray Gamma-Ray Telesc. Instrum. Astron.* X-Ray and Gamma-Ray Telescopes and Instruments for Astronomy. **4851**. SPIE, 28–44. DOI: 10.1117/12.461599.

Garnavich, Peter M., Saurabh Jha, Peter Challis, Alejandro Clocchiatti, Alan Diercks, et al. (1998). "Supernova Limits on the Cosmic Equation of State". *Astrophys. J.* **509**, 74–79. DOI: 10.1086/306495.

Gaskin, Jessica A., Alexandra Dominguez, Karen Gelmis, John (Jack) Mulqueen, Douglas Swartz, et al. (2018). "The Lynx X-ray Observatory: Concept Study Overview and Status". **10699**, 106990N. DOI: 10.1117/12.2314149.

Ghavamian, Parviz, J. Martin Laming & Cara E. Rakowski (2007). "A Physical Relationship between Electron-Proton Temperature Equilibration and Mach Number in Fast Collisionless Shocks". *ApJL* **654**, L69–L72. DOI: 10.1086/510740.

Ghavamian, Parviz, John Raymond, Patrick Hartigan & William P. Blair (2000). "Evidence for Shock Precursors in Tycho's Supernova Remnant". *ApJ* **535**, 266–274. DOI: 10.1086/308811.

Ghavamian, Parviz, John Raymond, R. Chris Smith & Patrick Hartigan (2001). "Balmer-Dominated Spectra of Nonradiative Shocks in the Cygnus Loop, RCW 86, and Tycho Supernova Remnants". *ApJ* **547**, 995–1009. DOI: 10.1086/318408.

Ghavamian, Parviz, P. Frank Winkler, John C. Raymond & Knox S. Long (2002). "The Optical Spectrum of the SN 1006 Supernova Remnant Revisited". *ApJ* **572**, 888–896. DOI: 10.1086/340437.

Ginzburg, V. L. & S. I. Syrovatskii (1965). "Cosmic Magnetobremsstrahlung (Synchrotron Radiation)". *Annu. Rev. Astron. Astrophys.* **3**, 297–350. DOI: 10.1146/annurev.aa.03.090165.001501.

Grefenstette, Brian W., Murray Brightman, Hannah P. Earnshaw, Fiona A. Harrison & R. Margutti (2023). "Early Hard X-Rays from the Nearby Core-collapse Supernova SN 2023ixf". *Astrophys. J.* **952**, L3. DOI: 10.3847/2041-8213/acdf4e.

Gu, L., C. Shah, J. Mao, A. J. J. Raassen, J. de Plaa, et al. (2022). "X-Ray Spectra of the Fe-L Complex. III. Systematic Uncertainties in Atomic Data". *Astron. Astrophys.* **664**, A62. DOI: 10.1051/0004-6361/202039943.

Guest, Benson T., Kazimierz J. Borkowski, Parviz Ghavamian, Robert Petre, Adrien Picquenot, Stephen P. Reynolds, Ivo R. Seitenzahl & Brian J. Williams (2023). "Rapid Expansion of the Young Type Ia Supernova Remnant 0519-69.0: More Evidence for a Circumstellar Shell". *Astrophys. J.* **946**, 44. DOI: 10.3847/1538-4357/acbf4e.

Guest, Benson T., Kazimierz J. Borkowski, Parviz Ghavamian, Robert Petre, Stephen P. Reynolds, Ivo R. Seitenzahl & Brian J. Williams (2022). "An X-Ray Proper-motion Study of the Large Magellanic Cloud Supernova Remnant 0509-67.5". *Astron. J.* **164**, 231. DOI: 10.3847/1538-3881/ac9792.

Haines, Todd, C. B. Bratton, D. Casper, A. Ciocio, R. Claus, et al. (1988). "Neutrinos from SN1987a in the IMB Detector". *Nuclear Instruments and Methods in Physics Research Section A: Accelerators, Spectrometers, Detectors and Associated Equipment* **264**, 28–31. DOI: 10.1016/0168-9002(88)91097-2.

Harrison, Fiona A., William W. Craig, Finn E. Christensen, Charles J. Hailey, William W. Zhang, et al. (2013). "The Nuclear Spectroscopic Telescope Array (NuSTAR) High-energy X-Ray Mission". *ApJ* **770**, 103. DOI: 10.1088/0004-637X/770/2/103.

Helder, E. A., D. Kosenko & J. Vink (2010). "Cosmic-Ray Acceleration Efficiency versus Temperature Equilibration: The Case of SNR 0509-67.5". *The Astrophysical Journal Letters* **719**, L140–L144. DOI: 10.1088/2041-8205/719/2/L140.

Hess, Victor F. (1912). "Über Beobachtungen Der Durchdringenden Strahlung Bei Sieben Freiballonfahrten". *Phys. Z.* **13**, 1084–1091.

Hirata, K., T. Kajita, M. Koshiba, M. Nakahata, Y. Oyama, et al. (1987). "Observation of a Neutrino Burst from the Supernova SN1987A". *Phys. Rev. Lett.* **58**, 1490–1493. DOI: 10.1103/PhysRevLett.58.1490.

Hovey, Luke, John P. Hughes & Kristoffer Eriksen (2015). "A Direct Measurement of the Forward Shock Speed in Supernova Remnant 0509-67.5: Constraints on the Age, Ambient Density, Shock Compression Factor, and Electron-ion Temperature Equilibration". *Astrophys. J.* **809**, 119. DOI: 10.1088/0004-637X/809/2/119.

Hugoniot, Pierre Henri (1887). "Mémoire Sur La Propagation Des Mouvements Dans Les Corps et Spécialement Dans Les Gaz Parfaits (Première Partie)". *J. École Polytech.* **57**, 3–97.

— (1889). "Mémoire Sur La Propagation Des Mouvements Dans Les Corps et Spécialement Dans Les Gaz Parfaits (Deuxième Partie)". *J. École Polytech.* **58**, 1–125.

Hwang, Una, Anne Decourchelle, Stephen S. Holt & Robert Petre (2002). "Thermal and Nonthermal X-Ray Emission from the Forward Shock in Tycho's Supernova Remnant". *ApJ* **581**, 1101–1115. DOI: 10.1086/344366.

Iben Jr., I. & A. V. Tutukov (1984). "Supernovae of Type I as End Products of the Evolution of Binaries with Components of Moderate Initial Mass." *Astrophys. J. Suppl. Ser.* **54**, 335–372. DOI: 10.1086/190932.

Inoue, Tsuyoshi, Ryo Yamazaki, Shu-ichiro Inutsuka & Yasuo Fukui (2012). "Toward Understanding the Cosmic-Ray Acceleration at Young Supernova Remnants Interacting

with Interstellar Clouds: Possible Applications to RX J1713.7-3946". *Astrophys. J.* **744**, 71. DOI: 10.1088/0004-637X/744/1/71.

Ishihara, D., H. Kaneda, A. Furuzawa, H. Kunieda, T. Suzuki, et al. (2010). "Origin of the Dust Emission from Tycho's SNR". *Astronomy and Astrophysics* **521**, L61. DOI: 10.1051/0004-6361/201015131.

Jacobson-Galán, W. V., L. Dessart, R. Margutti, R. Chornock, R. J. Foley, et al. (2023). "SN 2023ixf in Messier 101: Photo-ionization of Dense, Close-in Circumstellar Material in a Nearby Type II Supernova". *Astrophys. J.* **954**, L42. DOI: 10.3847/2041-8213/acf2ec.

Jansen, F., D. Lumb, B. Altieri, J. Clavel, M. Ehle, et al. (2001). "XMM-Newton Observatory. I. The Spacecraft and Operations". *A&A* **365**, L1–L6. DOI: 10.1051/0004-6361:20000036.

Kaastra, J. S., R. Mewe & H. Nieuwenhuijzen (1996). *SPEX: A New Code for Spectral Analysis of X & UV Spectra*. Pp. 411–414.

Kasuga, Tomoaki, Jacco Vink, Satoru Katsuda, Hiroyuki Uchida, Aya Bamba, Toshiki Sato & John P Hughes (2021). "Spatially Resolved RGS Analysis of Kepler's Supernova Remnant". *Astrophys. J.* **915**, 42. DOI: 10.3847/1538-4357/abff4f.

Katsuda, Satoru (2023). "High-Resolution X-Ray Spectroscopy of Supernova Remnants". In: *High-Resolution X-ray Spectroscopy: Instrumentation, Data Analysis, and Science*. Ed. by Cosimo Bambi & Jiachen Jiang. Springer Series in Astrophysics and Cosmology. Singapore: Springer Nature, pp. 393–425. DOI: 10.1007/978-981-99-4409-5_13.

Katsuda, Satoru, Knox S. Long, Robert Petre, Stephen P. Reynolds, Brian J. Williams & P. Frank Winkler (2013). "X-Ray Proper Motions and Shock Speeds along the Northwest Rim of SN 1006". *Astrophys. J.* **763**, 85. DOI: 10.1088/0004-637X/763/2/85.

Katsuda, Satoru, Koji Mori, Keiichi Maeda, Masaomi Tanaka, Katsuji Koyama, et al. (2015). "Keplers Supernova: An Overluminous Type Ia Event Interacting with a Massive Circumstellar Medium at a Very Late Phase". DOI: 10.1088/0004-637X/808/1/49.

Katsuda, Satoru, Mikio Morii, Hans-Thomas Janka, Annop Wongwathanarat, Ko Nakamura, et al. (2018). "Intermediate-Mass Elements in Young Supernova Remnants Reveal Neutron Star Kicks by Asymmetric Explosions". *ApJ* **856**, 18. DOI: 10.3847/1538-4357/aab092.

Katsuda, Satoru, Robert Petre, John P. Hughes, Una Hwang, Hiroya Yamaguchi, Asami Hayato, Koji Mori & Hiroshi Tsunemi (2010). "X-Ray Measured Dynamics of Tycho's Supernova Remnant". *The Astrophysical Journal* **709**, 1387–1395. DOI: 10.1088/0004-637X/709/2/1387.

Katsuda, Satoru, H. Tsunemi & K. Mori (2008a). "The Slow X-Ray Expansion of the Northwestern Rim of the Supernova Remnant RX J0852.0-4622". *Astrophys. J.* **678**, L35. DOI: 10.1086/588499.

Katsuda, Satoru, Hiroshi Tsunemi, Hiroyuki Uchida & M. Kimura (2008b). "Forward Shock Proper Motions of Kepler's Supernova Remnant". *ApJ* **689**, 225–230. DOI: 10.1086/592376.

Kerzendorf, Wolfgang E., Michael Childress, Julia Scharwächter, Tuan Do & Brian P. Schmidt (2014). "A Reconnaissance of the Possible Donor Stars to the Kepler Supernova". *Astrophys. J.* **782**, 27. DOI: 10.1088/0004-637X/782/1/27.

Kerzendorf, Wolfgang E., Tuan Do, Selma E. de Mink, Ylva Götberg, Dan Milisavljevic, et al. (2019). "No Surviving Non-Compact Stellar Companion to Cassiopeia A". *A&A* **623**, A34. DOI: 10.1051/0004-6361/201732206.

Kinugasa, Kenzo & Hiroshi Tsunemi (1999). "ASCA Observation of Kepler's Supernova Remnant". *Publ. Astron. Soc. Jpn.* **51**, 239–252. DOI: 10.1093/pasj/51.2.239.

Klein, Richard I., Christopher F. McKee & Philip Colella (1994). "On the Hydrodynamic Interaction of Shock Waves with Interstellar Clouds. 1: Nonradiative Shocks in Small Clouds". *ApJ* **420**, 213–236. DOI: 10.1086/173554.

Knežević, Sladjana, Ronald Läsker, Glenn van de Ven, Joan Font, John C. Raymond, et al. (2017). "Balmer Filaments in Tycho's Supernova Remnant: An Interplay between Cosmic-ray and Broad-neutral Precursors". *ApJ* **846**, 167. DOI: 10.3847/1538-4357/aa8323.

Kobashi, Ryosuke, Shiu-Hang Lee, Takaaki Tanaka & Keiichi Maeda (2023). *Exploring the Circumstellar Environment of Tycho's Supernova Remnant–I. The Hydrodynamic Evolution of the Shock*. arXiv e-prints. DOI: 10.48550/arXiv.2310.14841. preprint.

König, Ole, Jörn Wilms, Riccardo Arcodia, Thomas Dauser, Konrad Dennerl, et al. (2022). "X-Ray Detection of a Nova in the Fireball Phase". *Nature* **605** (7909), 248–250. DOI: 10.1038/s41586-022-04635-y.

Koyama, K., K. Kinugasa, K. Matsuzaki, M. Nishiuchi, M. Sugizaki, Ken'ichi Torii, Shigeo Yamauchi & Bernd Aschenbach (1997). "Discovery of Non-Thermal X-Rays from the Northwest Shell of the New SNR RX J1713.7-3946: The Second SN 1006?" *Publ. Astron. Soc. Jpn.* **49**, L7–L11. DOI: 10.1093/pasj/49.3.L7.

Koyama, K., R. Petre, E. V. Gotthelf, U. Hwang, M. Matsuura, M. Ozaki & S. S. Holt (1995). "Evidence for Shock Acceleration of High-Energy Electrons in the Supernova Remnant SN1006". *Nature* **378**, 255–258. DOI: 10.1038/378255a0.

Laming, J. Martin (2000). "Electron Heating at SNR Collisionless Shocks". *ApJS* **127**, 409–413. DOI: 10.1086/313325.

— (2015). "Wave Propagation at Oblique Shocks: How Did Tycho Get Its Stripes?" *Astrophys. J.* **805**, 102. DOI: 10.1088/0004-637X/805/2/102.

Laming, J. Martin, Una Hwang, Parviz Ghavamian & Cara Rakowski (2014). "Electron Heating, Magnetic Field Amplification, and Cosmic-Ray Precursor Length at Supernova Remnant Shocks". *Astrophys. J.* **790**, 11. DOI: 10.1088/0004-637X/790/1/11.

Laming, J. Martin, John C. Raymond, Brendan M. McLaughlin & William P. Blair (1996). "Electron-Ion Equilibration in Nonradiative Shocks Associated with SN 1006". *ApJ* **472**, 267. DOI: 10.1086/178061.

Lee, Jae-Joon, Bon-Chul Koo, John Raymond, Parviz Ghavamian, Tae-Soo Pyo, Akito Tajitsu & Masahiko Hayashi (2007). "Subaru HDS Observations of a Balmer-dominated Shock in Tycho's Supernova Remnant". *ApJL* **659**, L133–L136. DOI: 10.1086/517520.

Lee, Jae-Joon, John C. Raymond, Sangwook Park, William P. Blair, Parviz Ghavamian, P. F. Winkler & Kelly Korreck (2010). "Resolved Shock Structure of the Balmer-dominated Filaments in Tycho's Supernova Remnant: Cosmic-ray Precursor?" *ApJL* **715**, L146–L149. DOI: 10.1088/2041-8205/715/2/L146.

Lee, Shiu-Hang, Donald C. Ellison & Shigehiro Nagataki (2012). "A Generalized Model of Nonlinear Diffusive Shock Acceleration Coupled to an Evolving Supernova Remnant". *Astrophys. J.* **750**, 156. DOI: 10.1088/0004-637X/750/2/156.

Li, Chuan-Jui, Ivo R. Seitenzahl, Ryoko Ishioka, You-Hua Chu, Ashley J. Ruiter & Frédéric P. A. Vogt (2021). "Searching for Surviving Companion in the Young SMC Supernova Remnant 1E 0102.2-7219". *ApJ* **915**, 20. DOI: 10.3847/1538-4357/abf7c5.

Liu, Zheng-Wei, Friedrich K. Röpke & Zhanwen Han (2023). "Type Ia Supernova Explosions in Binary Systems: A Review". *Res. Astron. Astrophys.* **23**, 082001. DOI: 10.1088/1674-4527/acd89e.

Lopez, Laura A., Brian W. Grefenstette, Stephen P. Reynolds, Hongjun An, Steven E. Boggs, et al. (2015). "A Spatially Resolved Study of the Synchrotron Emission and Titanium in Tychos Supernova Remnant Using NuSTAR". *ApJ* **814**, 132. DOI: 10.1088/0004-637X/814/2/132.

Lumb, D. H., G. D. Berthiaume, D. N. Burrows, G. P. Garmire & J. A. Nousek (1991). "Charge Coupled Devices (CCDs) in X-ray Astronomy". *Exp. Astron.* **2**, 179–201. DOI: 10.1007/BF00566685.

Madsen, Kristin, Ryan Hickox, Matteo Bachetti, Daniel Stern, Nis C. Gellert, et al. (2019). "HEX-P: The High-Energy X-ray Probe". **51**, 166.

Malkov, M. A., R. Z. Sagdeev & P. H. Diamond (2012). "Magnetic and Density Spikes in Cosmic-Ray Shock Precursors". *ApJL* **748**, L32. DOI: 10.1088/2041-8205/748/2/L32.

Markevitch, M., F. Govoni, G. Brunetti & D. Jerius (2005). "Bow Shock and Radio Halo in the Merging Cluster A520". *ApJ* **627**, 733–738. DOI: 10.1086/430695.

Masai, K. (1984). "X-Ray Emission Spectra from Ionizing Plasmas". *Ap&SS* **98**, 367–395. DOI: 10.1007/BF00651415.

Masters, A., S. J. Schwartz, E. M. Henley, M. F. Thomsen, B. Zieger, et al. (2011). "Electron Heating at Saturn's Bow Shock". *J. Geophys. Res. Space Phys.* **116**, A10107. DOI: 10.1029/2011JA016941.

Matsuda, Masamune, Takaaki Tanaka, Hiroyuki Uchida, Yuki Amano & Takeshi Go Tsuru (2020). "Temporal and Spatial Variation of Synchrotron X-ray Stripes in Tycho's Supernova Remnant". *PASJ*. DOI: 10.1093/pasj/psaa075.

Matsuda, Masamune, Hiroyuki Uchida, Takaaki Tanaka, Hiroya Yamaguchi & Takeshi Go Tsuru (2022). "Discovery of Year-scale Time Variability from Thermal X-Ray Emission in Tycho's Supernova Remnant". *ApJ* **940**, 105. DOI: 10.3847/1538-4357/ac94cf.

McKee, Christopher F. (1974). "X-Ray Emission from an Inward-Propagating Shock in Young Supernova Remnants". *ApJ* **188**, 335–340. DOI: 10.1086/152721.

McKee, Christopher F. & Jeremiah P. Ostriker (1977). "A Theory of the Interstellar Medium: Three Components Regulated by Supernova Explosions in an Inhomogeneous Substrate." *ApJ* **218**, 148–169. DOI: 10.1086/155667.

Medina, Amber A., John C. Raymond, Richard J. Edgar, Nelson Caldwell, Robert A. Fesen & Dan Milisavljevic (2014). "Electron-Ion Equilibrium and Shock Precursors in the Northeast Limb of the Cygnus Loop". *Astrophys. J.* **791**, 30. DOI: 10.1088/0004-637X/791/1/30.

Mészáros, P. & M. J. Rees (1997). "Optical and Long-Wavelength Afterglow from Gamma-Ray Bursts". *ApJ* **476**, 232–237. DOI: 10.1086/303625.

Miceli, M., S. Orlando, D. N. Burrows, K. A. Frank, C. Argiroffi, et al. (2019). "Collisionless Shock Heating of Heavy Ions in SN 1987A". *Nat. Astron.* **3** (3), 236–241. DOI: 10.1038/s41550-018-0677-8.

Miceli, M., S. Sciortino, E. Troja & S. Orlando (2015). "Spatial Distribution of X-Ray Emitting Ejecta in Tycho's SNR: Indications of Shocked Titanium". *ApJ* **805**, 120. DOI: 10.1088/0004-637X/805/2/120.

Michael, Eli, Svetozar Zhekov, Richard McCray, Una Hwang, David N. Burrows, et al. (2002). "The X-Ray Spectrum of Supernova Remnant 1987A". *Astrophys. J.* **574**, 166–178. DOI: 10.1086/340591.

Minkowski, R. (1941). "Spectra of Supernovae". *PASP* **53**, 224. DOI: 10.1086/125315.

Mitsuda, Kazuhisa, Mark Bautz, Hajime Inoue, Richard L. Kelley, Katsuji Koyama, et al. (2007). "The X-Ray Observatory Suzaku". *PASJ* **59**, S1–S7. DOI: 10.1093/pasj/59.sp1.S1.

Okon, Hiromichi, Takaaki Tanaka, Hiroyuki Uchida, Hiroya Yamaguchi, Takeshi Go Tsuru, et al. (2020). "Deep XMM-Newton Observations Reveal the Origin of Recombining Plasma in the Supernova Remnant W44". *ApJ* **890**, 62. DOI: 10.3847/1538-4357/ab6987.

Okuno, Tomoyuki, Takaaki Tanaka, Hiroyuki Uchida, Felix A. Aharonian, Yasunobu Uchiyama, Takeshi Go Tsuru & Masamune Matsuda (2020). "Time Variability of Nonthermal X-Ray Stripes in Tycho's Supernova Remnant with Chandra". *ApJ* **894**, 50. DOI: 10.3847/1538-4357/ab837e.

Park, Sangwook, Svetozar A. Zhekov, David N. Burrows, Gordon P. Garmire & Richard McCray (2004). "A Chandra View of the Morphological and Spectral Evolution of Supernova Remnant 1987A". *Astrophys. J.* **610**, 275–284. DOI: 10.1086/421701.

Park, Sangwook, Svetozar A. Zhekov, David N. Burrows & Richard McCray (2005). "SNR 1987A: Opening the Future by Reaching the Past". *Astrophys. J.* **634**, L73–L76. DOI: 10.1086/498848.

Patnaude, Daniel J. & Robert A. Fesen (2007). "Small-Scale X-Ray Variability in the Cassiopeia A Supernova Remnant". *AJ* **133**, 147. DOI: 10.1086/509571.

— (2009). "Proper Motions and Brightness Variations of Nonthermal X-ray Filaments in the Cassiopeia A Supernova Remnant". *ApJ* **697**, 535–543. DOI: 10.1088/0004-637X/697/1/535.

— (2014). "A Comparison of X-Ray and Optical Emission in Cassiopeia A". *ApJ* **789**, 138. DOI: 10.1088/0004-637X/789/2/138.

Perlmutter, S., G. Aldering, M. della Valle, S. Deustua, R. S. Ellis, et al. (1998). "Discovery of a Supernova Explosion at Half the Age of the Universe". *Nature* **391**, 51–54. DOI: 10.1038/34124.

Picquenot, A., F. Acero, J. Bobin, P. Maggi, J. Ballet & G. W. Pratt (2019). "Novel Method for Component Separation of Extended Sources in X-ray Astronomy". *Astron. Astrophys.* **627**, A139. DOI: 10.1051/0004-6361/201834933.

Rakowski, Cara E., Parviz Ghavamian & John P. Hughes (2003). "The Physics of Supernova Remnant Blast Waves. II. Electron-Ion Equilibration in DEM L71 in the Large Magellanic Cloud". *ApJ* **590**, 846–857. DOI: 10.1086/375162.

Rakowski, Cara E., J. Martin Laming & Parviz Ghavamian (2008). "The Heating of Thermal Electrons in Fast Collisionless Shocks: The Integral Role of Cosmic Rays". *The Astrophysical Journal* **684**, 348–357. DOI: 10.1086/590245.

Rankine, W. J. Macquorn (1870). "On the Thermodynamic Theory of Waves of Finite Longitudinal Disturbance". *Phyl. Trans. Roy. Soc.* **160**, 277–288.

Ravi, Aravind P., Sangwook Park, Svetozar A. Zhekov, Marco Miceli, Salvatore Orlando, Kari A. Frank & David N. Burrows (2021). "Spectral Evolution of the X-ray Remnant of SN 1987A: A High-Resolution Chandra HETG Study". *ApJ* **922** (2), 140. DOI: 10.3847/1538-4357/ac249a.

Reynolds, Stephen P. (1998). "Models of Synchrotron X-Rays from Shell Supernova Remnants". *Astrophys. J.* **493**, 375–396. DOI: 10.1086/305103.

Reynolds, Stephen P., Kazimierz J. Borkowski, Una Hwang, John P. Hughes, Carles Badenes, J. M. Laming & J. M. Blondin (2007). "A Deep Chandra Observation of Kepler's Supernova Remnant: A Type Ia Event with Circumstellar Interaction". *Astrophys. J.* **668**, L135–L138. DOI: 10.1086/522830.

Reynolds, Stephen P., Brian J. Williams, Kazimierz J. Borkowski & Knox S. Long (2021). "Efficiencies of Magnetic Field Amplification and Electron Acceleration in Young Supernova Remnants: Global Averages and Kepler's Supernova Remnant". *ApJ* **917**, 55. DOI: 10.3847/1538-4357/ac0ced.

Riess, Adam G., Stefano Casertano, Wenlong Yuan, Lucas M. Macri & Dan Scolnic (2019). "Large Magellanic Cloud Cepheid Standards Provide a 1% Foundation for the Determination of the Hubble Constant and Stronger Evidence for Physics beyond ΛCDM". *Astrophys. J.* **876**, 85. DOI: 10.3847/1538-4357/ab1422.

Riess, Adam G., Alexei V. Filippenko, Peter Challis, Alejandro Clocchiatti, Alan Diercks, et al. (1998). "Observational Evidence from Supernovae for an Accelerating Universe and a Cosmological Constant". *Astron. J.* **116**, 1009–1038. DOI: 10.1086/300499.

Roper, Quentin, Miroslav Filipovic, Glenn E. Allen, Hidetoshi Sano, Laurence Park, et al. (2018). "An X-ray Expansion and Proper Motion Study of the Magellanic Cloud Supernova Remnant J0509-6731 with the Chandra X-ray Observatory". *Mon. Not. R. Astron. Soc.* **479**, 1800–1806. DOI: 10.1093/mnras/sty1196.

Ruiz-Lapuente, Pilar, Fernando Comeron, Javier Méndez, Ramon Canal, Stephen J. Smartt, et al. (2004). "The Binary Progenitor of Tycho Brahe's 1572 Supernova". *Nature* **431**, 1069–1072. DOI: 10.1038/nature03006.

Russell, H R, B R McNamara, J S Sanders, A C Fabian, P E J Nulsen, et al. (2012). "Shock Fronts, Electron-Ion Equilibration and Intracluster Medium Transport Processes in the Merging Cluster Abell 2146". *MNRAS* **423**, 236. DOI: 10.1111/j.1365-2966.2012.20808.x.

Rutherford, John, Daniel Dewey, Enectali Figueroa-Feliciano, Sarah N. T. Heine, Fabienne A. Bastien, Kosuke Sato & C. R. Canizares (2013). "A Decade-Baseline Study of the X-ray Knots of Cas A: The Paradox of Non-Evolution". *ApJ* **769**, 64. DOI: 10.1088/0004-637X/769/1/64.

Rybicki, George B. & Alan P. Lightman (1985a). "Bremsstrahlung". In: *Radiative Processes in Astrophysics*. John Wiley & Sons, Ltd, pp. 155–166. DOI: 10.1002/9783527618170.ch5.

— (1985b). "Synchrotron Radiation". In: *Radiative Processes in Astrophysics*. John Wiley & Sons, Ltd, pp. 167–194. DOI: 10.1002/9783527618170.ch6.

Sankrit, Ravi, William P Blair, Lisa M Frattare, Lawrence Rudnick, Tracey DeLaney, Ilana M Harrus & Jessica A Ennis (2008). "HUBBLE SPACE TELESCOPE/ADVANCED CAMERA FOR SURVEYS NARROWBAND IMAGING OF THE KEPLER SUPERNOVA REMNANT". *AJS* **135**, 538. DOI: 10.1088/0004-6256/135/2/538.

Sato, Toshiki & John P. Hughes (2017). "Direct Ejecta Velocity Measurements of Tycho's Supernova Remnant". *ApJ* **840**, 112. DOI: 10.3847/1538-4357/aa6f60.

Sato, Toshiki, Satoru Katsuda, Mikio Morii, Aya Bamba, John P. Hughes, Yoshitomo Maeda, Manabu Ishida & Federico Fraschetti (2018). "X-Ray Measurements of the Particle Acceleration Properties at Inward Shocks in Cassiopeia A". *ApJ* **853**, 46. DOI: 10.3847/1538-4357/aaa021.

Schwartz, Steven J., Michelle F. Thomsen, S. J. Bame & John Stansberry (1988). "Electron Heating and the Potential Jump across Fast Mode Shocks". *J. Geophys. Res.* **93**, 12923–12931. DOI: 10.1029/JA093iA11p12923.

Sedov, Leonid Ivanovich (1946). "Propagation of Strong Shock Waves". *J. Appl. Math. Mech.* **10**, 241–250.

Shimada, Nobue & Masahiro Hoshino (2005). "Effect of Strong Thermalization on Shock Dynamical Behavior". *J. Geophys. Res. Space Phys.* **110**, A02105. DOI: 10.1029/2004JA010596.

Skilling, J. (1975). "Cosmic Ray Streaming - I. Effect of Alfvén Waves on Particles." *MNRAS* **172**, 557–566. DOI: 10.1093/mnras/172.3.557.

Smith, R C, Robert P Kirshner, William P Blair & P F Winkler (1991). "Six Balmer-dominated Supernova Remnants". *ApJ* **375**, 652. DOI: 10.1086/170228.

Spitzer, L. (1962). *Physics of Fully Ionized Gases*.

Sun, Lei, Jacco Vink, Yang Chen, Ping Zhou, Dmitry Prokhorov, Gerd Pühlhofer & Denys Malyshev (2021). "The Post-impact Evolution of the X-Ray-emitting Gas in SNR 1987A as Viewed by XMM-Newton". *ApJ* **916**, 41. DOI: 10.3847/1538-4357/ac033d.

Takahashi, Tadayuki, Motohide Kokubun, Kazuhisa Mitsuda, Richard L. Kelley, Takaya Ohashi, et al. (2018). "Hitomi (ASTRO-H) X-ray Astronomy Satellite". *JATIS* **4**, 021402. DOI: 10.1117/1.JATIS.4.2.021402.

Tanaka, Takaaki, Tomoyuki Okuno, Hiroyuki Uchida, Hiroya Yamaguchi, Shiu-Hang Lee, Keiichi Maeda & Brian J. Williams (2021). "Rapid Deceleration of Blast Waves Witnessed in Tycho's Supernova Remnant". *ApJL* **906**, L3. DOI: 10.3847/2041-8213/abd6cf.

Tanaka, Takaaki, Hiroyuki Uchida, Hidetoshi Sano & Takeshi Go Tsuru (2020). "Shock-Cloud Interaction in the Southwestern Rim of RX J1713.7-3946 Evidenced by Chandra x-Ray Observations". DOI: 10.3847/2041-8213/abaef0.

Taylor, Geoffrey (1950). "The Formation of a Blast Wave by a Very Intense Explosion. I. Theoretical Discussion". *Proc. R. Soc. Lond. Ser. Math. Phys. Sci.* **201**, 159–174. DOI: 10.1098/rspa.1950.0049.

Telescope Array Collaboration, R. U. Abbasi, M. G. Allen, R. Arimura, J. W. Belz, et al. (2023). "An Extremely Energetic Cosmic Ray Observed by a Surface Detector Array". *Science* **382**, 903–907. DOI: 10.1126/science.abo5095.

The, L. -S., M. D. Leising, J. D. Kurfess, W. N. Johnson, D. H. Hartmann, N. Gehrels, J. E. Grove & W. R. Purcell (1996). "CGRO/OSSE Observations of the Cassiopeia A SNR." *Astron. Astrophys. Suppl. Ser.* **120**, 357–360.

The Fermi-LAT Collaboration, S. Abdollahi, M. Ackermann, M. Ajello, W. B. Atwood, et al. (2017). "Cosmic-Ray Electron-Positron Spectrum from 7 GeV to 2 TeV with the Fermi Large Area Telescope". *Phys. Rev. D* **95**, 082007. DOI: 10.1103/PhysRevD.95.082007.

Townsley, L. K., P. S. Broos, G. Chartas, E. Moskalenko, J. A. Nousek & G. G. Pavlov (2002). "Simulating CCDs for the Chandra Advanced CCD Imaging Spectrometer". *Nucl. Instrum. Methods Phys. Res. A* **486**, 716–750. DOI: 10.1016/S0168-9002(01)02155-6.

Truelove, J. Kelly & Christopher F. McKee (1999). "Evolution of Nonradiative Supernova Remnants". *ApJS* **120**, 299–326. DOI: 10.1086/313176.

Tsuchioka, Tomoya, Yasunobu Uchiyama, Ryota Higurashi, Hiroyoshi Iwasaki, Shumpei Otsuka, Shinya Yamada & Toshiki Sato (2021). "On the Origin of the Asymmetry of the Ejecta Structure and Explosion of G350.1–0.3". *ApJ* **912**, 131. DOI: 10.3847/1538-4357/abf2bd.

Uchiyama, Yasunobu & Felix A. Aharonian (2008). "Fast Variability of Nonthermal X-Ray Emission in Cassiopeia A: Probing Electron Acceleration in Reverse-Shocked Ejecta". *ApJL* **677**, L105. DOI: 10.1086/588190.

Uchiyama, Yasunobu, Felix A. Aharonian, Takaaki Tanaka, Tadayuki Takahashi & Yoshitomo Maeda (2007). "Extremely Fast Acceleration of Cosmic Rays in a Supernova Remnant". *Nature* **449**, 576–578. DOI: 10.1038/nature06210.

Van Adelsberg, Matthew, Kevin Heng, Richard McCray & John C. Raymond (2008). "Spatial Structure and Collisionless Electron Heating in Balmer-dominated Shocks". *ApJ* **689**, 1089–1104. DOI: 10.1086/592680.

Vink, Jacco (2012). "Supernova Remnants: The X-ray Perspective". *A&A Rev.* **20**, 49. DOI: 10.1007/s00159-011-0049-1.

Von Neumann, J. (1976). *Theory of Games, Astrophysics, Hydrodynamics and Meteorology*. Ed. by A.H. Taub. Collected Works. Pergamon Press.

Wang, Lifan, Peter Höflich & J. Craig Wheeler (1997). "Supernovae and Their Host Galaxies". *Astrophys. J.* **483**, L29–L32. DOI: 10.1086/310737.

Warren, Jessica S., John P. Hughes, Carles Badenes, Parviz Ghavamian, Christopher F. McKee, et al. (2005). "Cosmic-Ray Acceleration at the Forward Shock in Tycho's Supernova Remnant: Evidence from Chandra X-Ray Observations". *ApJ* **634**, 376. DOI: 10.1086/496941.

Webbink, R. F. (1984). "Double White Dwarfs as Progenitors of R Coronae Borealis Stars and Type I Supernovae." *Astrophys. J.* **277**, 355–360. DOI: 10.1086/161701.

Weisskopf, Martin C., Harvey D. Tananbaum, Leon P. Van Speybroeck & Stephen L. O'Dell (2000). "Chandra X-Ray Observatory (CXO): Overview". In: *X-Ray Opt. Instrum. Missions III*. Astronomical Telescopes and Instrumentation. Ed. by Joachim E. Truemper & Bernd Aschenbach. **4012**. International Society for Optics and Photonics. Munich, Germany: Proc.SPIE, 2–16. DOI: 10.1117/12.391545.

Whelan, John & I. Iben Jr. (1973). "Binaries and Supernovae of Type I". *Astrophys. J.* **186**, 1007–1014. DOI: 10.1086/152565.

Wilhelm, A., I. Telezhinsky, V. V. Dwarkadas & M. Pohl (2020). "Stochastic Re-Acceleration and Magnetic-Field Damping in Tycho's Supernova Remnant". *Astron. Astrophys.* **639**, A124. DOI: 10.1051/0004-6361/201936079.

Williams, Brian J. (2020). "Tycho's SNR: A New Era". *Chandra Propos. ID 22500080*, 5850.

Williams, Brian J., William P. Blair, Kazimierz J. Borkowski, Parviz Ghavamian, Sean P. Hendrick, et al. (2018). "The Expansion of the Young Supernova Remnant 0509-68.7 (N103B)". *Astrophys. J.* **865**, L13. DOI: 10.3847/2041-8213/aae08d.

Williams, Brian J., Kazimierz J. Borkowski, Parviz Ghavamian, John W. Hewitt, S. Alwin Mao, Robert Petre, Stephen P. Reynolds & John M. Blondin (2013). "Azimuthal Density Variations around the Rim of Tycho's Supernova Remnant". *ApJ* **770**, 129. DOI: 10.1088/0004-637X/770/2/129.

Williams, Brian J., Laura Chomiuk, John W. Hewitt, John M. Blondin, Kazimierz J. Borkowski, Parviz Ghavamian, Robert Petre & Stephen P. Reynolds (2016). "An X-ray and Radio Study of the Varying Expansion Velocities in Tycho's Supernova Remnant". *ApJL* **823**, L32. DOI: 10.3847/2041-8205/823/2/L32.

Wilms, J., A. Allen & R. McCray (2000). "On the Absorption of X-Rays in the Interstellar Medium". *ApJ* **542**, 914–924. DOI: 10.1086/317016.

Wilson, James R. (1985). *Supernovae and Post-Collapse Behavior*, p. 422.

Woosley, Stan & Thomas Janka (2005). "The Physics of Core-Collapse Supernovae". *Nature Phys* **1** (3), 147–154. DOI: 10.1038/nphys172.

Xi, Long, Terrance J. Gaetz, Paul P. Plucinsky, John P. Hughes & Daniel J. Patnaude (2019). "The Expansion of the Forward Shock of 1E 0102.2-7219 in X-Rays". *The Astrophysical Journal* **874**, 14. DOI: 10.3847/1538-4357/ab09ea.

XRISM Science Team (2020). "Science with the X-ray Imaging and Spectroscopy Mission (XRISM)". *ArXiv200304962 Astro-Ph*.

Yamaguchi, Hiroya, Fabio Acero, Chuan-Jui Li & You-Hua Chu (2021). "Discovery of Double-Ring Structure in the Supernova Remnant N103B: Evidence for Bipolar Winds from a Type Ia Supernova Progenitor". *Astrophys. J. Lett.* **910**, L24. DOI: 10.3847/2041-8213/abee8a.

Yamaguchi, Hiroya, Kristoffer A. Eriksen, Carles Badenes, John P. Hughes, Nancy S. Brickhouse, et al. (2014). "New Evidence for Efficient Collisionless Heating of Electrons at the Reverse Shock of a Young Supernova Remnant". *ApJ* **780**, 136. DOI: 10.1088/0004-637X/780/2/136.

Yamaguchi, Hiroya, John P. Hughes, Carles Badenes, Eduardo Bravo, Ivo R. Seitenzahl, Héctor Martínez-Rodríguez, Sangwook Park & Robert Petre (2017). "The Origin of the Iron-rich Knot in Tycho's Supernova Remnant". *ApJ* **834**, 124. DOI: 10.3847/1538-4357/834/2/124.

Zhang, Ming (2015). "Stochastic Acceleration of Galactic Cosmic Rays by Compressible Plasma Fluctuations in Supernova Shells". **812**, 148. DOI: 10.1088/0004-637X/812/2/148.

Zhou, Ping, Yang Chen, Zhi-Yu Zhang, Xiang-Dong Li, Samar Safi-Harb, Xin Zhou & Xiao Zhang (2016). "Expanding Molecular Bubble Surrounding Tyco's Supernova Remnant (SN 1572) Observed with the IRAM 30 m Telescope: Evidence for a Single-degenerate Progenitor". *ApJ* **826**, 34. DOI: 10.3847/0004-637X/826/1/34.

Zirakashvili, V. N. & Felix A. Aharonian (2007). "Analytical Solutions for Energy Spectra of Electrons Accelerated by Nonrelativistic Shock-Waves in Shell Type Supernova Remnants". *A&A* **465** (3), 695–702. DOI: 10.1051/0004-6361:20066494.